

Ludwig-Maximilians-Universität München  
Fakultät für Geowissenschaften

Dissertation

The Discontinuous Galerkin  
Approach for 3D Seismic Wave  
Propagation and 3D Dynamic  
Rupture Modeling in the Case of a  
Complex Fault System

Christian Pelties

11. Januar 2012



Dissertation zur Erlangung des akademischen Grades  
Doktor der Naturwissenschaften der  
Fakultät für Geowissenschaften  
Ludwig-Maximilians-Universität München

Vorgelegt von Christian Pelties am 11. Januar 2012

1. Gutachter: Prof. Dr. Heiner Igel
2. Gutachter: Prof. Dr. Peter Moczo

Tag der Disputation: 20.06.2012



# Abstract

The aim of this research study, is to contribute in the development of the Arbitrary high-order DERivatives Discontinuous Galerkin (ADER-DG) method for elastic wave propagation and its application. Thus, after a general introduction we first explain the underlying numerical scheme.

Then, the general benefits and capabilities of the proposed method are analyzed with a special focus on the oil and gas industry. Therein, the performance on large scale parallel computer clusters is demonstrated as well as two typical applications in geophysical exploration: a marine seismic survey and sonic logging in borehole wells.

Next, a rigorous accuracy study about accurate geometry representation is presented. In this sense, we discuss advantages and disadvantages of structured meshes, which violate material interfaces as they result in staircase approximations but are computationally very efficient, and unstructured meshes, that are aligned to material interfaces. It is shown that the accuracy of synthetic seismograms strongly depends on the signal frequency, material contrast and mesh resolution if the material interfaces are not respected by the mesh. Finally, we define clear rules that have to be adhered to guarantee acceptable results for cases where material contrasts occurring along curved interfaces are discretized with regular meshes.

The main goal of the work is to extend the ADER-DG method to three-dimensional dynamic rupture problems for complex fault systems. We give a complete description of the algorithm, benchmark the new implementation by the SCEC TPV3 test problem and compare it with two well established numerical methods. Afterwards, the systematic consistency is proved by a convergence test. In the end, we demonstrate the capabilities of the high-order accurate ADER-DG scheme on unstructured meshes for strong ground motion modeling. Therefore, an earthquake scenario, inspired by the 1992 Landers earthquake, is simulated that includes curved faults, fault branches and surface topography.



# Contents

<b>Abstract</b>	<b>v</b>
<b>1. Introduction</b>	<b>1</b>
<b>2. The ADER-DG Method</b>	<b>7</b>
2.1. Numerical Schemes for Seismic Wave Propagation . . . . .	7
2.2. Elastic Wave Equations . . . . .	9
2.3. Numerical Discretization . . . . .	11
2.3.1. Basis Functions . . . . .	11
2.3.2. Semi-discrete Formulation . . . . .	12
2.3.3. Coordinate Transformation into Reference Element . . . . .	15
2.3.4. The High-order Accurate Time Discretization: ADER . . . . .	17
2.4. Sources . . . . .	21
2.5. Boundary Conditions . . . . .	21
2.5.1. Free-Surface Boundaries . . . . .	21
2.5.2. Absorbing Boundaries . . . . .	22
2.5.3. Periodic Boundaries . . . . .	22
2.6. Computational Aspects . . . . .	22
<b>3. Wave Field Modeling in Exploration Seismology</b>	<b>25</b>
3.1. Introduction . . . . .	25
3.2. Discontinuous Galerkin Method . . . . .	26
3.3. Suitability for HPC-Infrastructure . . . . .	28
3.4. Applications . . . . .	29
3.4.1. Borehole-Scale Modeling . . . . .	30
3.4.2. Reservoir-Scale Modeling . . . . .	32
3.5. Concluding Remarks . . . . .	36
<b>4. Regular vs. Irregular Meshing for Complicated Models</b>	<b>39</b>
4.1. Introduction . . . . .	39
4.2. Importance of Interface Approximation . . . . .	42
4.2.1. Model Setup . . . . .	42
4.2.2. Accuracy Analysis . . . . .	46
4.2.3. Discretization Rules . . . . .	50
4.3. Multiple Layers with Undulating Interfaces . . . . .	56
4.3.1. Test Case Description . . . . .	59
4.3.2. Results and Discussion . . . . .	60

---

4.4. Sedimentary Basin . . . . .	64
4.4.1. Test Case Description . . . . .	64
4.4.2. Results and Discussion . . . . .	65
4.5. Conclusions . . . . .	71
<b>5. Dynamic Rupture with a 3D DG Method</b>	<b>73</b>
5.1. Introduction . . . . .	74
5.2. Dynamics of Fault Rupture . . . . .	76
5.3. Fault Dynamics within the Discontinuous Galerkin Framework . . . . .	77
5.3.1. Discretization of the Linear Elastic Wave Equation . . . . .	78
5.3.2. Flux computation . . . . .	79
5.4. Verification . . . . .	82
5.4.1. Code verification on the SCEC TPV3 . . . . .	82
5.4.2. Convergence test . . . . .	84
5.5. The Landers 1992 Earthquake . . . . .	90
5.6. Conclusions . . . . .	94
<b>6. Conclusion</b>	<b>101</b>
<b>Bibliography</b>	<b>119</b>
<b>A. Orthogonal Basis Functions for Tetrahedral Elements</b>	<b>121</b>
<b>B. Coordinate Transformation of Tetrahedra</b>	<b>123</b>
<b>Acknowledgment</b>	<b>125</b>

# Chapter 1.

## Introduction

Only very few events have such an impact on humans, their infrastructure and personal properties as earthquakes. Most devastating earthquakes cause tens of thousands casualties and damage of up to a billion dollars. Recent examples are the 2008 Sichuan earthquake killing estimated 68,000 people, the 2010 Haiti earthquake close to Haiti's capital Port-au-Prince with a death toll between 46,000 and 96,000 and millions of homeless, and the 2011 Tohoku catastrophe with its followed Tsunami causing a nuclear core melt, overall cost of up to US\$ 300 billion and more than 15,000 fatalities. Beside these dramatic numbers related to human life, large earthquakes also change planetary parameters of the earth. For instance, after the 2011 Tohoku earthquake the earth's axis was shifted by 10-25 cm, leading to a shortened day by 1.8 microseconds.

The basic mechanism of an earthquake can be understood in first order as frictional sliding of gigantic rock masses. These rock masses move in order to release stresses, which were accumulated in hundreds of years due to moving tectonic plates (several cm per year), resulting in intensive shaking and displacement of the ground. Of course, scientists want to understand under which circumstances earthquakes occur, how an earthquake works and which seismic risk potentially affected areas may have.

Although neither the exact time nor the location of the next *big one* can be predicted, statistics provide information about recurrence intervals as well as rough estimates of stress accumulations. Furthermore, many faults are known along which earthquake ruptures propagate (e.g. the San Andreas fault). Hence, earthquake scientists have the chance to model fictive earthquake ruptures at faults which are expected to break and study the effect on nearby structures. This is known as strong ground motion modeling and became an important tool that increased our knowledge about seismic hazard and improved building construction codes, for instance. Those simulations of hypothetical earthquakes provide information about ground shaking in terms of the intensity, acceleration and velocity, in fact, their peak values and spectral response (see Fig. 1.1). Having an educated guess of the above effects is the main benefit of the earthquake scenario for planning and preparedness purposes.

State of the art in strong ground motion modeling is to include the rupture dynamics directly in the simulations. It means that the slip on the fault is a function of the stress state as well as the frictional parameters. This way, slip based on physical friction laws has to be solved additionally. As a major benefit, the more realistic source representation enables the interaction of transient wavefields, evaluating stresses, as well as site and directivity effects with the rupture on the fault itself. Previous non-dynamically models

with an *a priori* assumed kinematic source ignored those effects leading in some cases to wrong conclusions or interpretations (e.g. analyzed by Dalguer *et al.*, 2001). Despite the fact, that dynamic rupture sources produce more realistic ground shaking information, those simulations are much more challenging in terms of the mathematical formulation and contain more unknowns, due to the non-linear nature and large uncertainties of the underlying physics. The high level of accuracy which could be achieved requires, in turn, more specific information and details about fault geometries, heterogeneous stress distributions on small scale and the actual friction coefficients - parameters which often must be assumed. Therefore, spontaneous rupture simulation remains an ongoing research topic with many construction sites.

Dynamic rupture modeling became also an important tool in the field of earthquake source physics. Hereby, the researchers try to understand the fundamental mechanisms of an earthquake in all details. Typical research topics are testing of different friction laws (linear slip-weakening, velocity weakening, rate-and-state), the effect of bimaterial ruptures, or interaction of waves reflected by material interfaces as faults are often embedded in low-velocity zones (e.g. Bizzari *et al.*, 2001; Rojas *et al.*, 2009; Brietzke *et al.*, 2009; DeDontney *et al.*, 2011b; Huang and Ampuero, 2011). Of particular interest is also the influence of complex geometries, such as curved, rough and branching faults (Dunham *et al.*, 2011; DeDontney *et al.*, 2011a; Tamura and Ide, 2011). Finally, the gained insights are incorporated into strong ground motion models to improve the seismic hazard knowledge.

It should be mentioned, that forward wave propagation tools are not exclusively subjected to model earthquakes. The mathematical concept can be applied straight forward to problems in the oil and gas exploration industry. Instead of earthquakes, artificial sources (e.g. explosions, air guns, piezoelectric-controlled vibrations) generate here seismic waves to probe subsurface properties. After complex processing of the collected seismic data, teams of geophysicists, geologists and petroleum engineers construct models of the underground. With the obtained maps hydrocarbon reservoirs are identified and drilling engineers are supported with necessary information on meter scale to reach the target horizons while avoiding dangerous gas cavities. The hereby involved inversion and migration techniques rely on accurate synthetic data produced by seismic forward modeling. Other areas where wave simulations come into play are, for instance, survey design or principle investigations in research and development to improve the understanding of seismic measurements.

Seismic wave propagation modeling is performed on computers as the earth's properties (temperatures, pressures, rupture speeds, details of geological settings, etc.) cannot be sufficiently represented in laboratory experiments. This connects seismology with numerics and informatics making earthquake science very interdisciplinary. In fact, realistic simulations are computationally extremely expensive as many small scale features must be included, but the waves propagate over large distances. Thus, the problems can only be solved under usage of large-scale high-performance computing infrastructures. Whether used in earthquake seismology or in industrial applications, the challenge is to develop efficient numerical methods which are, first of all, very accurate and reliable, but also flexible in order to include complex geological information and realistic initial and boundary conditions. Many different approaches have been developed in the past. All of them

---

have certain advantages, but also drawbacks. A brief summary and discussion is given in Section 2.1.

In this work, we will focus on the so-called Arbitrary high-order DERivates Discontinuous Galerkin (ADER-DG) method. As rather recently introduced in computational seismology by Käser and Dumbser (2006), DG methods seem to become increasingly popular (Etienne *et al.*, 2009; Smith *et al.*, 2010; Wilcox *et al.*, 2010). DG supports discretization of the computational domain into very flexible tetrahedral elements to align better geometrical constraints while generating high accurate synthetic data. Although DG methods are in general more expensive than standard solvers (e.g. Finite Differences, Spectral Element methods), various techniques (e.g. *hp*-adaptivity, local time stepping, mortar elements; see Chapter 2) help to concentrate the computational power to areas of interest. Furthermore, DG schemes show excellent scaling properties on modern large scale parallel computer platforms (see Section 3.3). To conclude, we are convinced that DG methods will pay off for large scale models with complex geometry and strongly varying material properties.

A unique advantage compared to other methodologies is that the current ADER-DG implementation is able to solve spontaneous rupture problems without generating numerical noise. The seminal two-dimensional research study of de la Puente *et al.* (2009) introduced a new concept of incorporating rupture dynamics via fluxes. An important outcome of their study was that the ADER-DG solution is very smooth and free of spurious high-frequency oscillations. Therefore, it does not require neither artificial damping nor filtering that could influence the rupture propagation and bias the results. Due to the tetrahedral mesh approach complex fault planes could be modeled adequately with small elements while fast mesh coarsening is possible with increasing distance from the fault. In combination with the high-order accuracy ADER-DG seems to be a promising concept for strong ground motion modeling and earthquake physics investigations. Corollary, the extension to three-dimensional rupture problems is the key task and main goal of this Ph.D. thesis and led to the publication Pelties *et al.* (2012).

Although the mathematical formulation was defined decades ago by e.g. Burridge and Knopoff (1967) or Andrews (1973), all suggested solutions of the problem remained unsatisfying for a long time. The difficulties lie in the numerics as the physical description of the frictional sliding is implemented as time-dependent Dirichlet (respectively Neumann) boundary conditions. These artificially imposed boundaries amplify certain characteristic modes (resonant frequencies) in the wavefield spectra of the tractions (respectively velocities), which result in self-sustained oscillations in the time series. Dispersion analyses clarify their origin (J.-P. Ampuero, personal communication, 2011). As mentioned above, de la Puente *et al.* (2009) take advantage of numerical upwinding fluxes to implement the rupture dynamics. In particular, the here used *Godunov* flux is intrinsically dissipative, at which the amount of numerical dissipation increases as a function of frequency (Hesthaven and Warburton, 2008, p.90, Fig. 4.1) acting in an optimal way on the non-physical modes. Thus, the spurious oscillations are damped with minimal invasion on the physically meaningful wavelengths. We will see in Chapter 5 how the scheme will perform in benchmark tests and under realistic conditions.

The work is structured as follows: First, the ADER-DG method is introduced for the three-dimensional, elastic, isotropic case in Chapter 2. The following Chapter 3

introduces the advantages of the method for high-performance computing infrastructures supported by two examples of the oil and gas exploration industry. Next, the importance of correct approximations of material interfaces is discussed in Chapter 4. Hereby, a quantitative error analysis was performed to obtain clear rules that should be respected in order to generate reliable results. These rules are proved by two realistic test cases. Finally, in Chapter 5 the implementation of three-dimensional dynamic rupture problems in the ADER-DG framework is presented. For this purpose, we elaborate the algorithm and compare the code with two well established numerical methods. A comprehensive convergence study shall verify the systematic correctness. In the end, a hypothetical earthquake is modeled on a complex fault system to demonstrate the features of the new scheme. The scenario based on the 1992 Landers earthquake includes surface topography as well as curved and branched fault segments.

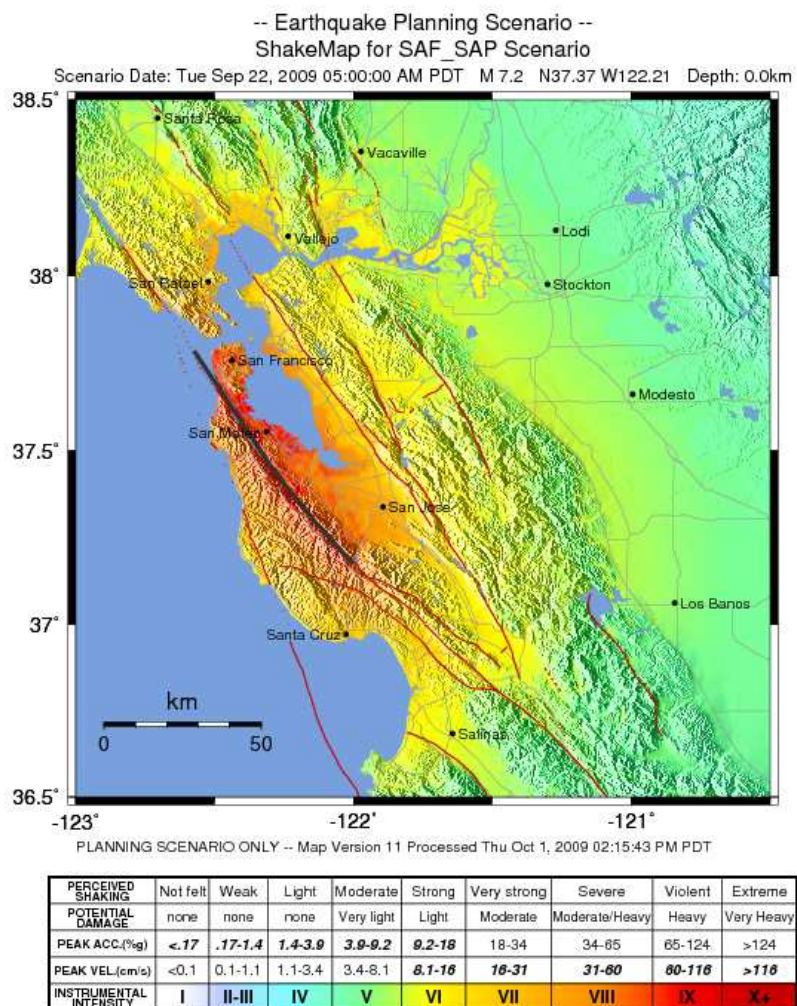


Figure 1.1.: Intensity of ground shaking of an hypothetical earthquake with Magnitude 7.2 in the vicinity of San Francisco. In this example, the rupture of a part of the northern San Andreas fault was modeled. (Image was made by U.S. Geological Service under public domain and can be obtained from <http://earthquake.usgs.gov/earthquakes/shakemap/>)



# Chapter 2.

## The ADER-DG Method

A substantial part of the Ph.D. work was to apply and participate in the development of the software SeisSol based on the so-called Arbitrary high-order DERivative Discontinuous Galerkin (ADER-DG) method. SeisSol models seismic wave propagation with the focus on large scale problems with complex geometry, heterogeneous media and realistic earthquake sources. As the used numerical scheme is fundamental for this thesis, the principal ideas of its theory will be briefly repeated and discussed in the following Chapter. A rigorous derivation can be found in Käser and Dumbser (2006); Dumbser and Käser (2006); Dumbser *et al.* (2007) and de la Puente (2008), accuracy analysis and benchmarks in Käser *et al.* (2008); Pelties *et al.* (2010) and Chaljub *et al.* (2010), and examples demonstrating its benefits in industrial and scientific applications in Käser *et al.* (2007); Käser and Gallovič (2008); Gallovič *et al.* (2010); Hermann (2010) and Käser *et al.* (2010).

### 2.1. Numerical Schemes for Seismic Wave Propagation

Before the ADER-DG method is introduced, a brief overview over other methodologies that exist to model seismic wave propagation is given. Of course, all of the different techniques have certain advantages but also drawbacks.

Finite Difference (FD) methods are successfully used since decades to solve any partial differential equation in many research fields and so also in seismology (e.g. Madariaga, 1976; Virieux, 1984, 1986; Levander, 1988; Moczo *et al.*, 2002). FD schemes are relatively easy to implement, robust and computationally efficient. Often, FD methods are still implemented on regular Cartesian spatial grids. This way, topography or undulating material interfaces usually result in staircase approximations leading to first-order errors proportional to the grid spacing or time step that are insensitive to the approximation order of the numerical scheme (Gustafsson and Wahlund, 2004; Symes *et al.*, 2008). In particular, free-surface boundaries require a high resolution in order to avoid numerical artifacts (Robertsson, 1996; Bohlen and Saenger, 2006; Pelties *et al.*, 2010). Furthermore, the use of regular grids does not allow to concentrate the computational power to areas

---

This Chapter represents a summary in own words of the ADER-DG discretization. The original fundamental research studies are by Käser and Dumbser (2006); Dumbser and Käser (2006); de la Puente (2008) and Hermann (2010) and references therein.

where it is needed. If a topography or a low-velocity sedimentary layer requires a fine grid, this grid resolution must be applied to the complete model domain. An estimation of the computational costs needed in the case for a large-scale strong ground motion simulation is given by Bao *et al.* (1998). Note that the drawback of regular grids is method independent. To overcome this issue, grid variability (Ely *et al.*, 2008; Kozdon *et al.*, 2012) and so-called grid doubling techniques (Pitarka, 1999; Kristek *et al.*, 2010; Lisitsa *et al.*, 2011) have been introduced into FD schemes. In particular, grid doubling techniques might improve the efficiency, but are difficult to implement and can produce undesired numerical artifacts like instabilities or spurious reflections at the grid interfaces. However, those artifacts have not been observed in the study of Kristek *et al.* (2010) (P. Moczo, personal communication, 2012). Furthermore, Moczo *et al.* (2007b) analyze existing FD schemes for improving the topography and material interface representation in detail and suggest solutions. An overview about modern FD techniques and their variations are summarized in Moczo *et al.* (2007a).

The restriction to Cartesian structured grids holds in general for Pseudo-Spectral (PS) methods, too (e.g. Carcione, 1994). The PS approach uses a set of orthogonal basis functions to discretize the space dependent physical quantities to improve the accuracy.

Finite Element (FE) (e.g. Oglesby *et al.*, 1998; Aagaard *et al.*, 2001; Galis *et al.*, 2008) and Finite Volume (FV) (e.g. Benjema *et al.*, 2007, 2009) methods overcome these drawbacks as the formulation allows for various element types among tetrahedra. A useful feature to create models with complex geometries. However, the accuracy is limited for FE and FV schemes as they are usually only computationally efficient in low-order formulations which are very dispersive and require a fine mesh.

The Spectral Element (SE) method can be seen as an evolution of classical FE schemes. Due to an intelligent choice of the integration point locations high-order accurate formulations can be realized with less computational costs compared to standard FE schemes. The superior efficiency and scalability on parallel High-Performance Computing (HPC) architectures of the SE method enables for the first time full elastic wave propagation on the whole Earth. Combined with the fact that deformed hexahedral elements can be used, SE became extremely popular in the seismological community (e.g. Seriani *et al.*, 1992; Priolo *et al.*, 1994; Seriani, 1998; Komatitsch and Vilotte, 1998; Komatitsch *et al.*, 2002; Chaljub *et al.*, 2007). However, although deformable hexahedral elements are more flexible than regular grids, meshing complex topography and undulating interior material interfaces is still challenging. Creating an unstructured hexahedral mesh is very time consuming and can easily occupy a scientist for weeks or months. The flexibility of hexahedral elements is limited and the discretized model is often unsatisfying. For spontaneous rupture simulations, SE methods generate strong spurious oscillations which potentially affect the rupture evolution itself.

The here proposed ADER-DG method might overcome many of the beforehand mentioned issues. A DG method can be understood as a FE method inheriting the desired concept of numerical fluxes from FV while showing spectral convergence properties like in SE (Reed and Hill, 1973; Hesthaven and Warburton, 2008). Furthermore, the method enables the use of many different element types, in particular the here used tetrahedra, to provide an enhanced meshing flexibility (see Section 2.6). The basic idea of a DG scheme is that the physical variables are approximated by a set of polynomial basis functions within

each element. The degree of the polynomials  $N$  correspond to the order of accuracy  $\mathcal{O}$  of the scheme via the relationship  $\mathcal{O} = N + 1$  and can be adjusted for each single element ( $p$ -adaptivity). Information between neighboring elements is exchanged by fluxes. This way, no global matrix has to be inverted and the scheme is entirely local independent of the degree of the polynomials. Thus, DG methods show excellent scaling on large parallel HPC infrastructures. In the present case, a high-order accurate time marching scheme, the ADER approach, is used. The ADER approach was originally introduced by Toro *et al.* (2001) and later combined with DG formulations by Schwartzkopff *et al.* (2002); Dumbser and Munz (2005a,b) for linear hyperbolic systems. The concept of ADER for DG schemes provides high-order accuracy in space and in time without the storage of intermediate time levels. Furthermore, each element can run its own optimal time step length regarding to the Courant-Friedrichs-Lewy (CFL) criterion (Courant *et al.*, 1928). This way, the time step length is not restricted by the smallest element in the entire model domain. The feature is known as local time stepping (LTS) (Dumbser *et al.*, 2007).

A special focus in this thesis lies on the numerical development and simulation of spontaneous rupture propagation. At the moment, ADER-DG is the only method that solves the problem without generating artificial high-frequency noise (de la Puente *et al.*, 2009, and Chapter 5).

It should be noticed, that the main drawback of DG methods is a higher computational cost and a more complex algorithm, which decelerates the coding and general development. However, with a smart use of the given features computational effort can be concentrated where it is needed. Is the meshing process considered, at which tetrahedral meshes can clearly be faster generated than hexahedral meshes, the concept pays off for complex geometries.

## 2.2. Elastic Wave Equations

For modeling numerically seismic wave propagation we need to solve the linear hyperbolic elastic wave equations. A given media can be assumed to be isotropic elastic if no other types of rheology as e.g. viscoelasticity, anisotropy or poroelasticity governs the wave propagation and the linear relationships between stress and strain is valid (Aki and Richards, 2002), which means strain lower  $\sim 10^{-4}$  (Stein and Wysession, 2003). At this point, it should be mentioned that the here introduced methodology is capable to model various rheologies as demonstrated in de la Puente *et al.* (2007, 2008) and de la Puente (2008), if the model requires a more complex material representation. However, we will assume linear elasticity while developing the numerical scheme in the following as the discretization is similar for all other rheologies, but we can concentrate on the technical key issues.

The elastodynamic equations are derived from Hooke's law and Newton's laws of motion. There are several possibilities of the mathematical formulation which are in general equivalent, but have certain advantages and drawbacks in the numerical implementation. It will be seen that a first-order velocity-stress formulation is best suited for the ADER time integration and the numerical fluxes. Omitting external source terms we formulate

the mathematical problem as:

$$\begin{aligned}
\frac{\partial}{\partial t}\sigma_{xx} - (\lambda + 2\mu)\frac{\partial}{\partial x}u - \lambda\frac{\partial}{\partial y}v - \lambda\frac{\partial}{\partial z}w &= 0, \\
\frac{\partial}{\partial t}\sigma_{yy} - \lambda\frac{\partial}{\partial x}u - (\lambda + 2\mu)\frac{\partial}{\partial y}v - \lambda\frac{\partial}{\partial z}w &= 0, \\
\frac{\partial}{\partial t}\sigma_{zz} - \lambda\frac{\partial}{\partial x}u - \lambda\frac{\partial}{\partial y}v - (\lambda + 2\mu)\frac{\partial}{\partial z}w &= 0, \\
\frac{\partial}{\partial t}\sigma_{xy} - \mu\left(\frac{\partial}{\partial x}v + \frac{\partial}{\partial y}u\right) &= 0, \\
\frac{\partial}{\partial t}\sigma_{yz} - \mu\left(\frac{\partial}{\partial z}v + \frac{\partial}{\partial y}w\right) &= 0, \\
\frac{\partial}{\partial t}\sigma_{xz} - \mu\left(\frac{\partial}{\partial z}u + \frac{\partial}{\partial x}w\right) &= 0, \\
\rho\frac{\partial}{\partial t}u - \frac{\partial}{\partial x}\sigma_{xx} - \frac{\partial}{\partial y}\sigma_{xy} - \frac{\partial}{\partial z}\sigma_{xz} &= 0, \\
\rho\frac{\partial}{\partial t}v - \frac{\partial}{\partial x}\sigma_{xy} - \frac{\partial}{\partial y}\sigma_{yy} - \frac{\partial}{\partial z}\sigma_{yz} &= 0, \\
\rho\frac{\partial}{\partial t}w - \frac{\partial}{\partial x}\sigma_{xz} - \frac{\partial}{\partial y}\sigma_{yz} - \frac{\partial}{\partial z}\sigma_{zz} &= 0,
\end{aligned} \tag{2.1}$$

where  $\lambda$  is the first Lamé constant,  $\mu$  is the shear modulus,  $\rho$  is the density,  $\sigma_{ij}$  are the components of the stress tensor and  $u$ ,  $v$  and  $w$  are the components of the particle velocity in the  $x$ ,  $y$ , and  $z$  directions, respectively. Grouping stresses and velocities into a vector  $\mathbf{Q} = (\sigma_{xx}, \sigma_{yy}, \sigma_{zz}, \sigma_{xy}, \sigma_{yz}, \sigma_{xz}, u, v, w)^T$ , we write the system of equations (2.1) in a more compact form following LeVeque (2002):

$$\frac{\partial Q_p}{\partial t} + A_{pq}\frac{\partial Q_q}{\partial x} + B_{pq}\frac{\partial Q_q}{\partial y} + C_{pq}\frac{\partial Q_q}{\partial z} = 0, \tag{2.2}$$

where the space-dependent Jacobian matrices  $A$ ,  $B$  and  $C$  include the material properties. Classical tensor notation and Einstein's summation convention are assumed.

As the PDE (2.2) is hyperbolic, the Jacobian matrices have real eigenvalues,

$$\begin{aligned}
\alpha_1 &= -c_p, & \alpha_2 &= -c_s, & \alpha_3 &= -c_s, \\
\alpha_4 &= 0, & \alpha_5 &= 0, & \alpha_6 &= 0, \\
\alpha_7 &= c_s, & \alpha_8 &= c_s, & \alpha_9 &= c_p,
\end{aligned} \tag{2.3}$$

with

$$c_p = \sqrt{\frac{\lambda + 2\mu}{\rho}} \quad \text{and} \quad c_s = \sqrt{\frac{\mu}{\rho}}. \tag{2.4}$$

$c_p$  and  $c_s$  can be physically interpreted as the P wave and S wave velocities, respectively. The eigenvalues (2.3) show, that two P waves propagate with speeds  $\alpha_1$  and  $\alpha_9$  and four different polarized S waves with  $\alpha_2, \alpha_3, \alpha_7$  and  $\alpha_8$ .

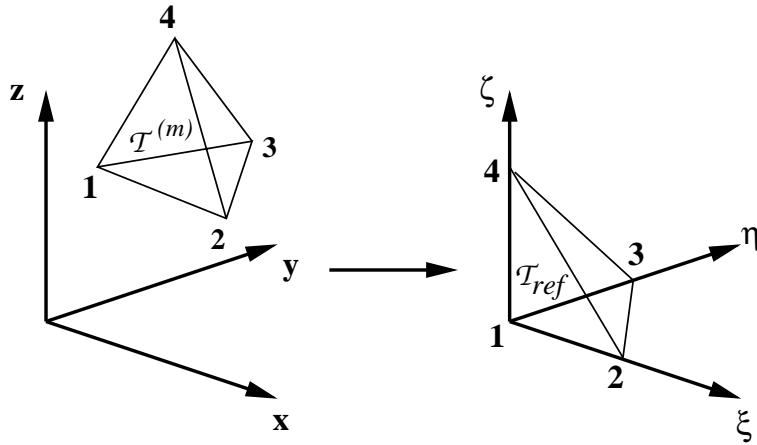


Figure 2.1.: Transformation of an element from the global coordinate system into the reference element in the local coordinate system.

## 2.3. Numerical Discretization

First step of the discretization is the division of the computational domain  $\Omega \in \mathbb{R}^3$  into conforming elements  $\mathcal{T}$  indexed by the superscript  $(m)$ . The division or better *meshing* is not a trivial task and will be addressed again in Section 2.6. Although various element types could be chosen, the following description is based on tetrahedral elements with completely flat surfaces as they are mostly used in the studies of this thesis. Each tetrahedral element has four neighbors  $\mathcal{T}^{(m_j)}$  with  $j = 1, \dots, 4$  as long as it is not a boundary element. Its location is uniquely specified by four vertices  $\mathbf{x}_i$  with  $i = 1, \dots, 4$  and  $\mathbf{x}_i = (x_i, y_i, z_i)$ . A common concept in FE methods is to transform the individual elements into a reference element  $\mathcal{T}_{ref}$  defined by the points  $\mathbf{x}_1 = (0, 0, 0)$ ,  $\mathbf{x}_2 = (1, 0, 0)$ ,  $\mathbf{x}_3 = (0, 1, 0)$  and  $\mathbf{x}_4 = (0, 0, 1)$ . The local coordinate system of the reference tetrahedron is denoted by  $\boldsymbol{\xi} = \xi, \eta, \zeta$  (see Fig. 2.1 and Appendix B). This way, many calculations can be precomputed and stored once in the reference element in order to avoid repeating or identical tasks.

Here, we suppose the Jacobian matrices  $A$ ,  $B$  and  $C$  of Eq. (2.2) to be constant inside an element  $\mathcal{T}^{(m)}$ . This approach implies that material interfaces have to be respected by the mesh for an appropriate model discretization. Note, Castro *et al.* (2010) demonstrated the case of a varying material representation inside an element for ADER-DG to save computational costs where the dispersion properties would allow for large element sizes, but the material properties of the model change on smaller scale. However, a varying material distribution inside an element is not used in this thesis.

In the following, a complete discretization of the elastic wave equations using the ADER-DG method will be shown.

### 2.3.1. Basis Functions

In every element the solution of Eq. (2.2) is approximated by a linear combination of purely space-dependent polynomial basis functions  $\Phi_l(\xi, \eta, \zeta)$  of degree  $N$  and purely time-dependent degrees of freedom  $\hat{Q}_{pl}^{(m)}(t)$ . The index  $p$  stands for the  $p$ th unknown

in  $\mathbf{Q}$  and  $l$  indicates the  $l$ th basis function. For the current implementation we are using orthogonal and hierarchical *Dubiner's basis functions* as given in Cockburn *et al.* (2000) and quoted in Appendix A. A complete basis for a polynomial degree  $N$  embraces  $L = (N+1)(N+2)(N+3)/6$  basis functions. As any point of the global coordinate system can be mapped into the reference tetrahedron we define the approximated solution for element ( $m$ ) as:

$$\left(Q_h^{(m)}\right)_p(\boldsymbol{\xi}, t) = \hat{Q}_{pl}^{(m)}(t)\Phi_l(\boldsymbol{\xi}), \quad (2.5)$$

Note, degrees of freedom  $\hat{g}_i$  of an approximated interpolation  $g_h$  represented by the linear combination

$$g_h = \hat{g}_i\Phi_i, \quad (2.6)$$

can be obtained via a  $L_2$  projection

$$\hat{g}_i = \frac{\int_{\mathcal{T}_{ref}} g\Phi_j dV}{\int_{\mathcal{T}_{ref}} \Phi_i\Phi_j dV}, \quad (2.7)$$

where  $g$  is the exact function. The integrals can be solved by Gaussian integration of sufficient accuracy.

### 2.3.2. Semi-discrete Formulation

Following the standard procedure of FE schemes we first multiply Eq. (2.2) by a test function  $\Phi_k$ , which is identical to the basis functions in Galerkin schemes, and integrate over an entire element  $\mathcal{T}^{(m)}$ :

$$\int_{\mathcal{T}^{(m)}} \Phi_k \frac{\partial Q_p}{\partial t} dV + \int_{\mathcal{T}^{(m)}} \Phi_k \left( A_{pq} \frac{\partial Q_q}{\partial x} + B_{pq} \frac{\partial Q_q}{\partial y} + C_{pq} \frac{\partial Q_q}{\partial z} \right) dV = 0. \quad (2.8)$$

By integrating the second term by parts we obtain

$$\begin{aligned} \int_{\mathcal{T}^{(m)}} \Phi_k \frac{\partial Q_p}{\partial t} dV + \int_{\mathcal{T}^{(m)}} \nabla [\Phi_k (A_{pq}\hat{x} + B_{pq}\hat{y} + C_{pq}\hat{z})] Q_q dV \\ - \int_{\mathcal{T}^{(m)}} (\nabla\Phi_k) (A_{pq}\hat{x} + B_{pq}\hat{y} + C_{pq}\hat{z}) Q_q dV = 0. \end{aligned} \quad (2.9)$$

Hereby,  $\hat{x}, \hat{y}, \hat{z}$  denote the normal vectors in  $x$ -,  $y$ - and  $z$ -direction. Applying Gauss' theorem on the second term we can rewrite Eq. (2.9) as

$$\int_{\mathcal{T}^{(m)}} \Phi_k \frac{\partial Q_p}{\partial t} dV + \int_{\partial\mathcal{T}^{(m)}} \Phi_k F_p^h dS - \int_{\mathcal{T}^{(m)}} (\nabla\Phi_k) (A_{pq}\hat{x} + B_{pq}\hat{y} + C_{pq}\hat{z}) Q_q dV = 0. \quad (2.10)$$

where the numerical flux  $F_p^h = (A_{pq}\hat{x} + B_{pq}\hat{y} + C_{pq}\hat{z}) Q_q \mathbf{n}$  has been introduced since  $Q_h$  is discontinuous at an element boundary.

In the isotropic case of Eq. (2.2) the system is rotational invariant. Thus, the flux can be computed in a *face-aligned* coordinate system, which is aligned with the outward pointing unit normal vector  $\mathbf{n}$  of an element boundary. The equation

$$Q_p = T_{pq} Q_q^n \quad (2.11)$$

transforms the unknowns vector  $Q_p$  to the vector  $Q_q^n$  in the local normal coordinate system. With the normal vector  $\mathbf{n} = (n_x, n_y, n_z)^T$  and the two tangential vectors  $\mathbf{s} = (s_x, s_y, s_z)^T$  and  $\mathbf{t} = (t_x, t_y, t_z)^T$  with respect to one face of the element, the rotation matrix  $T$  is given by

$$T = \begin{pmatrix} T^\sigma & 0 \\ 0 & T^v \end{pmatrix} \in \mathbb{R}^{9 \times 9}. \quad (2.12)$$

$T^\sigma \in \mathbb{R}^{6 \times 6}$  corresponds to the rotation matrix for the stress tensor rotation and is explicitly written as

$$T^\sigma = \begin{pmatrix} n_x^2 & s_x^2 & t_x^2 & 2n_x s_x & 2s_x t_x & 2n_x t_x \\ n_y^2 & s_y^2 & t_y^2 & 2n_y s_y & 2s_y t_y & 2n_y t_y \\ n_z^2 & s_z^2 & t_z^2 & 2n_z s_z & 2s_z t_z & 2n_z t_z \\ n_y n_x & s_y s_x & t_y t_x & n_y s_x + n_x s_y & s_y t_x + s_x t_y & n_y t_x + n_x t_y \\ n_z n_y & s_z s_y & t_z t_y & n_z s_y + n_y s_z & s_z t_y + s_y t_z & n_z t_y + n_y t_z \\ n_z n_x & s_z s_x & t_z t_x & n_z s_x + n_x s_z & s_z t_x + s_x t_z & n_z t_x + n_x t_z \end{pmatrix}, \quad (2.13)$$

whereas  $T^v \in \mathbb{R}^{3 \times 3}$  is the rotation matrix for the velocity tensor and given as

$$T^v = \begin{pmatrix} n_x & s_x & t_x \\ n_y & s_y & t_y \\ n_z & s_z & t_z \end{pmatrix}. \quad (2.14)$$

Within the *face-aligned* coordinate system, we follow the concept of exact Riemann solver to compute the state at element interfaces by upwinding (e.g. Toro, 1999). We decompose the surface integral into the sum of integrals over the individual element faces. For one interface between the actual element ( $m$ ) and its neighbor element ( $m_j$ ) the so-called *Godunov flux* reads

$$F_p^h = \frac{1}{2} T_{pq} (A_{qr}^{(m)} + |A_{qr}^{(m)}|) (T_{rs})^{-1} Q_s^{(m)} + \frac{1}{2} T_{pq} (A_{qr}^{(m)} + |A_{qr}^{(m)}|) (T_{rs})^{-1} Q_s^{(m_j)}, \quad (2.15)$$

where  $Q_s^{(m)}$  and  $Q_s^{(m_j)}$  are the boundary extrapolated values of the numerical solution from element  $\mathcal{T}^{(m)}$  and the  $j$ th-side neighbor  $\mathcal{T}^{(m_j)}$ , respectively. Only the Jacobian matrix  $A_{qr}^{(m)}$  of Eq. (2.2) in  $x$ -direction contributes to the flux term due to the rotation.

The given setting as in the present case for the flux term is known as the Riemann problem: Solving a PDE with a discontinuity as an initial condition. We know, that a number of waves given by the amount of eigenvectors and eigenvalues from the Jacobian  $A$  will be generated. These waves propagate with the speeds given in (2.3). For each

boundary face the outgoing as well as the incoming flux has to be considered. Furthermore, only those waves must contribute which have the correct travel direction. This means, positive normal direction for outgoing and negative direction for incoming. Eq. (2.15) account for above, if we define

$$|A_{qr}| = R_{qp}^A |\Lambda_{ps}| (R_{sr}^A)^{-1}, \quad \text{with} \quad |\Lambda_{ps}| = \text{diag}(|\alpha_1|, |\alpha_2|, \dots), \quad (2.16)$$

where  $\mathbf{R}^A$  denotes the matrix of the right eigenvectors  $R_{p1}^A, \dots, R_{p9}^A$  of the Jacobian  $A$ :

$$\mathbf{R}^A = \begin{pmatrix} \lambda + 2\mu & 0 & 0 & 0 & 0 & 0 & 0 & 0 & \lambda + 2\mu \\ \lambda & 0 & 0 & 0 & 1 & 0 & 0 & 0 & \lambda \\ \lambda & 0 & 0 & 0 & 0 & 1 & 0 & 0 & \lambda \\ 0 & \mu & 0 & 0 & 0 & 0 & 0 & \mu & 0 \\ 0 & 0 & 0 & 1 & 0 & 0 & 0 & 0 & 0 \\ 0 & 0 & \mu & 0 & 0 & 0 & \mu & 0 & 0 \\ c_p & 0 & 0 & 0 & 0 & 0 & 0 & 0 & -c_p \\ 0 & c_s & 0 & 0 & 0 & 0 & 0 & -c_s & 0 \\ 0 & 0 & c_s & 0 & 0 & 0 & -c_s & 0 & 0 \end{pmatrix}. \quad (2.17)$$

Independent of the used degree of the basis functions only direct neighbors exchange information via fluxes. Besides this welcome and important feature for parallel computing, *Godunov fluxes* are intrinsically dissipative. In fact, the amount of numerical dissipation depends on the frequency and the order  $\mathcal{O}$  of the scheme. At a certain point, an effective high-frequency cutoff that depends on the element size is reached (Hesthaven and Warburton, 2008, p.90, Fig. 4.1). Hence, short wavelengths that are not well resolved by a certain grid spacing are adaptively damped, without leading to numerical instabilities or affecting longer wavelengths. In particular, this attribute of the exact Riemann solver becomes extremely important for the implementation of spontaneous rupture sources as elaborated in Chapter 5.

Inserting Eqs. (2.5) and (2.15) in Eq. (2.10) we obtain the semi-discrete DG formulation:

$$\begin{aligned} & \frac{\partial}{\partial t} \hat{Q}_{pl}^{(m)} \int_{\mathcal{T}^{(m)}} \Phi_k \Phi_l dV \\ & + \sum_{j=1}^4 \frac{1}{2} T_{pq}^j \left( A_{qr}^{(m)} + |A_{qr}^{(m)}| \right) (T_{rs}^j)^{-1} \hat{Q}_{sl}^{(m)} \int_{(\partial\mathcal{T}^{(m)})_j} \Phi_k^{(m)} \Phi_l^{(m)} dS \\ & + \sum_{j=1}^4 \frac{1}{2} T_{pq}^j \left( A_{qr}^{(m)} - |A_{qr}^{(m)}| \right) (T_{rs}^j)^{-1} \hat{Q}_{sl}^{(m_j)} \int_{(\partial\mathcal{T}^{(m)})_j} \Phi_k^{(m)} \Phi_l^{(m_j)} dS \\ & - A_{pq} \hat{Q}_{ql}^{(m)} \int_{\mathcal{T}^{(m)}} \frac{\partial \Phi_k}{\partial x} \Phi_l dV - B_{pq} \hat{Q}_{ql}^{(m)} \int_{\mathcal{T}^{(m)}} \frac{\partial \Phi_k}{\partial y} \Phi_l dV - C_{pq} \hat{Q}_{ql}^{(m)} \int_{\mathcal{T}^{(m)}} \frac{\partial \Phi_k}{\partial z} \Phi_l dV = 0. \end{aligned} \quad (2.18)$$

As mentioned above, the surface integral is split into the sum over the four parts corresponding to the triangular element faces. One sum refers to the outgoing flux and the other one for the incoming flux of the neighbor, respectively. Note, that only the space dependent basis functions remain under the volume and surface integrals.

In the next Section, we will demonstrate how we transform the semi-discrete DG formulation of Eq. (2.18) into a reference coordinate system to reduce the computational effort.

### 2.3.3. Coordinate Transformation into Reference Element

Equation (2.18) is formulated in the global and physical  $xyz$ -coordinate system. As already introduced in the beginning of Section 2.3 and Fig. 2.1, each tetrahedron  $\mathcal{T}^{(m)}$  is transformed to a canonical reference tetrahedron  $\mathcal{T}_{ref}$  in order to precompute and store identical integrals.

The resulting influence on the integration variables is

$$dx dy dz = |\mathbf{J}| d\xi d\eta d\zeta, \quad (2.19)$$

where  $|\mathbf{J}|$  is the determinant of the Jacobian matrix of the transformation as given in Appendix B, Eq. (B.2). The transformed gradients have the form

$$\begin{pmatrix} \frac{\partial}{\partial x} \\ \frac{\partial}{\partial y} \\ \frac{\partial}{\partial z} \end{pmatrix} = \begin{pmatrix} \frac{\partial \xi}{\partial x} & \frac{\partial \eta}{\partial x} & \frac{\partial \zeta}{\partial x} \\ \frac{\partial \xi}{\partial y} & \frac{\partial \eta}{\partial y} & \frac{\partial \zeta}{\partial y} \\ \frac{\partial \xi}{\partial z} & \frac{\partial \eta}{\partial z} & \frac{\partial \zeta}{\partial z} \end{pmatrix} \begin{pmatrix} \frac{\partial}{\partial \xi} \\ \frac{\partial}{\partial \eta} \\ \frac{\partial}{\partial \zeta} \end{pmatrix}. \quad (2.20)$$

Before we proceed, we define

$$\begin{aligned} A_{pq}^* &= A_{pq} \frac{\partial \xi}{\partial x} + B_{pq} \frac{\partial \xi}{\partial y} + C_{pq} \frac{\partial \xi}{\partial z}, \\ B_{pq}^* &= A_{pq} \frac{\partial \eta}{\partial x} + B_{pq} \frac{\partial \eta}{\partial y} + C_{pq} \frac{\partial \eta}{\partial z}, \\ C_{pq}^* &= A_{pq} \frac{\partial \zeta}{\partial x} + B_{pq} \frac{\partial \zeta}{\partial y} + C_{pq} \frac{\partial \zeta}{\partial z}. \end{aligned} \quad (2.21)$$

In consideration of Eqs. (2.19), (2.20) and (2.21), the semi-discrete DG formulation of Eq. (2.18) transforms into

$$\begin{aligned} & \frac{\partial}{\partial t} \hat{Q}_{pl}^{(m)} |\mathbf{J}| \int_{\mathcal{T}_{ref}} \Phi_k \Phi_l d\xi d\eta d\zeta \\ & + \sum_{j=1}^4 T_{pq}^j \frac{1}{2} \left( A_{qr}^{(m)} + \left| A_{qr}^{(m)} \right| \right) (T_{rs}^j)^{-1} \hat{Q}_{sl}^{(m)} |S_j| F_{kl}^{-,j} \\ & + \sum_{j=1}^4 T_{pq}^j \frac{1}{2} \left( A_{qr}^{(m)} - \left| A_{qr}^{(m)} \right| \right) (T_{rs}^j)^{-1} \hat{Q}_{sl}^{(m_j)} |S_j| F_{kl}^{+,j,i,h} \\ & - A_{pq}^* \hat{Q}_{ql}^{(m)} |\mathbf{J}| \int_{\mathcal{T}_{ref}} \frac{\partial \Phi_k}{\partial \xi} \Phi_l d\xi d\eta d\zeta \\ & - B_{pq}^* \hat{Q}_{ql}^{(m)} |\mathbf{J}| \int_{\mathcal{T}_{ref}} \frac{\partial \Phi_k}{\partial \eta} \Phi_l d\xi d\eta d\zeta \\ & - C_{pq}^* \hat{Q}_{ql}^{(m)} |\mathbf{J}| \int_{\mathcal{T}_{ref}} \frac{\partial \Phi_k}{\partial \zeta} \Phi_l d\xi d\eta d\zeta = 0, \end{aligned} \quad (2.22)$$

where  $|S_j|$  denotes the area of face  $j$ . At this point, the mass matrix  $M$  and the stiffness matrices  $K$  are introduced

$$M_{kl} = \int_{\mathcal{T}_{ref}} \Phi_k \Phi_l d\xi d\eta d\zeta, \quad (2.23)$$

Table 2.1.: Face definition on tetrahedrons.

Face	Points
1	1 3 2
2	1 2 4
3	1 4 3
4	2 3 4

$$K_{kl}^{\xi} = \int_{\mathcal{T}_{ref}} \frac{\partial \Phi_k}{\partial \xi} \Phi_l d\xi d\eta d\zeta, \quad (2.24)$$

$$K_{kl}^{\eta} = \int_{\mathcal{T}_{ref}} \frac{\partial \Phi_k}{\partial \eta} \Phi_l d\xi d\eta d\zeta, \quad (2.25)$$

$$K_{kl}^{\zeta} = \int_{\mathcal{T}_{ref}} \frac{\partial \Phi_k}{\partial \zeta} \Phi_l d\xi d\eta d\zeta. \quad (2.26)$$

Obviously, these integrals can be precomputed by a computer algebra system (e.g. Maple or Matlab). Furthermore, the flux matrices  $F_{kl}^{-,j}$  and  $F_{kl}^{+,j,i,h}$  in Eq. (2.22) can be calculated analytically once on the reference element employing Eq. (2.27) as shown in the following.

First, the local faces and their local vertex ordering are defined according to Table 2.1. The vertex numbering is strictly counter-clockwise as seen in Fig 2.1. Furthermore, the vector of volume coordinates  $\boldsymbol{\xi}$  is given on the faces by mapping functions from the face parameters  $\chi$  and  $\tau$ , as shown in Table 2.2(a). For the flux computation over the face, integrations along the faces inside the local element  $\mathcal{T}^{(m)}$  as well as in the neighbor element  $\mathcal{T}^{(m_j)}$  are necessary. Hence, we transform the face parameters  $\chi$  and  $\tau$  inside the local element to the corresponding face parameters  $\tilde{\chi}$  and  $\tilde{\tau}$  in the neighbor face. This transformation depends on the orientation of the neighbor's face with respect to the local face of the considered element  $\mathcal{T}^{(m)}$ , as there may be three possible orientations due to the rotation of the triangular faces. Their mapping functions are given in Table 2.2(b).

Finally, all possible flux matrices in three dimensions are given by

$$\begin{aligned} F_{kl}^{-,j} &= \int_{\partial(\mathcal{T}_{ref})_j} \Phi_k \left( \boldsymbol{\xi}^{(j)}(\chi, \tau) \right) \Phi_l \left( \boldsymbol{\xi}^{(j)}(\chi, \tau) \right) d\chi d\tau, \\ F_{kl}^{+,j,i,h} &= \int_{\partial(\mathcal{T}_{ref})_j} \Phi_k \left( \boldsymbol{\xi}^{(j)}(\chi, \tau) \right) \Phi_l \left( \boldsymbol{\xi}^{(i)}(\tilde{\chi}^{(h)}(\chi, \tau), \tilde{\tau}^{(h)}(\chi, \tau)) \right) d\chi d\tau, \end{aligned} \quad (2.27)$$

for  $1 \leq j \leq 4$ ,  $1 \leq i \leq 4$  and  $1 \leq h \leq 3$ . The left state flux matrix (superscript '-')  $F_{kl}^{-,j}$  refers to the contribution to the fluxes over face  $j$  of the element  $\mathcal{T}^{(m)}$  itself. And, the right state flux matrix (superscript '+')  $F_{kl}^{+,j,i,h}$  refers to the contribution to the fluxes over the face  $j$  of the element's direct side neighbor  $\mathcal{T}^{(m_j)}$ . Index  $1 \leq i \leq N_E$  denotes the local number of the common face from the perspective of its neighbor  $\mathcal{T}^{(m_j)}$  and depends

Table 2.2.: (a) 3D volume coordinates  $\xi^{(j)}$  as function of the face parameters  $\chi$  and  $\tau$ .  
 (b) Transformation of the face parameters  $\chi$  and  $\tau$  of the tetrahedron's face to the face parameters  $\tilde{\chi}$  and  $\tilde{\tau}$  in the neighbor tetrahedron according to the three possible orientations  $h$  of the neighbor face.

j	1	2	3	4
$\xi^{(j)}(\chi, \tau)$	$\tau$	$\chi$	0	$1 - \chi - \tau$
$\eta^{(j)}(\chi, \tau)$	$\chi$	0	$\tau$	$\chi$
$\zeta^{(j)}(\chi, \tau)$	0	$\tau$	$\chi$	$\tau$

(a)

$h$	1	2	3
$\tilde{\chi}^{(h)}(\chi, \tau)$	$\tau$	$1 - \chi - \tau$	$\chi$
$\tilde{\tau}^{(h)}(\chi, \tau)$	$\chi$	$\tau$	$1 - \chi - \tau$

(b)

on the mesh generator. Index  $1 \leq h \leq 3$  represents the number of the local node in the neighbor's face which matches the local vertex 1 of face  $j$  in tetrahedron  $\mathcal{T}^{(m)}$ . Index  $h$  also depends on the mesh generator. On a given mesh, where indices  $i$  and  $h$  are known, only four of the 48 possible matrices  $F_{kl}^{+,j,i,h}$  are used per element.

Including Eqs. (2.23)-(2.26), we reformulate Eq. (2.22) in a more compact way as

$$\begin{aligned}
 & \frac{\partial}{\partial t} \hat{Q}_{pl}^{(m)} |\mathbf{J}| M_{kl} \\
 & + \sum_{j=1}^4 T_{pq}^j \frac{1}{2} \left( A_{qr}^{(m)} + \left| A_{qr}^{(m)} \right| \right) (T_{rs}^j)^{-1} \hat{Q}_{sl}^{(m)} |S_j| F_{kl}^{-,j} \\
 & + \sum_{j=1}^4 T_{pq}^j \frac{1}{2} \left( A_{qr}^{(m)} - \left| A_{qr}^{(m)} \right| \right) (T_{rs}^j)^{-1} \hat{Q}_{sl}^{(m_j)} |S_j| F_{kl}^{+,j,i,h} \\
 & - \hat{Q}_{ql}^{(m)} |\mathbf{J}| \left( A_{pq}^* K_{kl}^\xi + B_{pq}^* K_{kl}^\eta + C_{pq}^* K_{kl}^\zeta \right) = 0.
 \end{aligned} \tag{2.28}$$

The next Section will explore the ADER time integration for the derived equation in the reference coordinate system to achieve a fully discretized expression of the elastodynamic system.

### 2.3.4. The High-order Accurate Time Discretization: ADER

Eq. (2.28) could be integrated in time by the Runge-Kutta method in order to obtain a quadrature free Runge-Kutta DG scheme (Atkins and Shu, 1998). However, due to the so-called Butcher barrier (Butcher, 1987), the efficiency for integrations of an order of accuracy greater than  $\mathcal{O}4$  decreases dramatically. As higher-order accuracy might be quite advantageous for propagating waves over many wavelengths the Arbitrary high-order DERivative (ADER) technique is applied. ADER enables efficient time integration

of very high orders while storing only one single time step level. The approach implies that the same approximation order in space and in time is achieved automatically.

Its main ingredients are a Taylor expansion in time, the solution of Derivative Riemann-Problems (DRP) (Toro and Titarev, 2002) to approximate the space derivatives at the interface and the Cauchy-Kovalewski procedure for replacing iteratively the time derivatives in the Taylor series by space derivatives. As mentioned in Section 2.1, the ADER approach was originally introduced by Toro *et al.* (2001) and later combined with DG formulations by Schwartzkopff *et al.* (2002); Dumbser and Munz (2005a,b) for linear hyperbolic systems.

For the development of the ADER-DG schemes, we start with the basic equation Eq. (2.2) but transformed in the reference system

$$\frac{\partial Q_p}{\partial t} + \left( A_{pq}^* \frac{\partial}{\partial \xi} + B_{pq}^* \frac{\partial}{\partial \eta} + C_{pq}^* \frac{\partial}{\partial \zeta} \right) Q_q = 0. \quad (2.29)$$

Then, we integrate for a time increment  $\Delta t$  assuming that origin time is  $t = 0$  without loss of generality

$$\int_0^{\Delta t} \frac{\partial Q_p}{\partial t} dt = - \int_0^{\Delta t} \left( A_{pq}^* \frac{\partial}{\partial \xi} + B_{pq}^* \frac{\partial}{\partial \eta} + C_{pq}^* \frac{\partial}{\partial \zeta} \right) Q_q dt. \quad (2.30)$$

The left hand side of the equation has the simple solution

$$\int_0^{\Delta t} \frac{\partial Q_p}{\partial t} dt = Q_p(\Delta t) - Q_p(0). \quad (2.31)$$

That means, we basically seek for the solution of the time integral of the right hand side

$$\int_0^{\Delta t} Q_p(t) dt, \quad (2.32)$$

which is not trivial to solve with high-order accuracy.

A key issue for the solution is the Cauchy-Kovalewski procedure applied to Eq. (2.29) which is given by

$$\frac{\partial^k Q_p}{\partial t^k} = (-1)^k \left( A_{pq}^* \frac{\partial}{\partial \xi} + B_{pq}^* \frac{\partial}{\partial \eta} + C_{pq}^* \frac{\partial}{\partial \zeta} \right)^k Q_q. \quad (2.33)$$

Hereby, the  $k$ th time derivative is expressed as a function of pure space derivatives. Apparently, the relationship is valid for  $k = 1$  as we obtain Eq. (2.29). The validation for  $k \geq 2$  is proved by complete induction in Käser and Dumbser (2006).

In the next step, we evaluate the solution of Eq. (2.29) as a Taylor series in time up to order  $N$ ,

$$Q_p(\xi, \eta, \zeta, t) = \sum_{k=0}^N \frac{t^k}{k!} \frac{\partial^k}{\partial t^k} Q_p(\xi, \eta, \zeta, 0), \quad (2.34)$$

and replace all time derivatives by space derivatives, using (2.33):

$$Q_p(\xi, \eta, \zeta, t) = \sum_{k=0}^N \frac{t^k}{k!} (-1)^k \left( A_{pq}^* \frac{\partial}{\partial \xi} + B_{pq}^* \frac{\partial}{\partial \eta} + C_{pq}^* \frac{\partial}{\partial \zeta} \right)^k Q_q(\xi, \eta, \zeta, 0). \quad (2.35)$$

We then use the Discontinuous Galerkin approximation (2.5) in order to get

$$Q_p(\xi, \eta, \zeta, t) = \sum_{k=0}^N \frac{t^k}{k!} (-1)^k \left( A_{pq}^* \frac{\partial}{\partial \xi} + B_{pq}^* \frac{\partial}{\partial \eta} + C_{pq}^* \frac{\partial}{\partial \zeta} \right)^k \Phi_l(\xi, \eta, \zeta) \hat{Q}_{ql}(0). \quad (2.36)$$

This approximation can now be projected onto each basis function to obtain an approximation of the evolution of the degrees of freedom during one time step from time level  $n$  to time level  $n + 1$ . We obtain

$$\hat{Q}_{pl}(t) = \frac{\left\langle \Phi_n, \sum_{k=0}^N \frac{t^k}{k!} (-1)^k \left( A_{pq}^* \frac{\partial}{\partial \xi} + B_{pq}^* \frac{\partial}{\partial \eta} + C_{pq}^* \frac{\partial}{\partial \zeta} \right)^k \Phi_m(\xi, \eta, \zeta) \right\rangle}{\langle \Phi_n, \Phi_l \rangle} \hat{Q}_{qm}(0), \quad (2.37)$$

where  $\langle a, b \rangle = \int_{\mathcal{T}_E} a \cdot b \, dV$  denotes the inner product over the reference tetrahedron  $\mathcal{T}_E$  and the division by  $\langle \Phi_n, \Phi_l \rangle$  denotes the multiplication with the inverse of the mass matrix. In fact, due to the orthogonality of the used basis functions, the mass matrix is diagonal and the multiplication simplifies to a division by its entries. Equation (2.37) can be integrated analytically in time and we obtain

$$\int_0^{\Delta t} \hat{Q}_{pl}(t) dt = \frac{\left\langle \Phi_n, \sum_{k=0}^N \frac{\Delta t^{(k+1)}}{(k+1)!} (-1)^k \left( A_{pq}^* \frac{\partial}{\partial \xi} + B_{pq}^* \frac{\partial}{\partial \eta} + C_{pq}^* \frac{\partial}{\partial \zeta} \right)^k \Phi_m(\xi, \eta, \zeta) \right\rangle}{\langle \Phi_n, \Phi_l \rangle} \hat{Q}_{qm}(0). \quad (2.38)$$

With the definition

$$I_{plqm}(\Delta t) = \frac{\left\langle \Phi_n, \sum_{k=0}^N \frac{\Delta t^{(k+1)}}{(k+1)!} (-1)^k \left( A_{pq}^* \frac{\partial}{\partial \xi} + B_{pq}^* \frac{\partial}{\partial \eta} + C_{pq}^* \frac{\partial}{\partial \zeta} \right)^k \Phi_m(\xi, \eta, \zeta) \right\rangle}{\langle \Phi_n, \Phi_l \rangle} \quad (2.39)$$

the time-integrated degrees of freedom in equation (2.38) can be expressed as

$$\int_0^{\Delta t} \hat{Q}_{pl}(t) dt = I_{plqm}(\Delta t) \hat{Q}_{qm}(0), \quad (2.40)$$

where  $I_{plqm}(\Delta t)$  represents a four-dimensional tensor including the Cauchy-Kovalewski procedure and  $\hat{Q}_{qm}(0)$  denotes the  $q \times m$ -matrix of the degrees of freedom at time level  $n$ . Finally, by integration of (2.22) in time all parts to assemble the fully discrete ADER-DG

scheme are derived and we obtain:

$$\begin{aligned}
& \left[ \left( \hat{Q}_{pl}^{(m)} \right)^{n+1} - \left( \hat{Q}_{pl}^{(m)} \right)^n \right] |J| M_{kl} \\
& + \frac{1}{2} \sum_{j=1}^4 T_{pq}^j \left( A_{qr}^{(m)} + \left| A_{qr}^{(m)} \right| \right) (T_{rs}^j)^{-1} |S_j| F_{kl}^{-,j} \cdot I_{slmn}(\Delta t) \left( \hat{Q}_{mn}^{(m)} \right)^n \\
& + \frac{1}{2} \sum_{j=1}^4 T_{pq}^j \left( A_{qr}^{(m)} - \left| A_{qr}^{(m)} \right| \right) (T_{rs}^j)^{-1} |S_j| F_{kl}^{+,j,i,h} \cdot I_{slmn}(\Delta t) \left( \hat{Q}_{mn}^{(m_j)} \right)^n \\
& - A_{pq}^* |J| K_{kl}^\xi \cdot I_{qlmn}(\Delta t) \left( \hat{Q}_{mn}^{(m)} \right)^n \\
& - B_{pq}^* |J| K_{kl}^\eta \cdot I_{qlmn}(\Delta t) \left( \hat{Q}_{mn}^{(m)} \right)^n \\
& - C_{pq}^* |J| K_{kl}^\zeta \cdot I_{qlmn}(\Delta t) \left( \hat{Q}_{mn}^{(m)} \right)^n = 0.
\end{aligned} \tag{2.41}$$

The scheme is quadrature-free and performs high order time-integration from time level  $t^n$  to  $t^{n+1}$  in one single step while communicating only with its direct neighbors. Furthermore, only the memory of a first order explicit Euler time stepping scheme is consumed. The high-order approximation in space and in time provides spectral convergence properties as verified in Käser and Dumbser (2006) and Dumbser and Käser (2006).

As every explicit time marching scheme, also the numerical stability of the ADER approach depends on a limited time step length according to the CFL criterion (Courant *et al.*, 1928). A rigorous von Neumann stability analysis can be found in Dumbser (2005). In the present case, the time step is bounded by

$$\Delta t^{(m)} \leq C \frac{1}{2N+1} \frac{l^{(m)}}{c_{max}^{(m)}}, \tag{2.42}$$

where  $l$  is the diameter of the inscribed sphere of tetrahedron ( $m$ ) and  $c_{max}$  the maximum wave speed depending on the element's material properties. The coefficient  $C$  denotes the CFL-number, which must necessarily be  $C \leq 0.7$  for stability and has to be chosen even smaller under certain circumstances. In most situations, a value of 0.5 has proven to be practical.

In general, the smallest  $\Delta t^{(m)}$  of all elements in the whole domain governs the time step length. Hence, a model discretization including only one single small tetrahedron could be extremely costly as all other elements are restricted by a potentially undersized time step. Note, it frequently happens that a mesh generator produces small or even deformed elements to better align the geometries of a given model. However, the ADER approach enables local time stepping (LTS) as introduced by Dumbser *et al.* (2007) to reduce the number of element updates. In a LTS scheme each element run its own optimal time step length respecting Eq. (2.42) without changing the fundamental properties of the ADER-DG method nor its accuracy. Due to different time step lengths, the update levels of neighboring elements do not match anymore. But, the required interpolation of element time levels needed by a consistent flux computation is automatically done the Cauchy-Kovalewski procedure as an accurate prediction of the evolution of the degrees of freedom during one time step is naturally given. The volume integrals are always computed for

the full local time step as they depend purely on the local element information. In fact, the interpolation for the flux computation causes some overhead. However, the approach can significantly reduce the computational time when element sizes are very different or material properties change strongly. For instance, such cases occur in borehole modeling for industrial applications (see Chapter 3) and strong ground motion simulations including low-velocity sedimentary layers. Hereby, LTS definitely pays off and give remarkable speed-up's compared to simulations with a global time stepping scheme.

## 2.4. Sources

In the previous documentation of the numerical scheme, possible sources have been neglected. As the focus of the thesis lies on the implementation of dynamic rupture physics, which is explained in detail in Chapter 5, the concept of standard sources is only briefly addressed in this Section.

In general, sources are handled as individual source time functions  $S_p = S_p(\mathbf{x}, t)$  acting on one or more variables  $p$  at an arbitrary position in the computational domain.  $\mathbf{S}$  can contain a complex time series (e.g. assumed slip of an earthquake, Ricker wavelet, Gaussian pulse), but also a Dirac Delta function to compute Green functions. Using a Dirac Delta function has the advantage that different source types can be convoluted on the resulting seismograms. This way, only one simulation is needed to test various source mechanism, if identical source origins are assumed. Classical sources, like the double-couple mechanism, are created by an appropriate combination of the relevant stress components in  $\mathbf{S}$ . If extended earthquake faults are modeled kinematically, many sources at various positions are used at the same time as input (Käser *et al.*, 2007).

The vector  $\mathbf{S}$  is mathematically introduced as a right hand side term in Eq. (2.2). Basically, the discretization as presented in this Chapter holds also in the case of considering an additional term. However, for a complete derivation including the source term the reader is referred to Käser and Dumbser (2006).

## 2.5. Boundary Conditions

An important piece of solving a PDE and of a realistic simulation is the boundary condition. Therefore, we will discuss three often used one in this Section. In a DG scheme a boundary condition affects solely the flux term. Although the dynamic rupture source implementation is mathematically a boundary condition, we will address this topic in Chapter 5.

### 2.5.1. Free-Surface Boundaries

If acoustic emission can be neglected, we can model the Earth surface as a free surface. This is realized by imposing the normal and shear stresses perpendicular to the free surface to be zero. Thereby, we use the incoming flux to mirror exactly those components with the aid of matrix  $\Lambda = \text{diag}(-1, 1, 1, -1, 1, -1, 1, 1, 1)$ . Then, the flux term at an element

side adjacent to a free surface reads:

$$\begin{aligned} F_p^{\text{FreeSurfaceBC}} &= \frac{1}{2} T_{pq} (A_{qr}^{(m)} + |A_{qr}^{(m)}|) (T_{rs})^{-1} Q_s^{(m)} \\ &+ \frac{1}{2} T_{pq} (A_{qr}^{(m)} + |A_{qr}^{(m)}|) \Lambda_{rs} (T_{st})^{-1} Q_s^{(m)}. \end{aligned} \quad (2.43)$$

### 2.5.2. Absorbing Boundaries

Many applications are on a regional or even smaller scale. E.g. strong ground motion models range over a few tens or hundred kilometers and industrial applications sometimes go down to meter scale. Instead of modeling the whole Earth only chunks are considered in such cases leading to artificial bounded domains. At those boundaries, waves should simply travel outwards of the model. To this end, we set the incoming flux values of Eq. (2.15) to zero at the corresponding site of a boundary element:

$$F_p^{\text{AbsorbingBC}} = \frac{1}{2} T_{pq} (A_{qr}^{(m)} + |A_{qr}^{(m)}|) (T_{rs})^{-1} Q_s^{(m)}. \quad (2.44)$$

Unfortunately, the mathematical problem is ill-posed for waves with shallow incident angle causing unwanted reflections of significant amplitude. Therefore, many approaches, e.g. exact working absorbing boundaries or Convolutional Perfectly Matched Layers (CPML), to improve the behavior of absorbing boundaries can be found in the literature (e.g. Engquist and Majda, 1979; Givoli and Keller, 1990; Givoli *et al.*, 2006; Roden and Gedney, 2000). However, the improvement of better absorbing boundaries is a non-trivial task and still ongoing research.

### 2.5.3. Periodic Boundaries

Periodic boundary conditions are an important concept for accuracy studies of the method and convergence tests. Waves traveling out of the domain at one side enter the model again on the opposite side. Due to this trick, propagation over many wavelengths can be simulated without unnecessarily increasing the computational domain. Essentially, the surface meshes at the boundaries of opposing faces have to match exactly.

## 2.6. Computational Aspects

So far, several practical aspects regarding computational science have not been addressed in this thesis yet, although they play a major role in the choice of which numerical forward solver should be used for an actual application.

The flexibility of tetrahedral meshing was only touched in Section 2.1, but the model building is an important and potentially time consuming part in the workflow and will dictate the overall accuracy of the simulation. Usually, the first step is to create the model geometry in a Computer Aided Design (CAD) tool by volumes and surfaces. In some cases, the actual mesh generator provides some CAD capabilities, e.g. ANSYS ICEM CFD and Gambit. Then, the element size has to be chosen carefully in order to guarantee

an accurate experiment according to the geological material properties, the demands of the geometry, and the frequency of the propagated signal. Taking this information as input, the meshing software creates a mesh almost automatically. However, this statement is valid for tetrahedral meshes. The experience has shown that hexahedral element generation is a very time consuming task and requires a degree of manual manipulation which should not be underestimated. Furthermore, although deformable hexahedral elements can nowadays be used in modern forward simulators, they are less flexible than tetrahedral grids when meshing complex topography and undulating interior material interfaces. On the other hand, a tetrahedral mesh is computational more expensive than a hexahedral discretization. Before the model setup is tackled the user should decide which approach is more appropriated in the particular situation. To overcome this issue, Hermann *et al.* (2011) developed an approach to combine different element types to reduce the costs further while keeping the possibility of using tetrahedral elements.

As many interesting applications lead to a huge number of elements, the workload is divided into many smaller tasks each solved in parallel by a distinct processor in a so-called HPC-cluster to accomplish the simulation in an acceptable time period. As the resulting communication takes place only between direct neighbors, a good scalability on HPC architectures is achieved (see Section 3.3). The technical realization of the data exchange between processors is performed by the Message Passing Interface (MPI) libraries and the partition into smaller subdomains by the free software METIS (Karypis and Kumar, 1998). If all elements are of equal computational cost, a perfect load balance between the used cores is reached when every subdomain contains the same amount of elements. Of course, a minimal surface to volume ratio is also desired. Situation is different when LTS or  $p$ -adaptivity are applied. In this case, the load balance is improved by grouping elements of similar computational cost and distribute a subdomain out of each group to every processor.

Illustration of the modeled wavefield is often very helpful for the interpretation of the experiment. Considering computations on thousands of cores, a huge amount of data is produced in order to provide snapshots of the wavefield. In the current implementation, every core processes only a small part of elements out of the full computational domain. Therefore, each node writes only its own results into a file on the hard drive. In a post-processing step, all the files of each node have to be gathered and ported into a proper format of the used visualization tool. This can be done on a local workstation as well as the visualization with commonly used tools as Matlab, Tecplot and Paraview.



## Chapter 3.

# Wave Field Modeling in Exploration Seismology Using the Discontinuous Galerkin Finite Element Method on HPC-infrastructure

### 3.1. Introduction

Seismic and acoustic measurements in a broad sense, including surface seismic, borehole seismic and sonic waveforms, play an important role in improving our knowledge of hydrocarbon reservoirs in both exploration and production phases. In that context, accurate modeling of wave propagation, in particular when considering irregular free-surface effects, complicated subsurface geological structures, or the physics of a sonic tool deployed downhole, is one of the major challenges geophysicists are facing.

We present a Discontinuous Galerkin (DG) finite element method, recently developed in computational seismology for the application on High Performance Computing (HPC) facilities, and illustrate its potential for seismic and sonic modeling in oil and gas exploration.

The exploration industry has developed a broad spectrum of techniques to initially detect, accurately survey, and constantly monitor these reservoirs to supply our still increasing demand of fossil fuels. Typically, surface seismic acquisitions are characterized with sources at or near free-surface and 3D multi-component seismic data that are recorded either at the free-surface or eventually at the sea-bottom using ocean-bottom-cables (OBC). With a typical frequency bandwidth of about 5-250 Hz the flexibility and density of source and receiver distributions provide a wide lateral coverage of the prospected area that ranges on a scale of several square kilometers. Borehole seismic surveys are characterized with sources either at the surface (e.g. 3D VSP) or downhole (cross-well imaging, micro-seismic events localization) with receivers in the borehole close to the targeted reservoir. They provide complementary information, as compared to surface seismic interpretation, by shedding more light onto particular structures of the reservoir that are up to several hundred meters away from the wellbore. For much higher depth-resolution imaging (typically 0.5 ft) along the wellbore sonic measurements with frequencies of 1-5 kHz are used to

---

This chapter presents the work of Martin Käser, Christian Pelties, Cristóbal E. Castro, Hugues Djikpesse and Michael Prange published in *The Leading Edge* (2010) in a slightly modified form.

derive, for instance, lithology properties and rock textures at different depths. They are also used, when deemed necessary, to analyze borehole stability, borehole mud invasion and any formation damage up to a few meters away from the wellbore.

For instance, independent of the scale of the problem, seismic and sonic waves within this broad frequency range are used to extract reservoir structural characteristics and compositional properties. The underlying inversion and migration techniques often rely on accurate synthetic data produced via special forward modeling tools. Solving the forward problem, in this case, means solving the full 3D seismic wave equations. This way, synthetic datasets of seismograms recorded at desired locations are generated for a given velocity model and source characteristics. Another application of wave propagation simulations is in the design of survey geometries and parameters to save valuable resources. The generation of highly accurate and reliable synthetic data incorporating all important model features can be challenging, but represents an absolutely crucial prerequisite. The importance as well as the difficulties to produce such data sets are emphasized by the foundation of the SEG Advanced Modeling (SEAM) project (Fehler, 2009), which is dedicated to large-scale geophysical modeling in industry. New numerical methods can provide such synthetics, even though they might still be computationally more involved than standard techniques, like finite differences (FD) due to their better approximation capabilities. Thus, future developments aim for strong interconnections between flexible and accurate numerical simulation methods and powerful computational resources such as those provided by current HPC-facilities.

In this article, we present the Discontinuous Galerkin finite element method to emphasize its advantages and future potential, especially for seismic modeling in the exploration industry. In the following, the principles of this numerical scheme are explained and its promising properties with respect to HPC-hardware are discussed. Two 3D examples occurring in seismic exploration demonstrate the method's applicability and flexibility on a span of scales: a marine seismic survey on the kilometer scale and sonic logging on the centimeter to meter depth-scale.

## 3.2. Discontinuous Galerkin Method

As computational modeling techniques are becoming increasingly important in all fields of seismology over the last decades, various innovative numerical methods have been developed. A new approach introduced for the simulation of seismic wave propagation by Käser and Dumbser (2006) is the Discontinuous Galerkin (DG) finite element approach. In particular, its combination with the explicit time integration method of Titarev and Toro (2002) using Arbitrary high-order DERivatives (ADER) leads to a high-order accuracy in both space and time. The extension of the method to 3D unstructured tetrahedral meshes (Dumbser and Käser, 2006) enables the use of automatic mesh generation for complex model geometries. Furthermore, a number of different material properties can be considered, such as acoustic fluids and elastic, anisotropic, viscoelastic or poroelastic solids (de la Puente *et al.*, 2007, 2008; de la Puente, 2008). Therefore, the ADER-DG scheme provides extremely high flexibility with respect to a wide range of wave propagation problems. The numerical method belongs to the class of Finite Element (FE) meth-

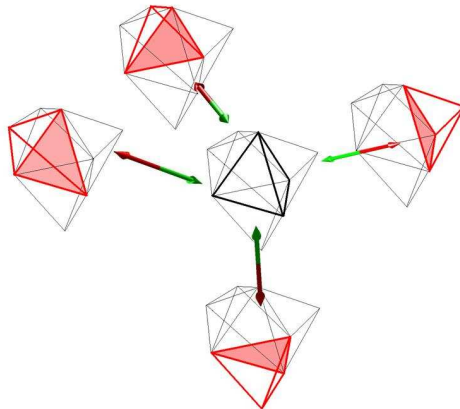


Figure 3.1.: Tetrahedral element with its direct neighbor elements for minimal communication across their common interfaces (red).

ods, but uses the Discontinuous Galerkin approach (e.g. Cockburn *et al.*, 2000; Hesthaven and Warburton, 2008). Here, the approximating 3D polynomials inside each element are allowed to be discontinuous along interfaces between neighboring elements in contrast to classical FE schemes. These discontinuities are then treated as in high-order Finite Volume (FV) methods using the well-established theory of Riemann problems and Riemann solvers (e.g. Toro, 1999). While the degree of the approximation polynomials determines the spatial order of accuracy, the ADER time integration approach provides the same time accuracy. Thereby, the time extrapolation of the solution to future time levels uses a Taylor expansion where higher-order time derivatives are replaced by space derivatives via a recursive use of the velocity-stress wave equation. A further advantage is that the polynomial basis functions are orthogonal which leads to a diagonal mass matrix. In fact, such basis functions exist for many different element types, e.g. triangles, quadrilaterals, tetrahedrons, hexahedrons, pyramids, and prisms. Furthermore, the scheme's extension to higher approximation orders does not require an increased stencil as typically necessary for FV or FD schemes. Instead, only the number of degrees of freedom, i.e. the polynomial coefficients, inside an element increases. Therefore, the numerical algorithm keeps a spatially local character as each time update of the solution inside one element only depends on the minimum number of direct neighbors sharing a common interface as shown in Figure 3.1. At these interfaces the concept of numerical fluxes is a key ingredient and strength of the ADER-DG method as it allows for a variety of physical effects to be accommodated: boundary conditions, friction laws for dynamic rupture processes, or the combination of different element types and non-conforming mesh transitions.

In order to focus the computational effort on particular areas of interest local adaptation of the approximation order and local time stepping is possible. Especially, the local time stepping approach allows each element to use its own optimal time step length according to the local stability condition. Hence, these features increase the performance and efficiency in models with strongly varying element sizes without losing accuracy.

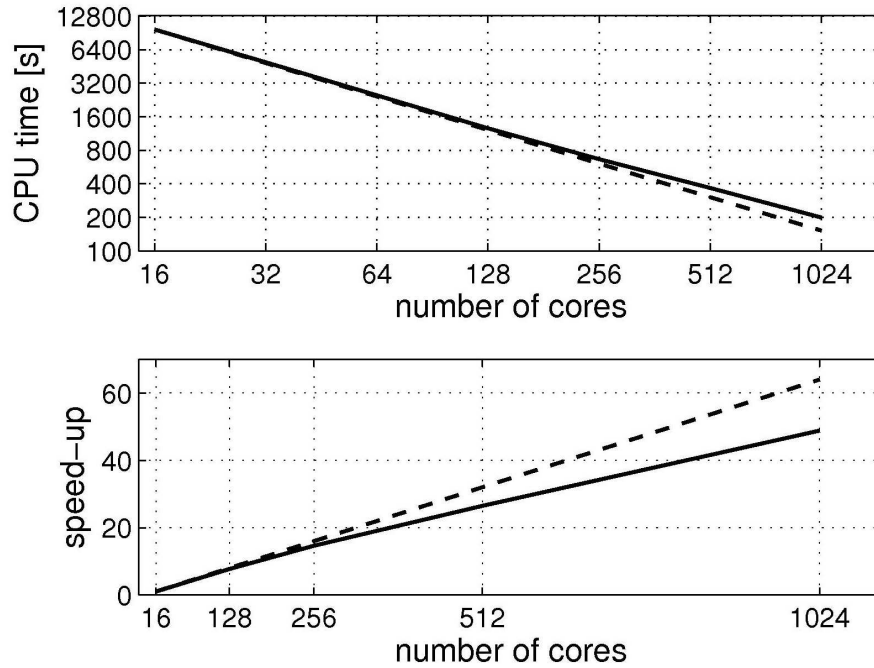


Figure 3.2.: CPU time decrease (top) and speed-up (bottom) for an increasing number of cores for the strong-scaling test (solid) in comparison to the theoretically ideal case (dashed).

### 3.3. Suitability for HPC-Infrastructure

A major advantage of the ADER-DG scheme is its locality as an element updated in time only requires information from the direct neighbors in form of polynomial coefficients. This property does not change with increasing approximation order as only the amount of coefficients grows. Therefore, the scheme is well-suited for parallelization. In fact, communication between elements takes place only once per time step and represents much less than 1% of the CPU-time. The results of a strong-scaling test for the borehole application shown below, where the model size, i.e. the total number of elements, remains constant ( $\sim 1.3 \cdot 10^6$ ) but the number of cores increases, are shown in Figure 3.2. The CPU-time reduction remains still close to the ideal case and the speed-up is satisfactory up to 1024 cores with an efficiency of 76%. The crucial issue for the scaling properties of the algorithm is the load balance which depends on the mesh partitioning strategy. For a standard, global time stepping scheme, where all elements are updated to the next time level, optimal load balance is achieved by dividing the computational domain into subdomains with the same number of elements. However, the local time stepping approach yields more difficulties as each element runs its own time step. Therefore, element updates happen asynchronously as smaller elements update more often than larger ones. The resulting load imbalances are currently overcome by grouping elements into zones, partition each zone separately as shown in Figure 3.3(c), and spread the parts equally to different cores.

Order $\mathcal{O}$	1	2	3	4	5	6	7	8
$m$ (DOF per element)	1	4	10	20	35	56	84	120
$M_e$ (memory per element [bytes])	2664	2880	3312	4032	5112	6624	8640	11232
$10^3$ elements per core $M_c = 0.5$ GB	200	180	160	130	100	80	60	45

Table 3.1.: Number  $m$  of degrees of freedom (DOF), memory consumption  $M_e$  per element, and an estimate of the element number per core of  $M_c = 0.5$  GB memory in dependence of approximation order.

Therefore, significant improvements of the algorithm should be achieved by run-time optimization of the serial part of the code. In fact, each tetrahedral element update requires the computation of three volume integrals and eight flux integrals (two per element face). Each of these integral computations consists of local matrix multiplications where three matrices of dimensions  $9 \times 9$ ,  $9 \times m$ , and  $m \times m$  are related to the nine velocity-stress variables and the number  $m$  of degrees of freedom (DOF), which depend on the degree  $N$  of the approximation polynomial as  $m = (N + 1)(N + 2)(N + 3)/6$ .

Memory consumption is not an issue as all data can be kept in arrays for each core. For every element there are  $9 \times m$  degrees of freedom and  $9 \times 9$  entries of the Jacobian matrices as double-precision real numbers to store in memory. In contrast, volume and flux integral matrices of size  $m \times m$  are element-independent and have to be kept in memory only once. Table 3.1 shows the memory requirement and the estimated maximum number of elements on an IBM BlueGene architecture with  $M_c = 0.5$  GB of memory per core with respect to the approximation order  $\mathcal{O}$ .

The 3D wave equations in velocity-stress formulation contain nine unknowns (six stresses and three velocities), each of which is approximated by the DOF inside an element leading to a  $9 \times m$  matrix. Furthermore, each element side has its own  $9 \times 9$  matrix of flux-orientation and material information. Therefore, the total memory per tetrahedral element is given by  $M_e = (9 \cdot m + 4 \cdot 9^2) \cdot 8$  bytes as given in Table 3.1. Note that the estimate of elements per core considers the memory requirement of a few MB for additional data, e.g. volume and flux matrices, basis functions, mesh coordinates, etc. Other architectures like the SGI Altix system or the IBM Power 6 often have 2 GB or 4 GB of memory per core and therefore can accommodate correspondingly more elements.

## 3.4. Applications

The applicability and geometrical flexibility of the ADER-DG method using 3D unstructured tetrahedral meshes is demonstrated in the following two examples relevant in hydrocarbon reservoir exploration. The examples are chosen to show the wide range of applications from borehole sonic measurements on the centimeter scale up to fully 3D salt

reservoir models on the kilometer scale. Both problems are solved on HPC-facilities of SGI and IBM.

### 3.4.1. Borehole-Scale Modeling

Sonic logging is one of the common techniques to estimate the geophysical and petrophysical properties (especially velocities and porosity) of the penetrated formation with a depth resolution of  $\sim 0.5$  ft. To validate sonic measurements via acoustic wave propagation modeling it turns out to be fundamental to consider the model geometry and heterogeneous material distribution in and around the well. In Figure 3.3(a) we sketch a setup of a sonic logging experiment, where a logging tool is placed inside a fluid-filled well penetrating an interbedded formation of two different materials. It is assumed that a steel casing separates the borehole fluid from a damaged formation zone. Due to the damage of the formation around the wellbore the drilling fluid (mud) typically causes an invasive zone leading to a nearly radial material gradient of a few meters away from the well. In our study, we investigate the effect of the steel casing on sonic measurements and the importance of the material gradient with respect to the recorded signals. To this end, we use an explosive source at the lower end of the tool and 25 equally spaced receivers along the tool as sketched in Figure 3.3(a). In Figure 3.3(b) we show a cut through the 3D mesh where the ratio between smallest and largest elements (here  $\sim 50$ ) is visible. The mesh of the fluid and the uppermost layers is omitted for better visualization of the geometry. In this case, the local time step algorithm particularly pays off, as the steel tool and casing force the usage of extremely small elements ( $\sim 1$  inch edge length), but yield a P-wave speed of 5000 m/s. This parameters lead to a time step length of  $\sim 1 \mu\text{s}$  in these elements. Figure 3.3(c) shows the mesh partition strategy, where each color represents a different subdomain. Note that the tool, fluid, casing, and formation are partitioned individually via the separation into zones. Then subdomains of each zone are collected and put to one core to achieve an acceptable load balance as in the local time stepping approach smaller elements are computationally more expensive than larger ones. Comparisons show, that the local time step approach is about three times faster than a global time step algorithm for this application.

Table 3.2 gives the material properties of the steel tool and casing, the fluid, and the geological formation for our tests. First we consider a cased well and a material gradient around the well of 2 m radius where the properties change linearly from the bore fluid to the unperturbed formation values. The interbedded layers consist of material 1 and 2 producing a synthetic data set shown in blue in Figure 3.4(a). Enhancing the material contrast by replacing material 2 by material 3 results in virtually the same dataset (shown in red). However, we obtain clear differences by removing the casing and repeating the experiments as shown by the green and black data in Figure 3.4(a). Obviously, the casing strongly obscures the effect of different material properties on the seismogram. In a second series of tests, we omit the gradient and use the unaltered material properties of the formation directly adjacent to the wellbore. In this case, the casing again has a larger effect on the seismograms than the material contrasts in the formation. In fact, the removal of the casing leads to increasing phase shifts of later arrivals in the seismograms.

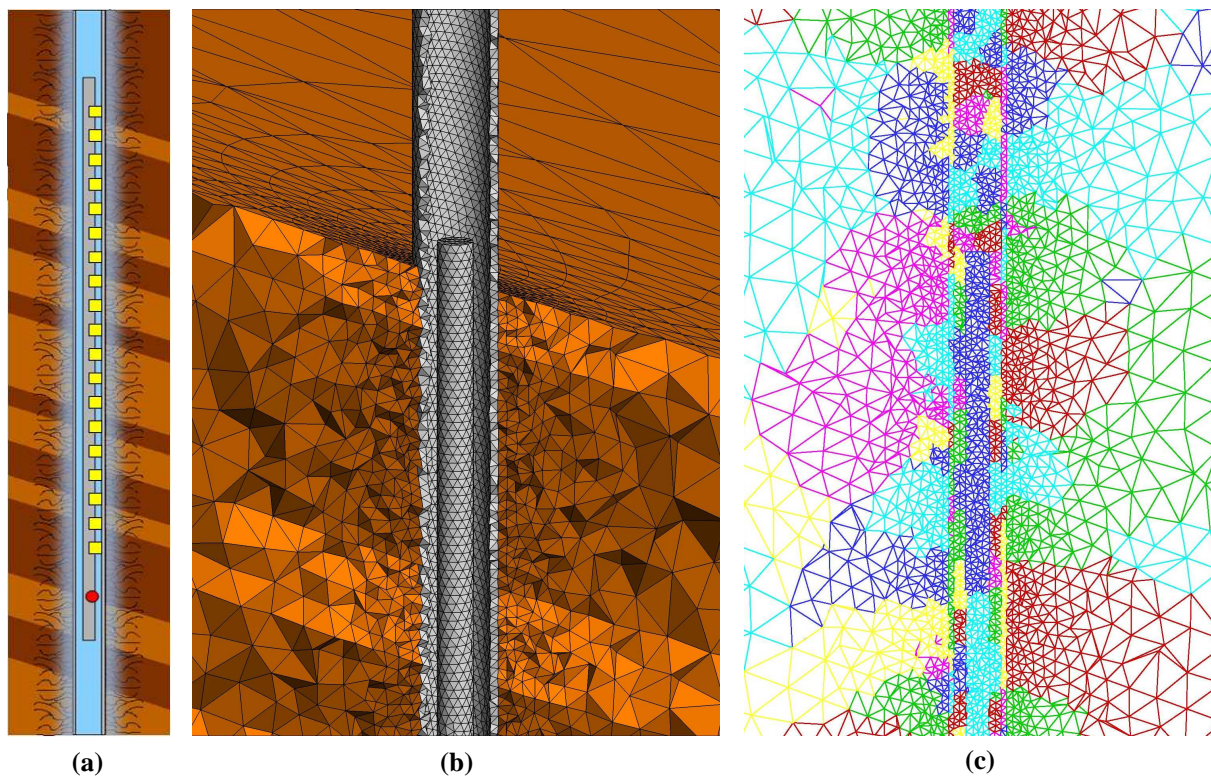


Figure 3.3.: Problem setup for sonic logging. (a) Sonic logging tool in a cased, fluid-filled borehole penetrating a formation of tilted layers with an invasive zone of mud in the vicinity of the well. (b) Sketch of the sliced 3D model discretized by a problem-adapted tetrahedral mesh. (c) 2D projection of a cut through the 3D mesh showing the zonal partitioning approach for multi-processor computations, where different colors represent the subdomains processed on different cores.

	$\rho$ [kg/m <sup>3</sup> ]	$\lambda$ [10 <sup>9</sup> Pa]	$\mu$ [10 <sup>9</sup> Pa]	$v_p$ [m/s]	$v_s$ [m/s]
tool/casing	7800	65.0000	65.0000	5000	2887
bore fluid	1020	2.2950	0.0000	1500	0
material 1	2700	14.5480	14.5480	4020	2321
material 2	2700	13.5480	13.5480	3880	2240
material 3	2500	10.5480	10.5480	3423	1977

Table 3.2.: Material properties of the modeling setup for sonic measurements in the borehole considering the logging tool, the bore fluid, the casing, and the heterogeneous formation.

Consideration of the  $z$ -velocity components in Figure 3.4(c) and (d) shows slightly different results with less pronounced phase shifts. However, the effect of the tool's geometry on the P-wave bouncing up and down the tool due to the strong impedance contrast between the steel and the surrounding fluid (Käser and Dumbser, 2008) is clearly visible. Furthermore, a systematic analysis of the rotational motion (not shown) could provide additional information and promote the construction and design of rotational borehole sensors.

### 3.4.2. Reservoir-Scale Modeling

Surface seismic data generally provides a large-scale picture of the geological subsurface and the geometrical features of a reservoir. Seismic simulations are used for model validation or survey design. In particular, time-lapse seismic measurements allow for the assessment of changes in the subsurface with time, such as fluid movement or effects of secondary oil recovery. Such data are examined for variations in seismic attributes related to pore-fluid content. Therefore, reservoirs are described by dynamically changing properties and reduced turn-around times for model updates through efficient model building technologies are becoming an increasingly important issue in oil and gas exploration.

The ADER-DG method is capable of using unstructured tetrahedral meshes for the accurate simulation of seismic wave propagation phenomena. Especially for geometrically complex models, such as the SEG/EAGE salt model shown in Figure 3.5(a), the mesh generation process for tetrahedral meshes can be highly automated once the model geometry is defined. The mesh can be aligned to complex shapes of free surface topography, structural interfaces, or faults in order to approximate correctly such structural features. This is particularly important when these features represent sharp material discontinuities that should not be smoothed out by strong gradients. To demonstrate the capability of the methodology we apply our software to a simplified salt model in Figure 3.5(b) that contains the main features, like complex salt body, the major fault, and some sedimentary layers, of the SEG/EAGE model. The problem of the original complete model is that it requires a tedious, manual correction of the geometry definition, as some interfaces and surfaces forming the geological units are intersecting in a non-physical manner. Different sections and parts of our simplified salt model are shown in Figure 3.6 and the according

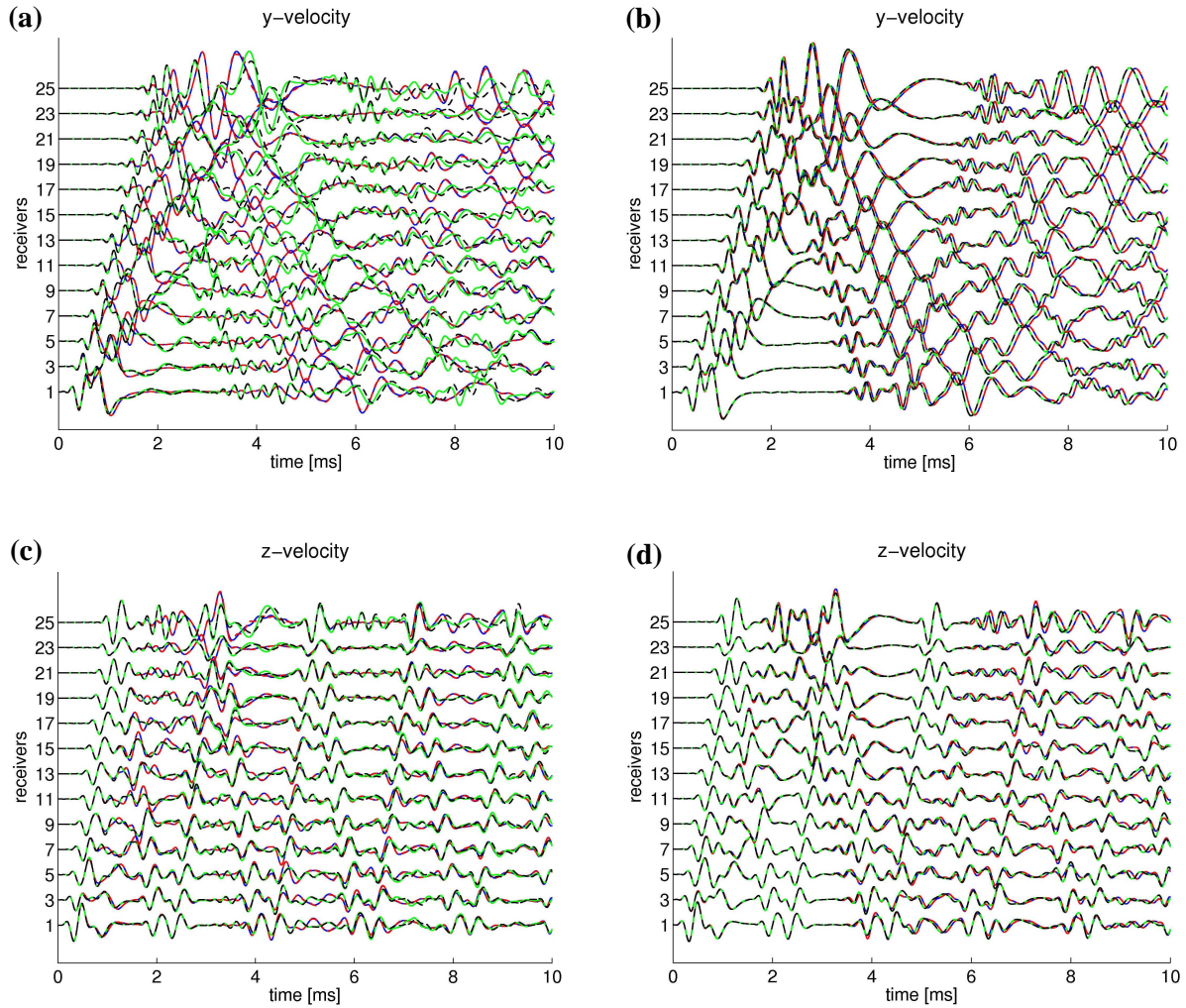


Figure 3.4.: Synthetic wave forms of velocity components for the sonic logging experiment. (a) Damage zone (material gradient) of 2 m radius is assumed. Results are shown for four experiments: small (blue-solid) and large (red-dashed) material contrast with casing, and small (green-solid) and large (black-dashed) material contrast without casing. (b) Same as (a), however, without damage zone. (c), (d) Same as (a), (b) for the z-velocity component instead of the y-component.

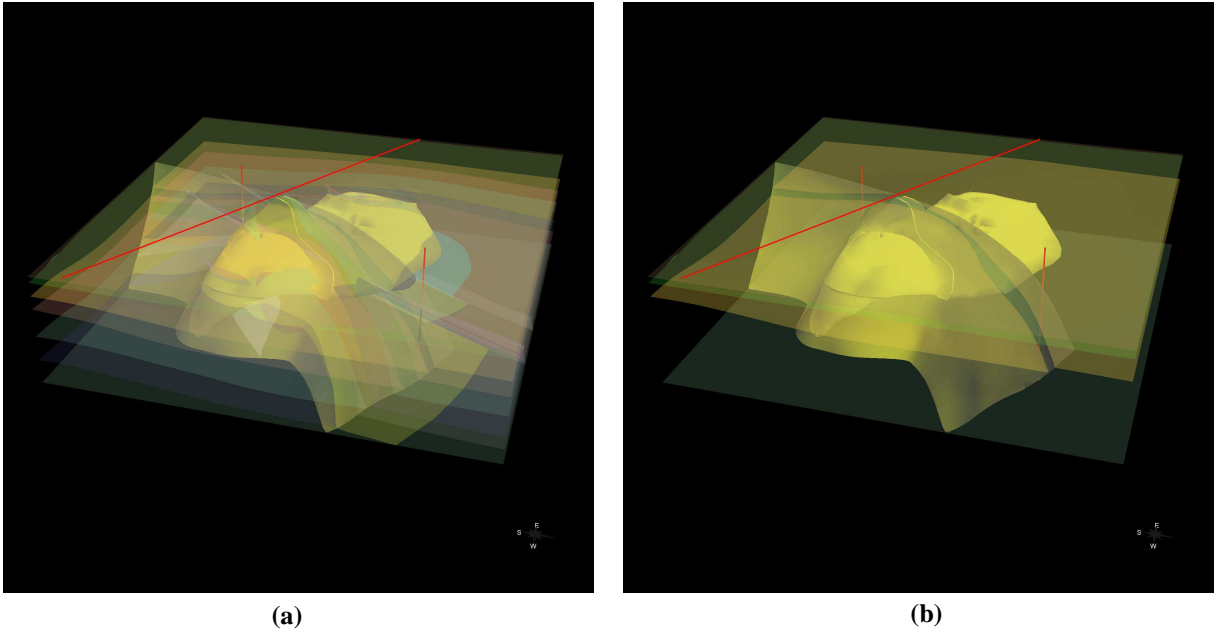


Figure 3.5.: SEG/EAGE salt model. (a) Complete and (b) simplified model including the fundamental features of intersections of layers, faults, and the salt body. The horizontal red line indicates the cross section along A-A', the vertical red lines indicate the two boreholes.

material properties are given in Table 3.3. A 2D cut along the profile A-A' indicated as a red surface line in Figure 3.5 is shown in Figure 3.6(a) together with the notation of the material distribution. In Figure 3.6(b) we display a 3D perspective view of the model, where the water layer and geological units 1b and 2b are removed in order to see the deformation of the fault due to the salt body intrusion. A separate view of the complex 3D geometrical structure of the salt body is shown in Figure 3.6(c). Note that holes in the original definition of the enclosing salt body surface are closed according to the geometry of the intersecting faults. Here, we emphasize that a crucial precondition of the automatic mesh generation process is the exact definition of the model's geometry. Once this is done, the appropriate mesh spacing has to be chosen such that the geometrical features are accounted for with sufficient resolution and that the propagated seismic waves are approximated with the desired accuracy.

It is important to remember that the accuracy of the numerical seismograms depends on three factors: (1) the mesh spacing, (2) the approximation order, and (3) the propagation distance of the waves. A detailed study of the influence of these parameters on the accuracy of synthetic seismograms obtained by the ADER-DG method has been carried out by Käser *et al.* (2008).

An example of the effect of different approximation orders for the SEG/EAGE salt model is shown in Figure 3.7. The seismogram is obtained by using a tetrahedral mesh of  $3.1 \cdot 10^6$  elements of  $\sim 200$  m edge length and is recorded by a receiver inside one of the boreholes indicated as vertical red lines in Figure 3.5. An explosive source producing a Ricker wavelet with dominant frequency of 5 Hz is located in the other well. Using an ADER-DG scheme of second order ( $\mathcal{O}2$ ) in time and space generates a smooth seismogram,

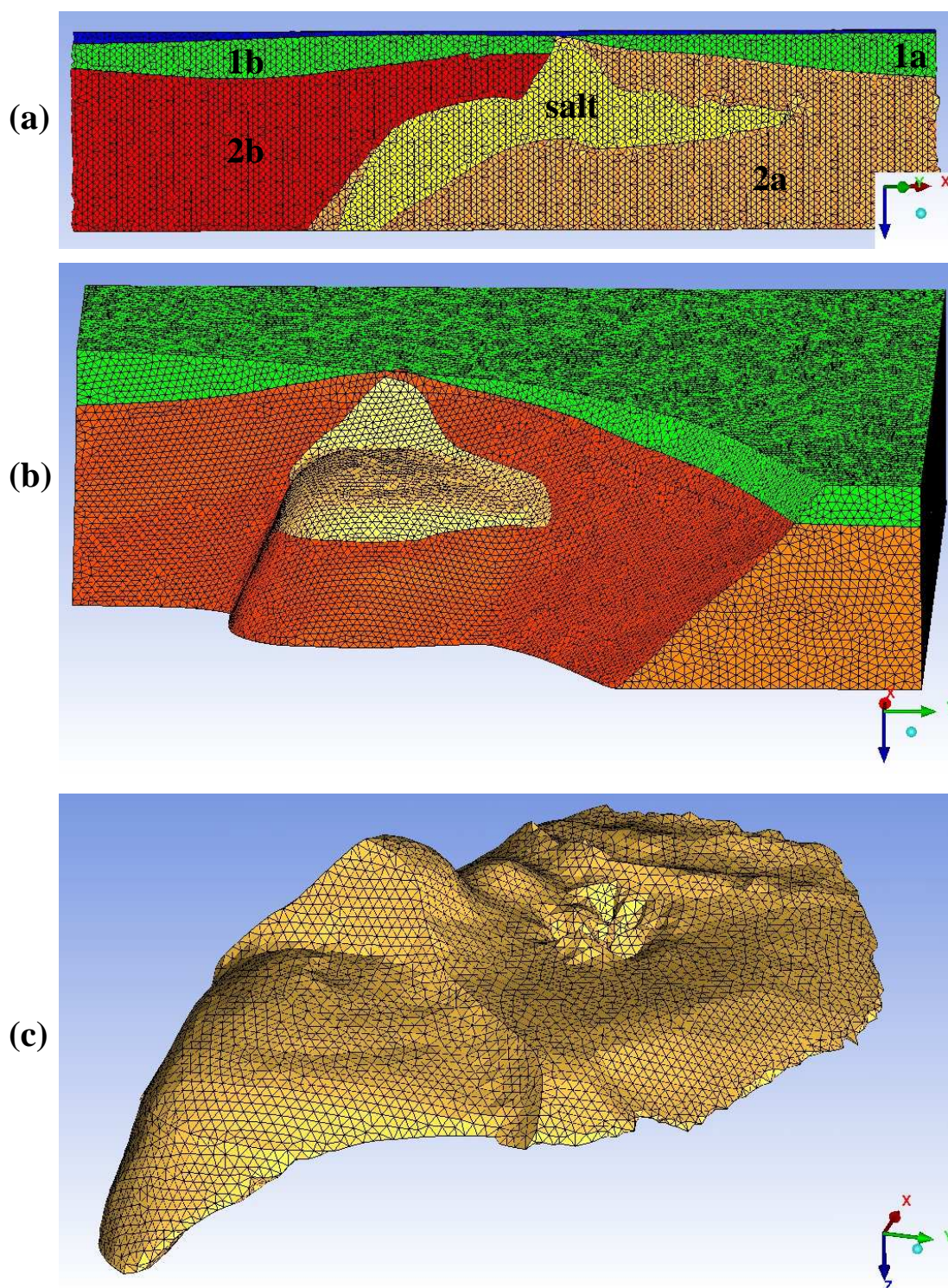


Figure 3.6.: (a) Cut through the tetrahedral mesh produced with ICEM-CFD (ANSYS) along the A-A' profile showing the geometry of the salt body of the SEG/EAGE salt model. (b) 3D perspective of the salt (yellow) exhibiting complex features due to its intersection with a fault. (c) 3D geometry of the discretized salt body.

	$\rho$ [kg/m <sup>3</sup> ]	$\lambda$ [10 <sup>9</sup> Pa]	$\mu$ [10 <sup>9</sup> Pa]	$v_p$ [m/s]	$v_s$ [m/s]
water	1020	2.2950	0.0000	1500	0
layer 1a	2000	4.5067	4.5067	2600	1501
layer 1b	2050	5.0000	5.0000	2705	1562
layer 2a	2500	7.5000	7.5000	3000	1732
layer 2b	2600	9.0000	9.0000	3223	1861
salt	2160	20.8000	14.4570	5094	3103

Table 3.3.: Material properties of the modeling example of the simplified 3D salt model problem.

where much of the amplitude information is essentially lost due to numerical diffusion. Therefore, the problem is under-resolved, but gives a first rough estimate of the solution without producing numerical artifacts. Increasing the order to  $\mathcal{O}3$  or  $\mathcal{O}4$  preserves more amplitude information, while the change between two consecutive orders indicates how close the solution has already converged towards a quasi-analytic solution. The frequency spectra in Figure 3.7 clearly show the extended frequency content of the synthetic signal of higher approximation quality while preventing spurious high-frequency noise.

We finally apply the ADER-DG  $\mathcal{O}4$  scheme to the simplified salt model to produce synthetic raw shots similar to acquired data in surface seismic surveys running a computation on 512 cores. Examples of resulting data sets are shown in Figure 3.8 for two different shot locations recorded along surface receiver lines (a) on cross-section A-A' and (b) connecting the two boreholes. The strong direct water wave is clearly visible in Figure 3.8(a) while effects due to the structural features of the salt body are visible in Figure 3.8(b). Data processing can now be applied as for real data. Besides, the synthetics allow for systematic studies of source signature effects and structural or compositional subsurface properties on the seismic response.

### 3.5. Concluding Remarks

We presented the new Discontinuous Galerkin finite element method for seismic wave propagation modeling applied to relevant problems in oil and gas exploration using HPC-infrastructure. The geometrical flexibility of unstructured tetrahedral meshes combined with the method's high-order approximation properties in space and time, due to a novel time integration scheme for explicit schemes, demonstrates the potential of the proposed simulation technology to produce accurate and reliable synthetic datasets for challenging modeling problems. The applicability of the software using different hardware architectures of modern HPC-infrastructure, its scaling properties and memory usage allow for the solution of large-scale wave propagation problems to support model validation by comparing synthetics with acquired field data. Further technical improvements with respect to run-time and cache optimization are necessary to enhance the method's performance on HPC-facilities, whereas developments covering a broader field of geophysical applications should be motivated by specific needs of the users.

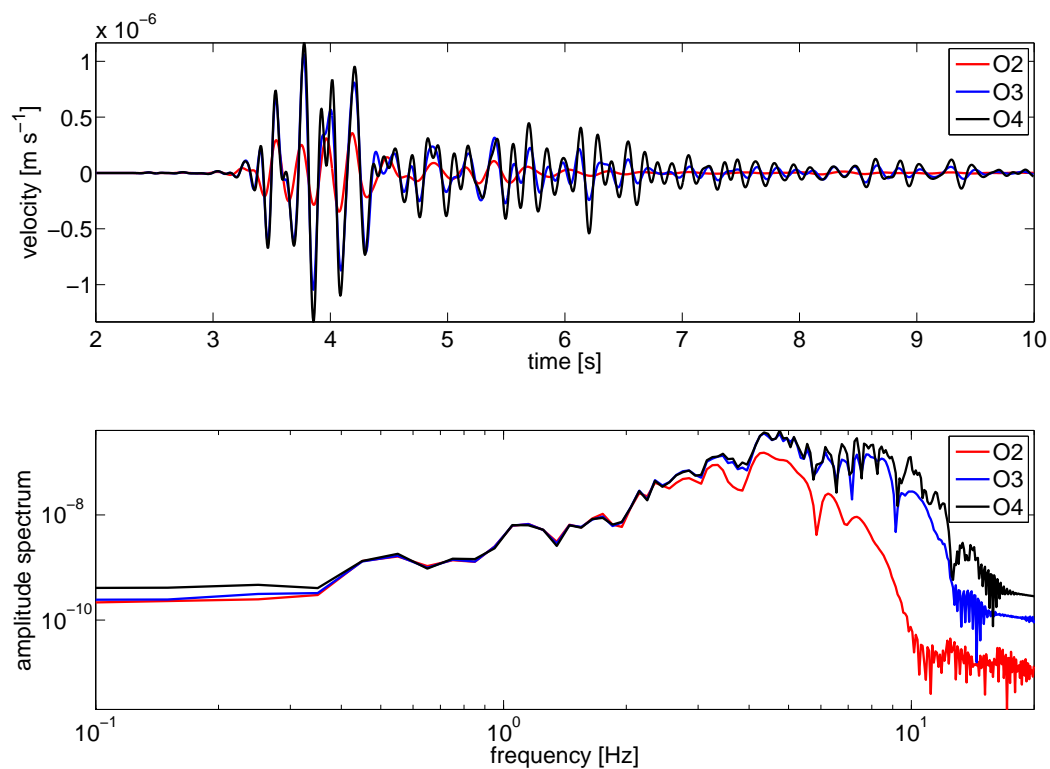


Figure 3.7.: Reduced numerical diffusion and extended frequency content of synthetic seismograms due to higher approximation orders on the same mesh spacing.

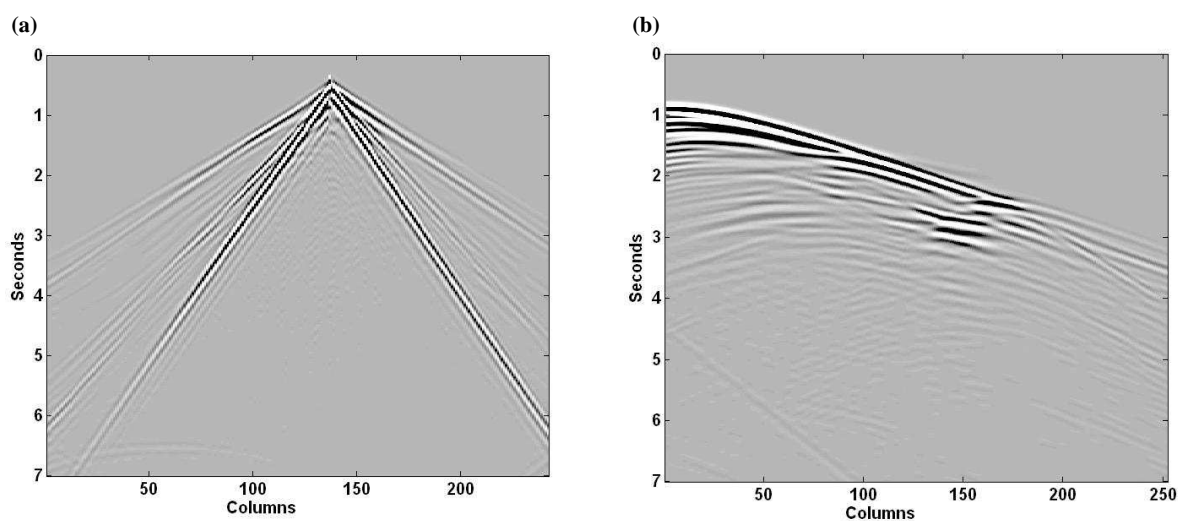


Figure 3.8.: Synthetic raw shots of two surface receiver lines across the salt model. (a) The source position is at the surface close to the center of the receiver line A-A'. (b) The source is inside a borehole with a receiver line connecting the two wells at the surface.



## Chapter 4.

# Regular vs. Irregular Meshing for Complicated Models and Their Effect on Synthetic Seismograms

We present a detailed study on the numerical effects due to staircase approximations of non-planar material interfaces and the importance of mesh alignment to such material boundaries using the Discontinuous Galerkin Finite Element method. Our aim is to define clear rules that have to be adhered to guarantee acceptable synthetic data in seismic forward modeling for the cases where material contrasts occurring along curved interfaces are discretized with regular meshes. To this end, we compare results of structured staircase approximations with reference results obtained by unstructured triangular meshes that can be aligned to non-planar interfaces. We investigate different mesh spacings, wave frequencies, and material contrasts to cover various parameter ranges that allow us to measure their influence on the accuracy of the resulting wave forms. Our results show that acceptable synthetic results strongly depend on the material contrast and we give a quantitative estimate of the required mesh resolution in the sense of numbers of elements per shortest dominant wave length to obtain satisfying seismograms even if the material interfaces are not respected by the mesh. We apply our rules to two different test cases including a multi-layered model and a basin structure, both with non-planar interfaces of small and large material contrasts to confirm the validity of our study. We finally conclude that for moderate material contrasts regular meshing can be beneficial due to its simple mesh generation process and typically superior computational efficiency compared to unstructured meshes, however, the correct frequency- and material-dependent mesh resolution has to be chosen.

### 4.1. Introduction

Recently, the development of seismic forward modeling tools seem to increasingly consider the use of unstructured meshes (Bao *et al.*, 1998; Gao and Zhang, 2006; Stupazzini *et al.*, 2008; Ichimura *et al.*, 2009; Etienne *et al.*, 2009; Wilcox *et al.*, 2010). The main motivation for this discretization approach is the alignment of the mesh to geometrically

---

This chapter presents the work of Christian Pelties, Martin Käser, Cristóbal E. Castro and Verena Herman published in *Geophysical Journal International* (2010) in a slightly modified form.

complex material discontinuities or topographic features. The accurate representation of the real geometry of a physical problem is generally assumed to be important to achieve high-quality simulation results avoiding numerical artifacts due to inappropriate model discretization. However, unstructured meshes typically require more computational memory than regular, structured grids as the connectivity between element vertices has to be stored explicitly. Furthermore, they often are computationally more expensive to obtain a numerical solution. Nevertheless, unstructured meshes tend to become a popular choice for wave propagation applications, as the mesh spacing  $h$  can be changed locally ( $h$ -adaptation) to adjust the element size to the material properties or to improve the resolution of particular areas of interest. Alternatively, a solution can be approximated within each element using polynomials of various degree  $p$  leading to locally increased accuracy ( $p$ -adaptation). In addition, local time stepping might be used (Dumbser *et al.*, 2007) to reduce the computational cost. Unfortunately, these advanced methods can be difficult to implement, maintain, or extend to further functionalities due to the underlying data structures and sophisticated algorithms.

Within the topic of unstructured 3D meshes there is a further distinction, mainly between meshes of hexahedral or tetrahedral elements, as other element types like pyramids or prisms are rarely used. Methods like the Spectral Element Method (SEM) show particular advantages for hexahedral meshes, while their efficient formulation even for 2D triangular meshes seems to be problematic (Pasquetti and Rapetti, 2006; Mercerat *et al.*, 2006). On the other hand, the Discontinuous Galerkin (DG) method is well-suited for tetrahedral or triangular meshes but in general computationally more expensive. In both cases, however, the creation of the computational meshes for geometrically complex domains requires advanced mesh generators, e.g. CUBIT, ANSYS ICEM-CFD, Fluent Gambit, or TetGen. Most of this meshing software is developed and used for engineering problems such as structural mechanics, fluid dynamics, etc. and can handle geometries that typically represent combinations and modifications of simple geometrical shapes. In contrast, many problems in geoscience consists of more complicated structures and geological units with irregular internal material interfaces, non-planar earthquake faults, or complex domain boundaries due to topography. Furthermore, the geometrical information is given as a large data set of discrete points of regular or irregular distributions, which have to be interpolated to obtain surface splines that can then be processed by the mesh generators. The step of building this geometry typically is a time consuming task requiring a large amount of manual interaction. Finally, not all geoscientists, or computational seismologists in particular, have access to the appropriate, often commercial software, which hinders the distribution of codes based on specific mesh generators within the community of seismology or geoscience in general.

On the other hand, methods based on regular, structured grids like Finite-Differences (FD) (e.g. Moczo *et al.*, 2007a; Olsen *et al.*, 2006) helped tremendously to answer many scientific questions in the past and are widely spread in the seismological community. However, the assignment of material properties to nodes located at the interface can be problematic and staircase approximations of material discontinuities usually occur. For internal material interfaces the accuracy often relies on sufficiently fine grid spacing and special treatments to avoid spurious diffractions (Zahradnik *et al.*, 1993; Collino *et al.*, 1997). The misalignment of the regular grid to material discontinuities leads to first-order

errors proportional to the grid spacing or time step that are insensitive to the approximation order of the numerical scheme (Gustafsson and Wahlund, 2004; Symes *et al.*, 2008). Therefore, work has been done to represent such interfaces through an appropriate usage of effective material using harmonic and arithmetic averaging of elastic moduli and densities (e.g. Graves, 1996; Moczo *et al.*, 2002). Zhang and LeVeque (1997) developed a second-order accurate method for the acoustic wave equations in heterogeneous media using high resolution multi-dimensional flux-limiters on a Cartesian grid. Near the material interface special formulas are developed using the immersed interface method that incorporate the jump conditions and give pointwise second order accuracy even when the interface is not aligned with the grid. This approach was then extended to fourth-order accuracy and for elastic waves (Zhang and Symes, 1998). A major disadvantage of regular grid methods occurs when dealing with complex free-surface topography. It is well known that standard FD schemes require a high grid resolution at free-surface boundaries to avoid numerical artifacts, in particular, if non-planar free-surface topography has to be included (Robertsson, 1996; Bohlen and Saenger, 2006). Moczo *et al.* (2007b) summarize and analyse existing FD schemes for this topic in detail and suggest an alternative approach to model free-surface topography. However, standard FD schemes rely on dense meshes which could result in an enormous computational effort. An interesting estimation of the computational requirements needed for a large-scale FD simulation is given by Bao *et al.* (1998). Nevertheless, the use of regular grids allows in general for highly efficient codes both in terms of memory and computational cost.

In this paper we analyse quantitatively numerical errors of synthetic seismograms due to staircase approximations of material discontinuities using the DG method, as its implementation on regular meshes is computationally also much more efficient. To this end, we focus on the systematic dependence of the errors on mesh spacing, material contrast, and frequency content of the seismic signal. To our knowledge only few quantitative studies exist for this topic and mainly consider the FD approach (e.g. van Vossen *et al.*, 2002; Bohlen and Saenger, 2006). There, FD schemes are investigated by modeling free-surface conditions and solid-fluid contrasts using variable grid spacings and different angles between the orientation of the grid and the interface. However, they perform their studies for material properties typically occurring in geosciences but do not focus explicitly on error dependencies on the wave speed ratio. In our study, we simulate the reflection and transmission of a 2D plane wave at a semi-circular interface between two materials and also investigate the effects at a non-planar free-surface boundary condition using regular, quadrilateral meshes. The reference solution for all tests is produced with the same, well-tested high-order DG method on unstructured triangular meshes to fully account for the geometrical features of the test cases. This way, differences due to the usage of different numerical methods are excluded. Hence, we can compare synthetic seismograms whose misfits can only originate from the different discretization approaches. Our goal is to define proper discretization rules that should be considered in forward modeling of seismic wave propagation in order to guarantee a desired accuracy. Finally, we show that these rules also hold for more realistic applications with complicated geometrical properties and material distributions typically encountered in layered or sedimentary basin environments.

The paper is structured as follows: Section 4.2 defines the model setup and studies the results of the different staircase discretization approaches. We analyse in detail the errors of the synthetic seismograms and their spatial distribution to set up discretization rules which should help modelers to choose a sufficient geometry sampling. In a second step, we verify these rules in Section 4.3 with a more complicated layered model with two arbitrary shaped interfaces. Finally, we apply and test our rules in a realistic scenario of a basin structure in Section 4.4 and finally draw our conclusions in Section 4.5.

## 4.2. Importance of Interface Approximation

To quantify the dependency of the numerical errors on the approximation quality of the discretization, the material contrast, and the frequency content of the seismic waves, we set up a test case which allows us to perform a systematic analysis by the variation of the respective parameters. This will then lead to the definition of some fundamental rules concerning the discretization of complex geometries with regular meshes and the importance of the interface approximation by mesh alignment.

### 4.2.1. Model Setup

Similar to previous work (Kawase, 1988; Ohminato and Chouet, 1997) we simulate the incidence of a plane P-wave with a Ricker-type source time function onto a semi-circular material interface separating a basin-like structure from a homogeneous half-space (see Fig. 4.1). Material 1 located in the half-circle of radius  $r = 100$  m is surrounded by material 2 of higher wave velocities. In addition to five different material contrasts of elastic media, we also consider two special cases, where the material 1 in the basin is an acoustic fluid, or where the material interface represents a free-surface boundary such that material 1 vanishes. We will focus on the computational domain  $(x, z) \in \Omega = [-400, 400] \times [-400, 0]$  m  $\in \mathbb{R}^2$  with the top boundary ( $z = 0$  m) being a free surface. In fact, the other boundaries of the model are extended sufficiently to avoid any interference of possible reflections from non-perfectly absorbing boundaries with the waves of interest that are reflected, transmitted, or converted at the material interface or the free surface. Tests, which are not shown here, indicated that, in principle, similar results are obtained for plane S-wave incidence or waves from single-force sources generating P- and S-waves as well as for different interface geometries, e.g. a notch (Godinho *et al.*, 2009). The dots in Fig. 4.1 denote the locations of  $21 \times 21$  receivers allowing for a dense sampling of the wave field to obtain an overview of the spatial error distribution.

In Fig. 4.2 we show the two different discretization approaches used. On the left side a regular, structured grid with a mesh spacing of  $h = 20$  m is sketched. In our study we assign constant material properties within each element determined by the location of the element's geometrically barycenter. With the displayed coarse resolution of only a fifth of the semi-circle's radius the discretized shape of the material interface hardly represents the true geometry. On the right side of Fig. 4.2 we show an unstructured, triangular mesh with an average triangular edge length of  $h = 10$  m. This discretization is used to produce a reference solution for the problem and provides a sufficiently accurate discretization, as

further mesh refinement to  $h = 5$  m generates quasi-identical seismograms. Therefore, we also remark that the unstructured triangular mesh with its piecewise linear edge-alignment of  $h = 10$  m represents the material interface sufficiently accurate.

For our tests concerning the sensitivity of numerical seismograms to the discretization of complex geometry, we use a series of regular square-shaped meshes with  $h = 20$  m,  $h = 10$  m, and  $h = 5$  m providing an improved discretization of the curved material interface by an increasingly fine staircase approximation. Furthermore, we vary the material contrast to investigate its importance with respect to the discretization approach. The material contrast between two materials 1 and 2 is given through the ratio of the S-wave speeds  $v_{S,1}/v_{S,2}$ , with  $v_{S,1} \leq v_{S,2}$ . In this way, small numbers represent strong material contrasts. Table 4.1 gives an overview of the applied material contrasts and wavelengths. Finally, we use plane, Ricker-type P-waves of different dominant frequency contents,  $f_{15} = 15$  Hz,  $f_{20} = 20$  Hz, and  $f_{25} = 25$  Hz to analyse the dependence of the discretization effects on the seismic wavelengths. We mention, that the Ricker wavelet of a dominant frequency  $f$  contains significant energy up to a maximum frequency of around  $2.5f$ .

The used simulation code is based on a DG method and is well-tested and verified against analytical solutions and other numerical schemes (Dumbser and Käser, 2006; Käser *et al.*, 2008). Its accuracy and applicability to strong material heterogeneities was also confirmed in previous work (Chaljub *et al.*, 2010; Castro *et al.*, 2010). Using the same numerical solver for structured and unstructured meshes ensures that differences in the seismograms originate only from diverse geometry representations and not from numerical biases like diffusion, dispersion, under-resolution, or different ways of incorporating material properties. We remark, that all simulations are performed with order 7 in space and time and use enough elements per wavelength to resolve the wave field sufficiently accurate. This is confirmed by running the simulations of highest frequency content and coarsest discretization with a decreased order of accuracy, which basically does not change the resulting seismograms and therefore proves numerical convergence of the solution. The remaining small differences are much smaller than the effects obtained by varying the parameters of our accuracy analysis.

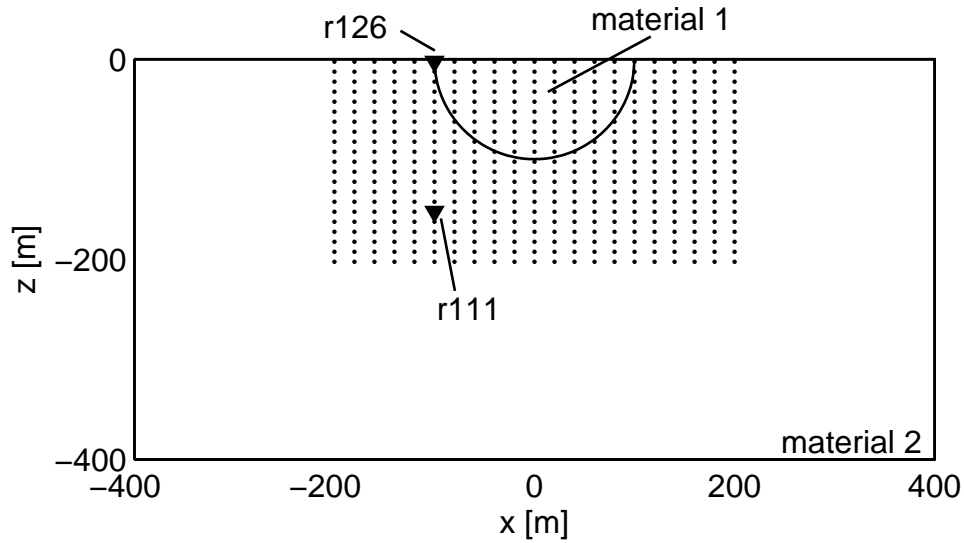


Figure 4.1.: Model setup of the accuracy study with a basin-like structure (material 1) in a homogeneous half-space (material 2). We show a zoomed section of the area of the material interface with receiver locations denoted by dots. Seismograms at positions of highlighted geophones (downward-pointing triangle) are discussed in detail in Section 4.2.2.

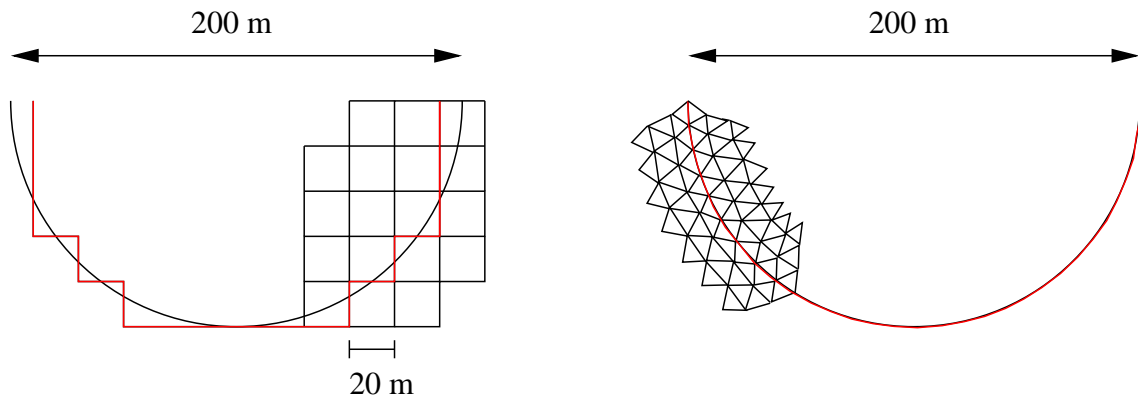


Figure 4.2.: Sketch of the two different discretization approaches. Material properties for the DG method are set element-wise determined by the geometrically barycenter of each element. Hence, the discrete material interface (red line) is dislocated from the exact position (black semi-circle) and depends on the mesh. Left: an example of a regular mesh with 20 m spacing is shown which is not able to represent the interface properly leading to a coarse and jagged approximation. Right: an example of a triangular mesh with 10 m spacing (triangular edge lengths) used to compute the reference solution. In this case, the shape of semi-circle is approximated with piecewise linear edges of triangular elements.

Table 4.1.: Material properties for the seven test cases with different contrasts across the interface. Furthermore, the dimensionless values of the shortest wavelength per mesh spacing  $\lambda_S/h$  are given for the dominant frequencies  $f$ . Please, note that a P wave represents the shortest wavelength in the Solid-Fluid test case.

test case	$\rho$ [kg/m <sup>3</sup> ]	$v_P$ [m/s]	$v_S$ [m/s]	$\lambda_s/h$ for f25			$\lambda_s/h$ for f20			$\lambda_s/h$ for f15		
				h20	h10	h5	h20	h10	h5	h20	h10	h5
<i>Solid-Solid 1:</i>												
material 1	1000	1732	1000	2	4	8	2.5	5	10	3.3	6.7	13.3
material 2	1299	2249	1299	2.6	5.2	10.4	3.2	6.5	13	4.3	8.7	17.3
contrast		0.77	0.77									
<i>Solid-Solid 2:</i>												
material 1	1000	1732	1000	2	4	8	2.5	5	10	3.3	6.7	13.3
material 2	1538	2665	1538	3.1	6.2	12.3	3.8	7.7	15.4	5.1	10.2	20.5
contrast		0.65	0.65									
<i>Solid-Solid 3:</i>												
material 1	1000	1732	1000	2	4	8	2.5	5	10	3.3	6.7	13.3
material 2	2000	3464	2000	4	8	16	5	10	20	6.7	13.3	26.7
contrast		0.5	0.5									
<i>Solid-Solid 4:</i>												
material 1	1000	1732	1000	2	4	8	2.5	5	10	3.3	6.7	13.3
material 2	2500	4503	2600	5.2	10.4	20.8	6.5	13	26	8.7	17.3	34.7
contrast		0.38	0.38									
<i>Solid-Solid 5:</i>												
material 1	1000	1732	1000	2	4	8	2.5	5	10	3.3	6.7	13.3
material 2	5000	8660	5000	10	20	40	12.5	25	50	16.7	33.3	66.7
contrast		0.2	0.2									
<i>Solid-Free Surface:</i>												
material 1	-	-	-	-	-	-	-	-	-	-	-	-
material 2	2000	3464	2000	4	8	16	5	10	20	6.7	13.3	26.7
contrast		-	-									
<i>Solid-Fluid:</i>												
material 1	1020	1500	0	3	6	12	3.8	7.5	15	5	10	20
material 2	2000	3464	2000	4	8	16	5	10	20	6.7	13.3	26.7
contrast		0.43	-									

### 4.2.2. Accuracy Analysis

In the following we analyse the results of the 63 test cases obtained by 7 different material contrasts, 3 mesh spacings and 3 frequencies. First, we study the spatial error distribution to identify areas of particularly high errors. Then we investigate and display the misfits of selected seismograms to define some basic rules. These rules should guarantee a desired level of accuracy for curved interface approximations, that have to be obeyed when using structured meshes.

#### Spatial Error Distribution

We compare the quality of the obtained seismograms at all 441 receivers indicated in Fig. 4.1. To measure the misfit between the simulated test seismogram  $S_{h,i}(t)$  and the reference solutions  $S_{\text{ref},i}(t)$  we use the root mean square (RMS) error

$$E_i = \sqrt{\frac{\int |S_{h,i}(t) - S_{\text{ref},i}(t)|^2 dt}{\int |S_{\text{ref},i}(t)|^2 dt}}, \quad (4.1)$$

where  $i$  is the index of the receiver,  $h$  the mesh spacing of the numerical computation, and  $t$  is time. We emphasize that the RMS error is not always suitable to compare seismograms quantitatively. Instead, time-frequency (TF) misfit criteria as suggested by Kristeková *et al.* (2006) and Kristeková *et al.* (2009) represent a more appropriate approach for the comparison of two signals. The main advantage of the TF-misfit is to obtain separate information about phase and envelope errors. We also determined the envelope and phase misfits individually, however, it turned out that the combined analysis of these envelope and phase misfits at each receiver gives at least a similar pattern as the RMS error. Even though we, in general, strongly recommend the use of the TF-misfit analysis we prefer the single-valued RMS error in this case to provide an overview of the spatial error distribution without splitting all our results considering envelope and phase misfits separately. Furthermore, the RMS error typically tends to overestimate the errors compared to separate envelope and phase misfits and therefore serves as an upper limit estimation.

To present the errors we assign a colored pixel to each receiver depending on the single valued RMS misfit of its seismograms distinguishing horizontal and vertical components.

In Figs 4.3-4.9 we show the spatial error maps representing the single valued RMS misfit  $E_i$  between reference solutions and seismograms obtained with the structured grid. Each figure belongs to one material contrast and contains the results of the three dominant frequencies f15, f20, and f25 (ordered from left to right) obtained from the three refined mesh spacings  $h = 20, 10, 5$  m (ordered from top to bottom). For each frequency and mesh size we display the horizontal and vertical velocity components. For better visualization and comparison the colorbars are normalized ranging between 0 and 1 for the minor material contrasts Solid-Solid 1 (Fig. 4.3) to Solid-Solid 3 (Fig. 4.5) and between 0 and 2 for the stronger contrasts Solid-Solid 4 (Fig. 4.6) to Solid-Fluid (Fig. 4.9) where the errors are larger.

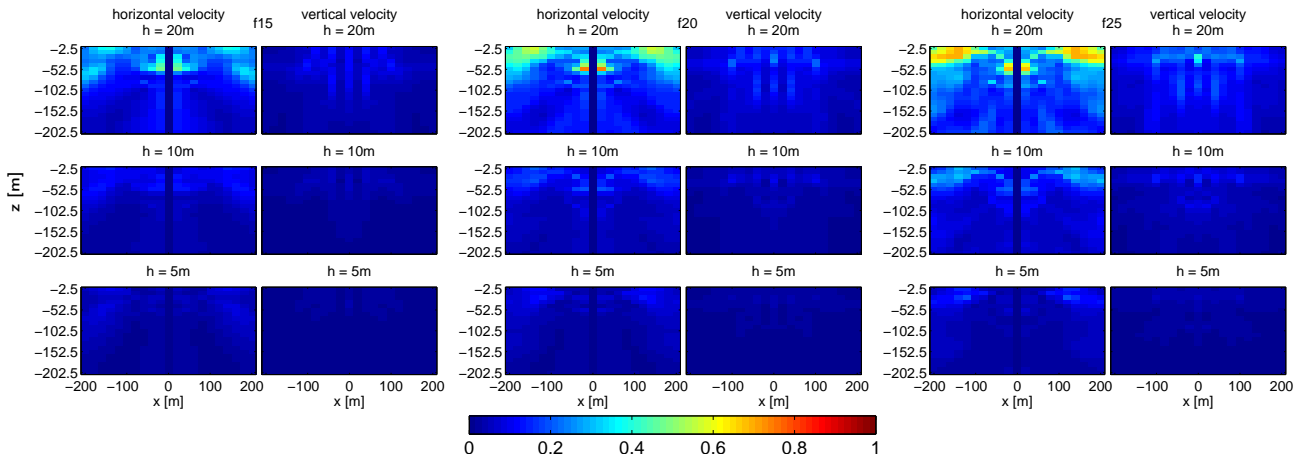


Figure 4.3.: Error maps of the RMS error  $E$  for the test case Solid-Solid 1 with the material contrast 0.77.

A first and obvious observation is that the misfit of the horizontal velocity components in the center of the model ( $x = 0$  m) is always zero, as no energy appears on this component caused by the plane vertical P-wave incident from below. However, higher error levels appear, in general, for the horizontal component. This is also due to the fact that all energy in the system is primarily in the vertical component and only by reflections, refractions, and transmissions energy is transferred into the horizontal component. Therefore, the horizontal component seems to be especially sensitive to the geometry approximations of the semi-circular interface. A further observation is the higher error level close to the material interface, at the free-surface, and at two areas leading away from the semi-circular basin at approximately 30 degrees downward. The shape of the semi-circle is easily identifiable by warmer colors for the stronger material contrasts. Besides higher errors occur at the inside of the semi-circle close to the material contact. Furthermore, a general increase of the error level with increasing mesh spacing, higher frequency content, and stronger material contrast is visible.

Particularly high errors appear in the case of the Solid-Free Surface (Fig. 4.8) and Solid-Fluid (Fig. 4.9) contrasts where the staircase approximation of the curved interface obviously creates large misfits compared to the reference solution obtained with the rather smooth approximation via aligned triangular edges. In these two cases even for the finest mesh spacing  $h = 5$  m and lowest frequency f15 the horizontal component already shows an error level clearly above  $E_i = 0.5$ . However, for the Solid-Solid material interfaces in Figs 4.3-4.7 the finest mesh spacing  $h = 5$  m seems to work surprisingly well.

Based on this investigation of the spatial error distribution we can now focus on the seismogram misfits and the effects of the staircase approximation of a curved interface on the seismic signature in more detail.

### Seismogram Misfits

After the analysis of the overall distribution of RMS errors, we study the seismic wave forms at two receivers in different areas of the computational domain. To this end,

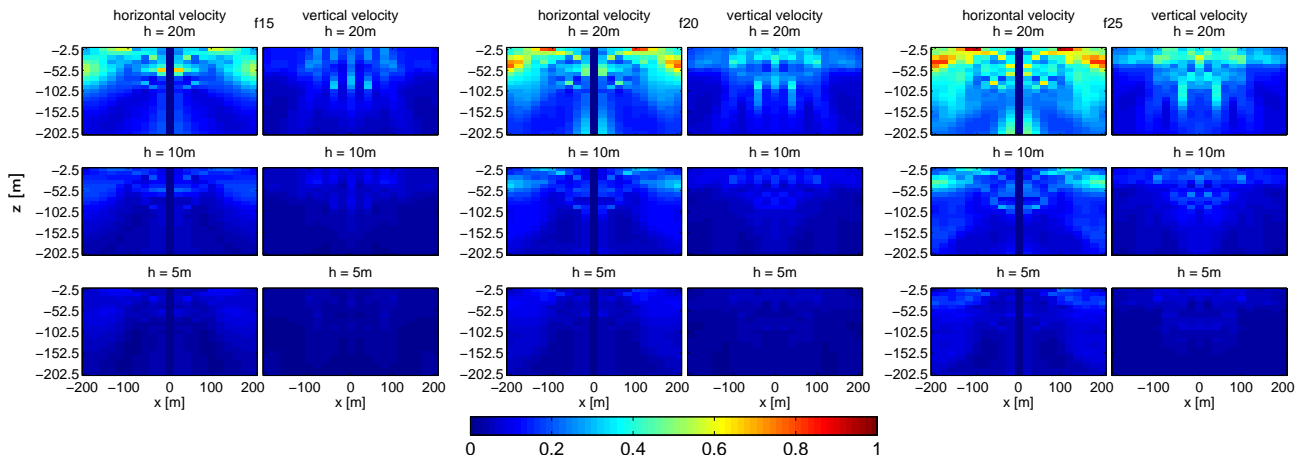


Figure 4.4.: Error maps of the RMS error  $E$  for the test case Solid-Solid 2 with the material contrast 0.65.

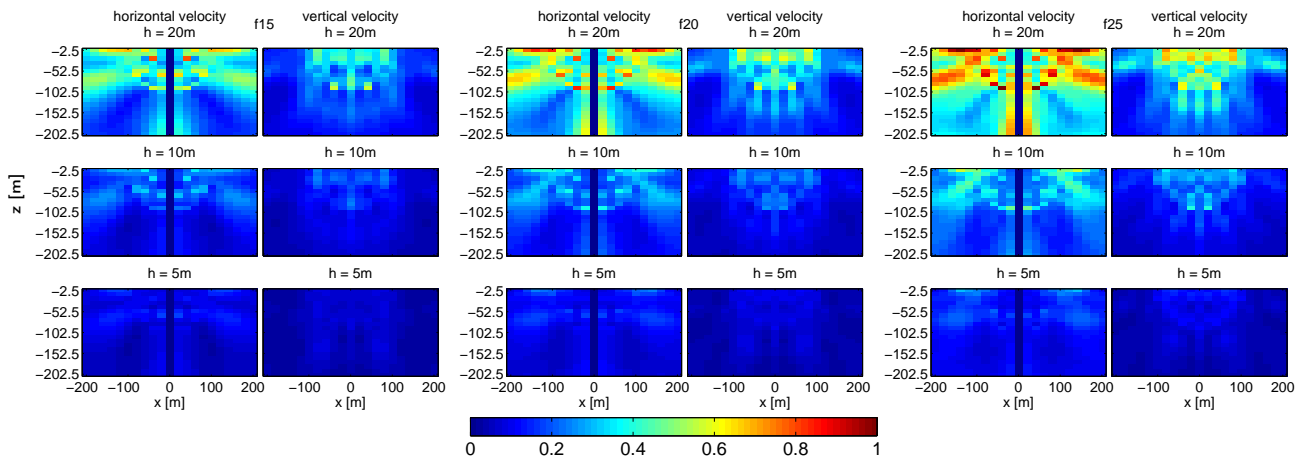


Figure 4.5.: Error maps of the RMS error  $E$  for the test case Solid-Solid 3 with the material contrast 0.5.

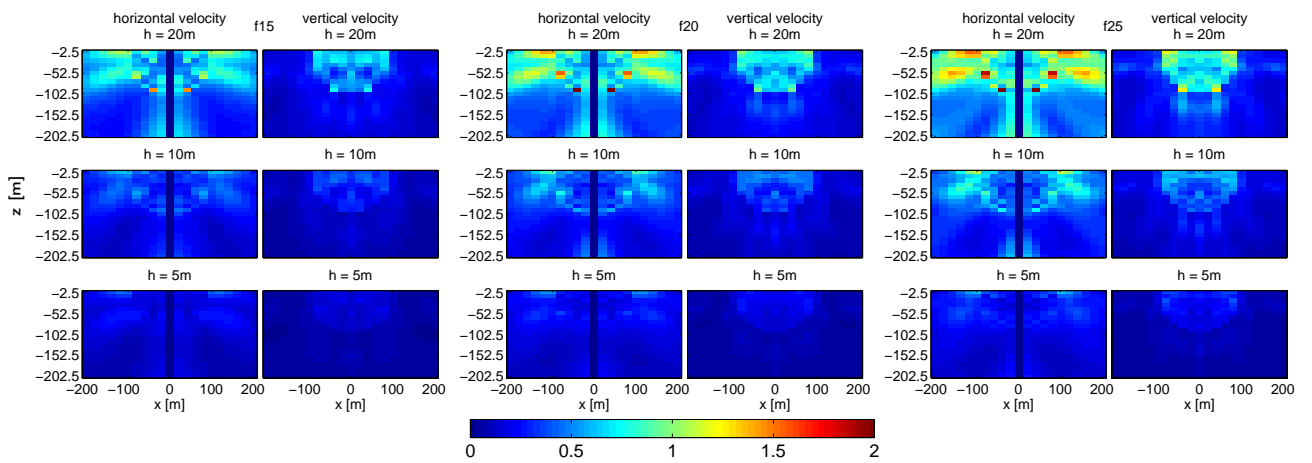


Figure 4.6.: Error maps of the RMS error  $E$  for the test case Solid-Solid 4 with the material contrast 0.38.

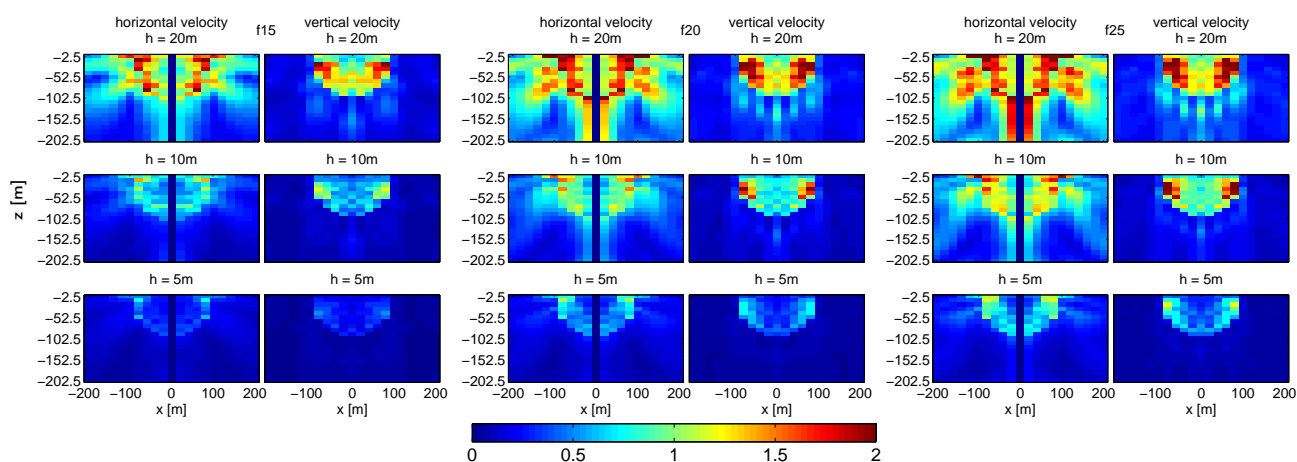


Figure 4.7.: Error maps of the RMS error  $E$  for the test case Solid-Solid 5 with the material contrast 0.2.

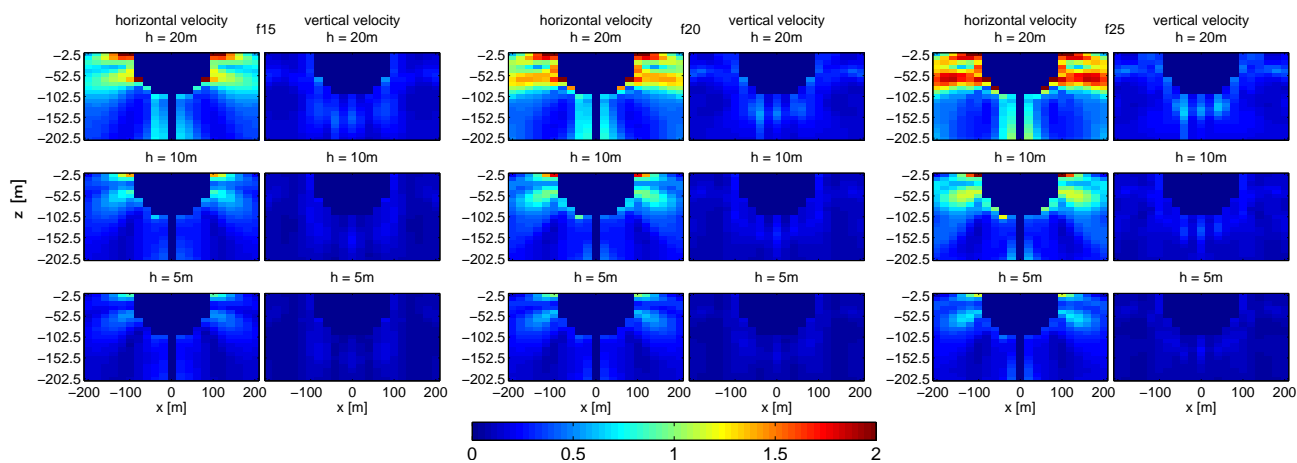


Figure 4.8.: Error maps of the RMS error  $E$  for the test case Solid-Free Surface.

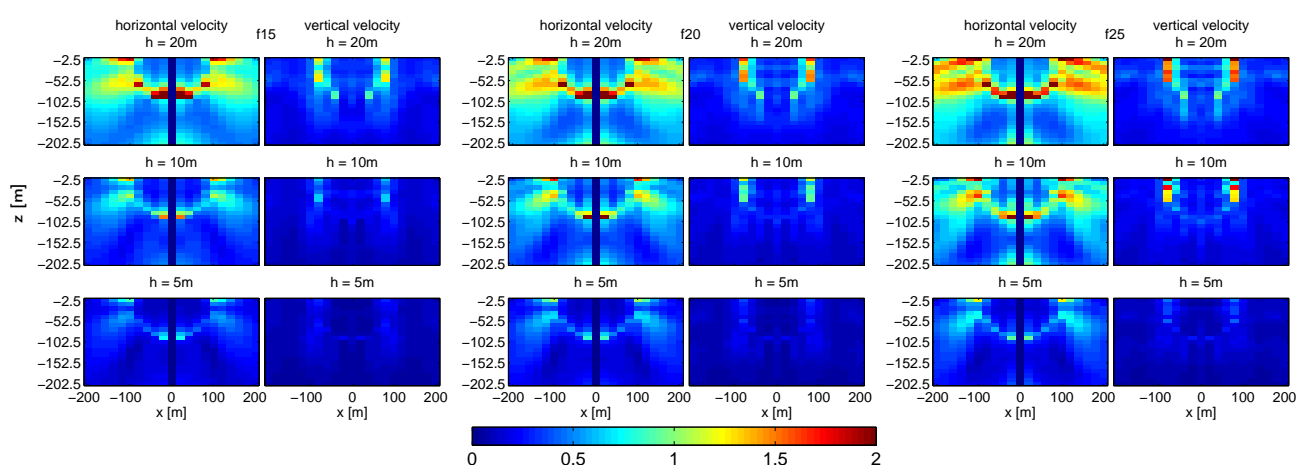


Figure 4.9.: Error maps of the RMS error  $E$  for the test case Solid-Fluid.

we show the variation of the seismograms for the test cases Solid-Solid 1 (Fig. 4.10), Solid-Solid 3 (Fig. 4.11), Solid-Free Surface (Fig. 4.12), and Solid-Fluid (Fig. 4.13) with respect to their dependence on the mesh spacing (different colors) and frequency (ordered from top to bottom) for both horizontal (left) and vertical (right) components. In each figure we display the results obtained for receivers r111 and r126 at the locations indicated by the downward-pointing triangles in Figure 4.1. While receiver r111 ( $x, z) = (-100.0, -152.5)$  m lies in an area of a generally low RMS error, receiver r126 ( $x, z) = (-100.0, -2.5)$  m has a crucial position close to the free-surface boundary at the top of the computational domain and directly at the material interface. If we compare the behavior of the seismogram misfit in Figs 4.10-4.13 with each other, the growing misfits with increasing material contrast is clearly observable again. The seismograms of the test case Solid-Solid 1 (Fig. 4.10) are examples of an remarkably good fit, which is due to the small material contrast. Only at the crucial position of r126 for a coarse mesh spacing of  $h = 20$  m we obtain larger amplitude errors and phase shifts for the horizontal velocity component. The seismograms of receiver r126 for the test case Solid-Solid 3 (Fig. 4.11) show nicely how the error decreases with decreasing mesh spacing. However, we can observe only a small decrease of the misfit at lower frequencies. In contrast, receiver r111 seems to be much less affected. As expected, the quality of seismograms at receiver r126 depends strongly on the combination of the three different simulation parameters due to its worst case position identified in Section 4.2.2.

Furthermore, the seismograms of the test cases Solid-Free Surface (Fig. 4.12) and Solid-Fluid (Fig. 4.13) clearly demonstrate that the wave forms are strongly affected by the staircase approximation of the semi-circular interface. While the misfits at receiver r111 again are much smaller and decrease even more with reduced mesh spacing and frequency, the seismograms at receiver r126, especially the horizontal components, are not acceptable even for the finest mesh h5 and lowest frequency f15.

### 4.2.3. Discretization Rules

To facilitate the definition of useful discretization rules that have to be considered when approximating curved material interfaces we introduce the total error

$$E_{\text{tot}} = \frac{1}{N} \sum_i \left( E_{i,\text{horizontal}} + E_{i,\text{vertical}} \right) \quad (4.2)$$

over all receivers  $i$  that occur in an error map of Figs 4.3-4.9, where  $N$  is the number of receivers. Note, that  $N$  changes for the test case Solid-Free Surface depending on how many receivers are still below the free-surface boundary, while  $N = 441$  for all other test cases. The error  $E_{\text{tot}}$  allows us to measure the overall seismogram misfit of a simulation depending on different mesh spacings, frequencies, and material contrasts. A threshold of the error  $E_{\text{tot}}$  is shown as a dashed red line in all plots of Figs 4.14-4.16. The results of the systematic error analysis are shown in Figs. 4.14-4.15 on the left displaying the behavior of the error  $E_{\text{tot}}$  with respect to mesh refinement for each of the seven different material contrasts. The three lines of different symbols represent the frequencies. Clearly, the errors are consistently smaller for lower frequencies and decrease almost linearly with

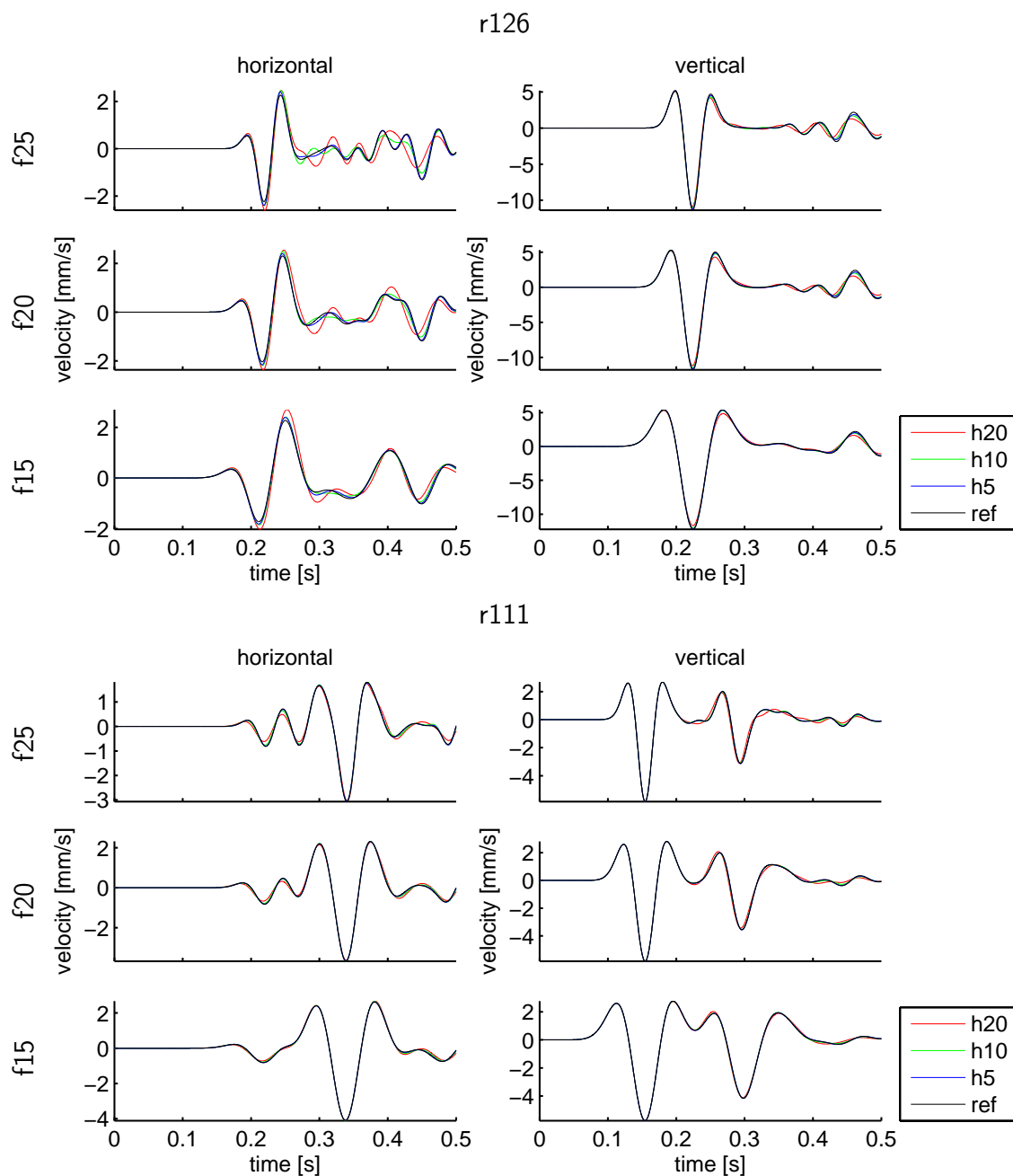


Figure 4.10.: Example seismograms of the accuracy study test case Solid-Solid 1 with the material contrast 0.77. Shown are the horizontal and vertical velocity components of r126 (top) and r111 (bottom).

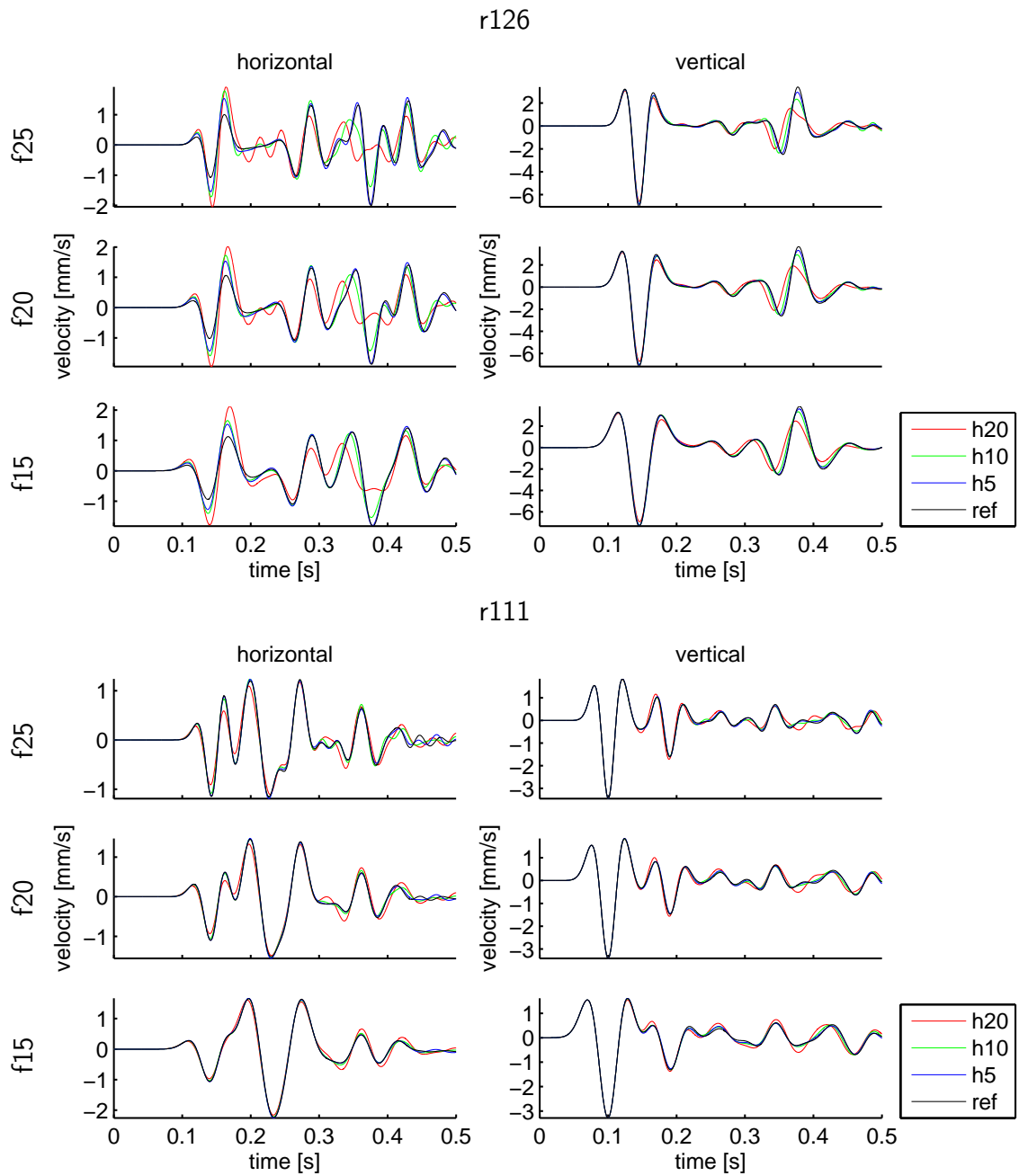


Figure 4.11.: Example seismograms of the accuracy study test case Solid-Solid 3 with the material contrast 0.5. Shown are the horizontal and vertical velocity components of r126 (top) and r111 (bottom).

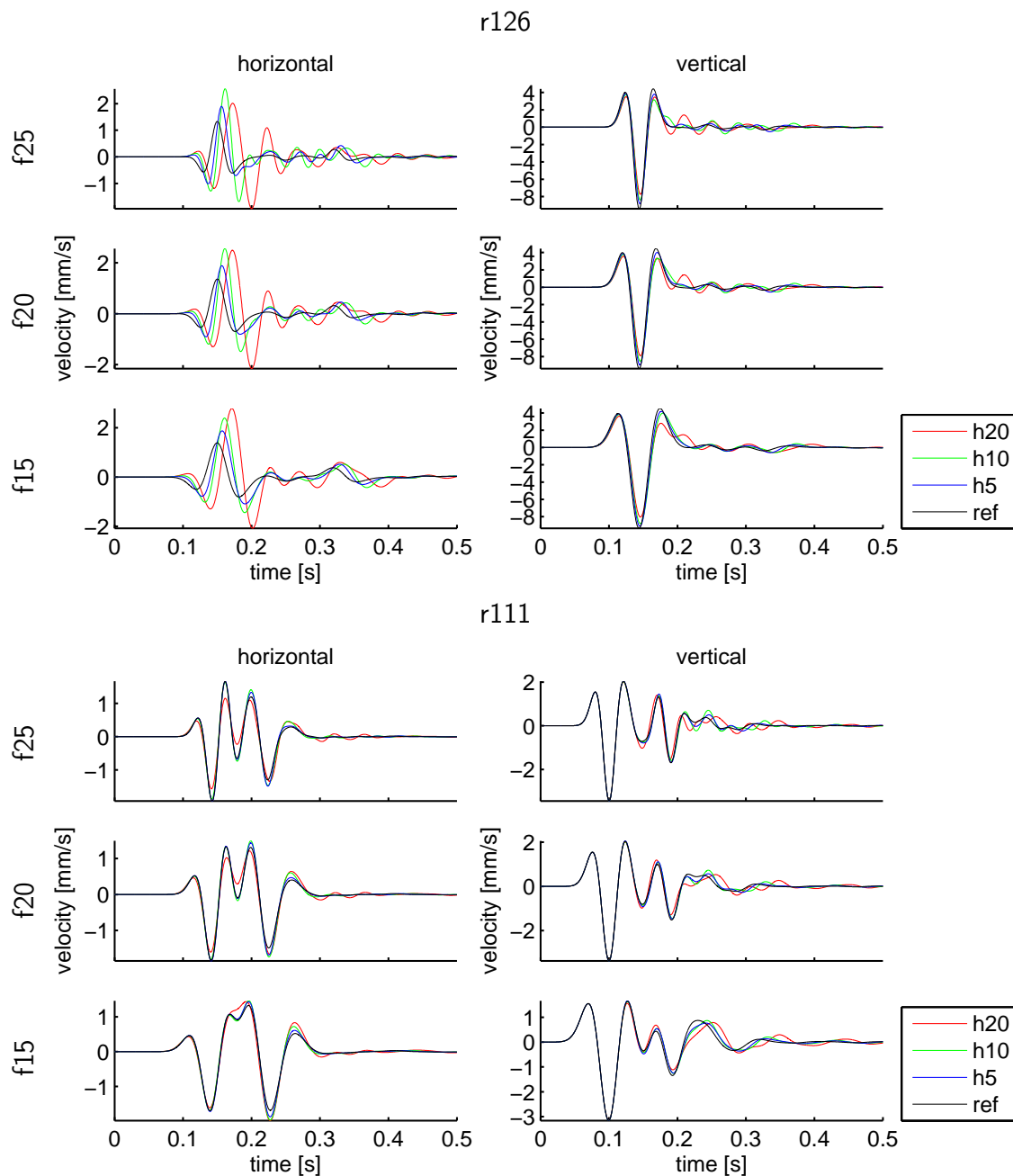


Figure 4.12.: Example seismograms of the accuracy study test case Solid-Free Surface. Shown are the horizontal and vertical velocity components of r126 (top) and r111 (bottom).

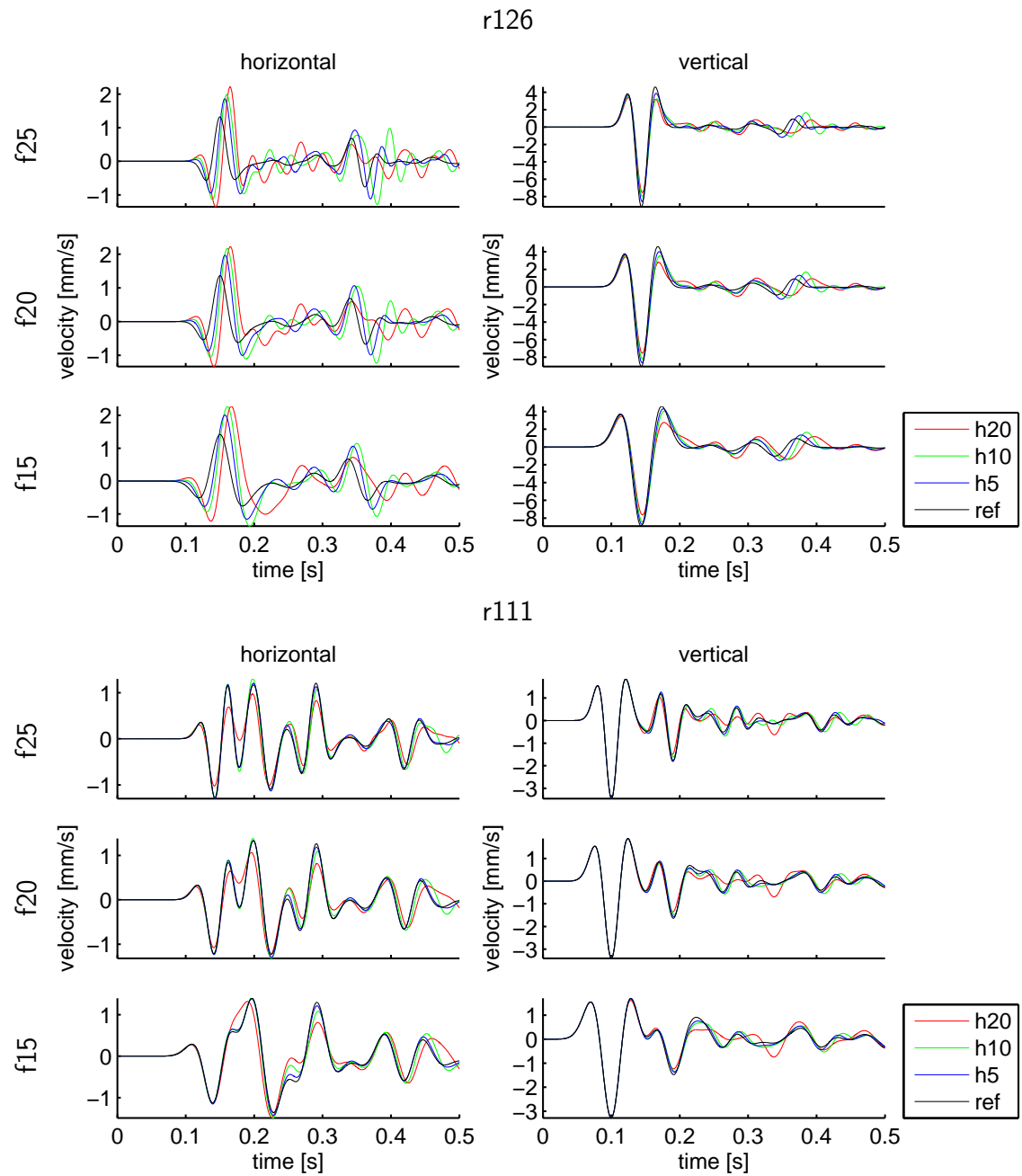


Figure 4.13.: Example seismograms of the accuracy study test case Solid-Fluid. Shown are the horizontal and vertical velocity components of r126 (top) and r111 (bottom).

mesh refinement for all seven test cases. Therefore, our DG approach confirms the first-order error behaviour due to the simple staircase approximation as predicted by studies on the immersed interface method (Zhang and LeVeque, 1997; Zhang and Symes, 1998) even though the approximation of the solution using our DG scheme is of order 7 in space and time. We mention that the basic idea in immersed interface methods is to take into account the jump conditions for the discontinuous solution or its derivatives at an interface and to find linear combinations of these discontinuous values that give more accurate numerical approximations at or near the interface.

Presenting the results in a different way in Figs. 4.14-4.15 on the right, where the error is plotted against frequency, shows that systematically finer meshes provide smaller errors that increase with higher frequency content. In a third presentation of our results in Fig. 4.16 we show the behavior of the error for all seven material contrasts (different line symbols) in one plot. In the top row the frequency is fixed in each plot and the error decreases with decreasing mesh spacing  $h$ . In the bottom row the mesh spacing is fixed and the error behavior depending on frequency is shown. Obviously, the errors are generally smaller for smaller material contrasts, however, the test case Solid-Fluid seems to be even more sensitive to the staircase approximation than the Solid-Free Surface. We point out that it is important to consider interface waves such as Rayleigh waves at the free surface and Scholte waves at an elastic-acoustic interface when signals are recorded directly at or in the vicinity of the interface. Even though such interface waves propagate slower than the S wave inside the elastic material their phase velocities are usually close to the S wave velocity. Therefore the suggested mesh spacing of the following discretization rules would have to be adjusted by using a correspondingly smaller mesh spacing. Furthermore, the velocities of the interface waves show significant frequency-dependence (dispersion) and their energy content compared to the body waves is difficult to estimate. Therefore, a systematic study of their influence would go beyond the scope of this work. However, our results agree, in general, with the studies of Bohlen and Saenger (2006) concerning staircase approximations of free-surface boundaries in numerical modeling of seismic wave propagation, as accurate simulations including topography or bathymetry (van Vossen *et al.*, 2002) require a much higher mesh resolution than those treating internal elastic interfaces. They show that surface waves are particularly sensitive to non-smooth topography. In contrast, for the Solid-Solid test cases a regular mesh with staircase approximation of material interfaces can generate acceptable results depending on the combination of mesh spacing, frequency, and material contrast. For seismic wave speed contrasts across a material discontinuity of 0.77 (Solid-Solid 1) only small differences in the seismograms are obtained even for relatively high frequencies and coarse meshes (see Fig. 4.3). An increase of the material contrast requires in turn an adjustment of either a higher mesh resolution or a reduction of the frequency.

Finally, we can establish rules, which should be adhered when modeling complex geological interfaces, especially with the DG approach using regular, structured meshes and which should also be considered in wave propagation modeling using other methods. First we define a threshold for classifying a seismogram to be acceptable. In our case, this threshold is defined as  $E_{\text{tot}} = 0.3$  above which seismograms are degenerated too much due to the geometrical representation of the interface. This threshold is shown as a dashed red line in all plots of Figs 4.14-4.16. As examples to clarify the meaning of

this threshold with respect to the seismic waveforms and their misfits we refer to the seismograms shown in Section 4.2.2. In Fig. 4.11 the horizontal component obtained at receiver r126 with frequency content f15 and mesh spacing h10 (green) has an error level  $E_i = 0.285$  and is therefore classified as just acceptable. A non-acceptable example is given in the same graphic for frequency f25 obtained with h10 (green) with  $E_i = 0.500$ . In contrast, a clearly acceptable horizontal seismogram is shown in Fig. 4.11 for receiver r111, frequency f25, and h10 (green), with  $E_i = 0.135$ .

If we now use the results shown e.g. in Fig. 4.15, none of our simulations of the Solid-Free Surface or Solid-Fluid cases produced acceptable seismograms. Therefore, we will focus on the different Solid-Solid test cases in the following. However, we point out that our tests consider a  $v_p/v_s$ -ratio of  $\sqrt{3}$  of a Poisson material. As shown recently by Moczo *et al.* (2010) the accuracy of most of the used numerical schemes decreases with increasing  $v_p/v_s$ -ratio and values of 5 and larger can occur in near-surface sedimentary structures. From each of the plots of Fig. 4.14 we use the acceptable data point with the highest error value but still below the red threshold line. Also, we use the non-acceptable data point with the lowest error level but larger than the error threshold. Using the information of the shortest dominant wavelength per mesh spacing for each test case given in Table 4.1 we can plot these data into the graph in Fig. 4.17 to determine a transition zone that separates two regions. Above the transition zone (grey shaded), bounded by the solid black line from above, the sampling in the sense of elements per wavelength is good enough for the particular material contrast to produce acceptable seismograms. Below the transition zone, bounded by the dashed red line from below, the sampling is insufficient and non-acceptable seismograms according to our threshold are obtained. Considering this result is extremely important for high-order accurate numerical schemes, like the DG or SEM methods, as such methods usually allow for large mesh spacings due to their high-order approximation properties within an element. In cases, where geometrically complicated material interfaces cannot be honored by mesh alignment or regular meshes are used for computational efficiency, it is crucial to respect the results represented in Fig. 4.17 to reduce numerical artifacts due to the staircase approximation. From Fig. 4.17 we also can conclude that low-order schemes using the staircase approximation naturally seem to overcome the problem of complex geometry as the number of grid points or elements per wavelength is typically chosen high enough (e.g. 8 grid points per wavelength) to obtain satisfying results. Furthermore, our results confirm the exceptionally fine mesh spacing required to model solid-fluid or solid-free surface contacts with methods which cannot align the mesh to such non-planar interfaces typically occurring for strong bathymetry or topography. For further details on this topic for FD schemes we refer to the work of Robertsson (1996) and Bohlen and Saenger (2006).

### 4.3. Multiple Layers with Undulating Interfaces

Since our previous study consist of a rather simple geometry with only one interface, we here construct a more complex situation representing a more realistic application. This test case contains three layers separated by two undulating interfaces with a material contrast of 0.5 each. The regular grid spacing of the quadrilateral mesh is constructed by

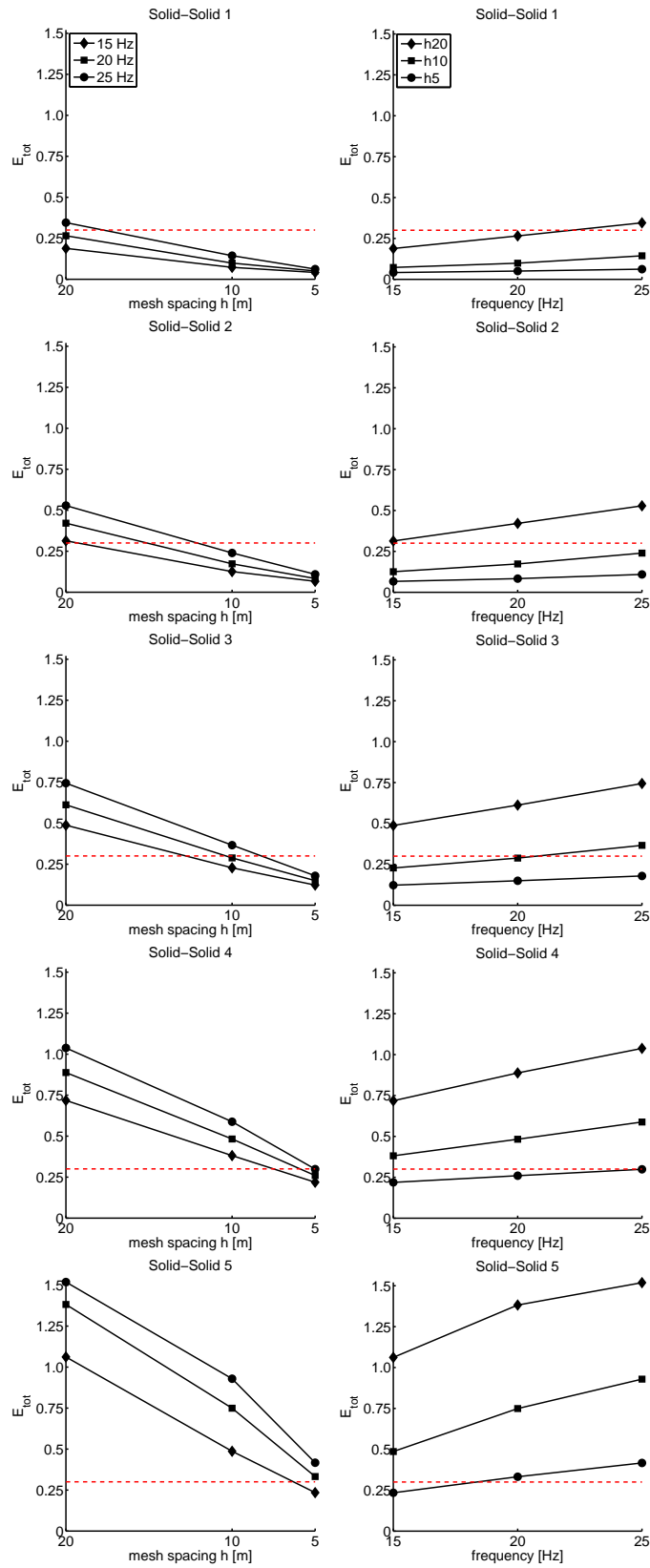


Figure 4.14.: Left: Error  $E_{tot}$  versus mesh spacing  $h$  with varying frequencies  $f$  for the different material contrasts. Right: Error  $E_{tot}$  versus frequency  $f$  with varying mesh spacing  $h$ . The threshold of acceptance is shown as a dashed red line.

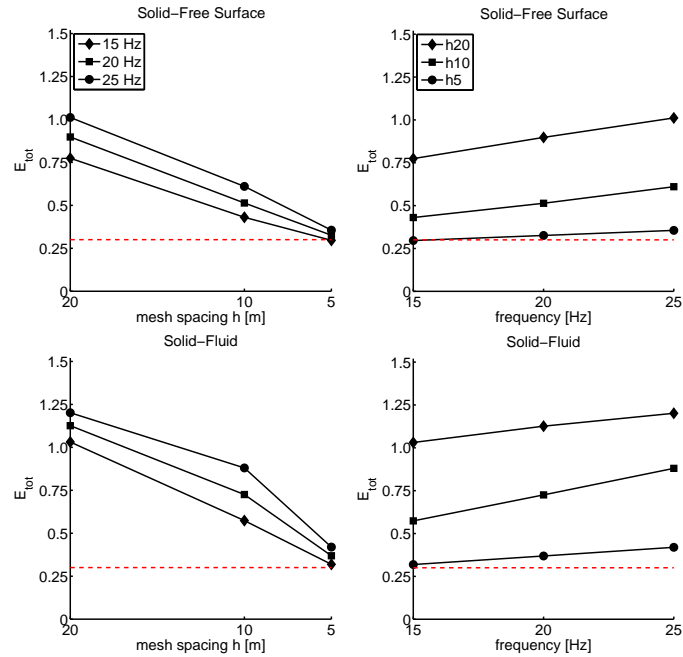


Figure 4.15.: Left: Error  $E_{tot}$  versus mesh spacing  $h$  with varying frequencies  $f$  for the different material contrasts. Right: Error  $E_{tot}$  versus frequency  $f$  with varying mesh spacing  $h$ . The threshold of acceptance is shown as a dashed red line.

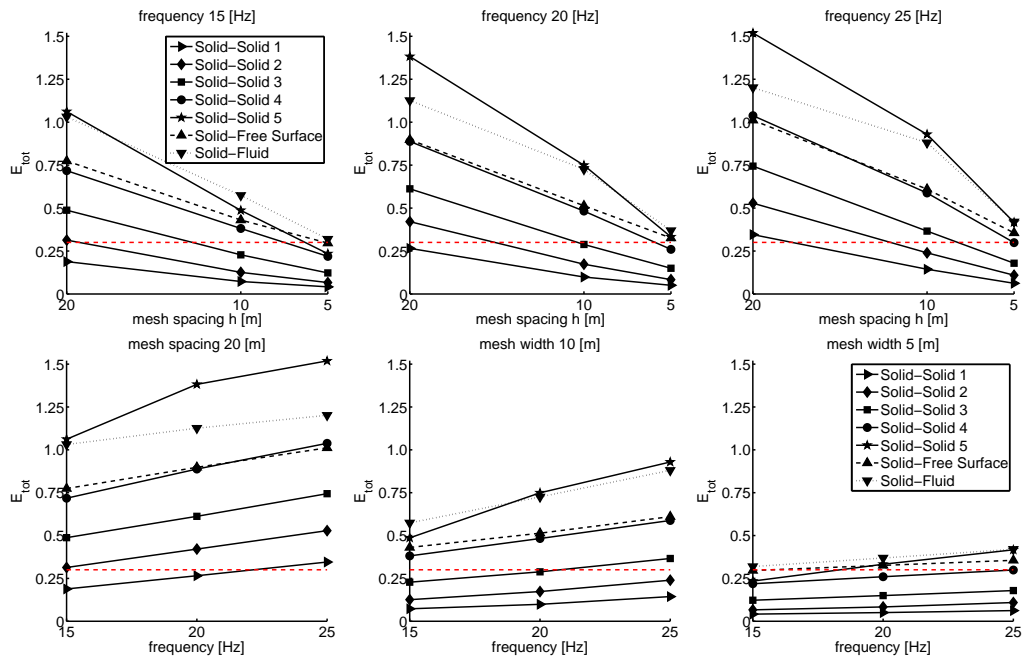


Figure 4.16.: Error  $E_{tot}$  versus mesh spacing  $h$  and frequency  $f$  respectively with varying material contrasts. The threshold of acceptance is shown as a dashed red line.

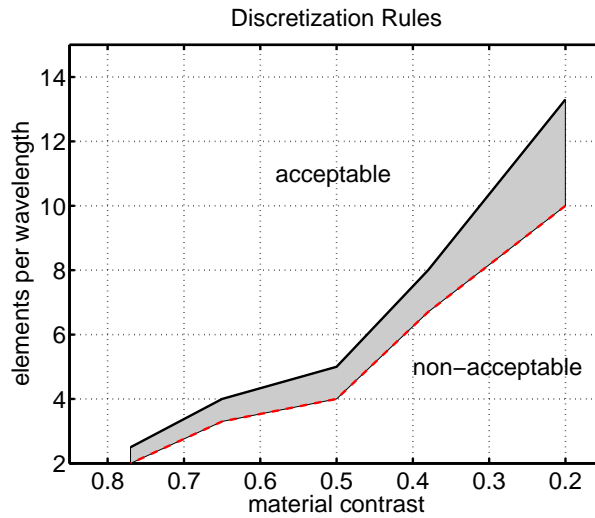


Figure 4.17.: Diagram representing the discretization rules by displaying what mesh spacing (measured in elements per shortest dominant wavelength) is required for a given material contrast to obtain acceptable seismograms above the black solid line. The material contrast between two materials 1 and 2 is given through the ratio of S-wave speeds  $v_{S,1}/v_{S,2}$ , with  $v_{S,1} \leq v_{S,2}$ . Values below the red dashed line produce non-acceptable results, while the grey shaded area denotes a transition zone.

respecting the rules of Section 4.2.3. Representative seismograms of selected receivers are analysed and discussed in detail.

### 4.3.1. Test Case Description

An overview of the layered model is given in Fig. 4.18 with material properties given in Table 4.2. The top boundary at  $z = 0$  m is a free surface, the bottom at  $z = -8000$  m is absorbing and the lateral boundaries are set periodic. The source is a point source at  $(x, z) = (10, -1990)$  m using a force pair on the two velocity components with a Ricker-type source time function of dominant frequency  $f = 8$  Hz. The total simulation time is 10 s.

Considering Fig. 4.17, we should be able to use a mesh spacing of 5 elements per dominant wavelength to represent an interface with material contrast 0.5 sufficiently accurate with a structured discretization. Like in Section 4.2, we cover a large part of the domain with a dense receiver array of  $31 \times 31$  receivers distributed within a rectangular area of  $(x, z) \in [-3000, 3000] \times [-6000, 0]$  m. The shortest dominant wavelengths for material 1 and 2 are 125 m and 250 m, respectively, leading to mesh spacings of  $h = 25$  m and  $h = 50$  m at the interfaces. The employment of a regular but non-conforming mesh (Hermann *et al.*, 2011) enables us to test both interfaces with their specific resolutions. In more specific terms, this means that we use a regular mesh spacing of  $h = 25$  m above  $z = -3000$  m and  $h = 50$  m below this depth. An example of the interface discretization by the structured grid is given in Fig. 4.18 (b). To ensure a correct resolution of the

Table 4.2.: Material properties used for the multiple layer application.

	$\rho$ [kg/m <sup>3</sup> ]	$v_P$ [m/s]	$v_S$ [m/s]
Material 1	1000.0	1732.1	1000.0
Material 2	2000.0	3464.1	2000.0
Material 3	4000.0	6928.2	4000.0

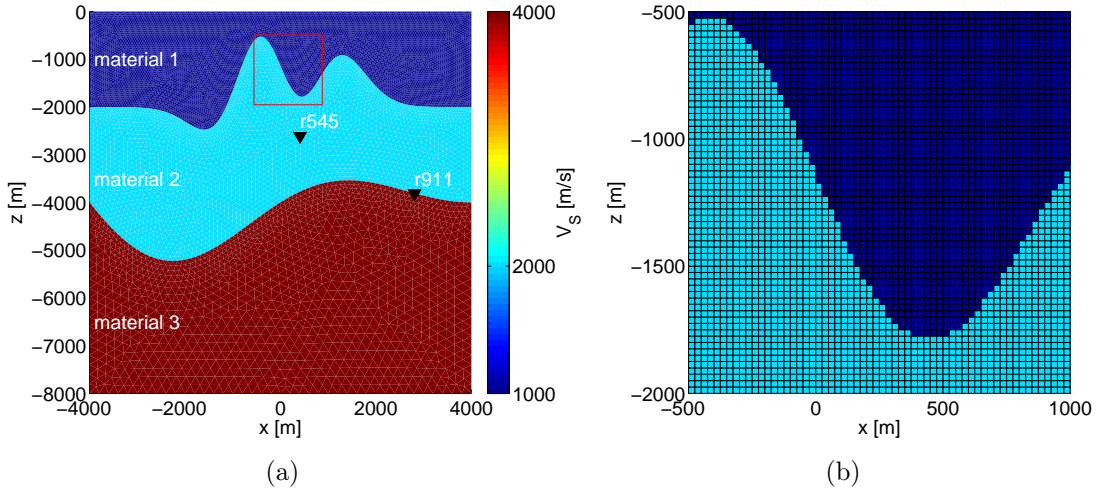


Figure 4.18.: (a) S-wave velocity distribution of the multiple layer application. The area within the red rectangular is zoomed in (b) together with an overlay of the quadrilateral mesh.

wave field we choose the approximation order 6 in space and time. Again, a reliable reference solution is produced using the same numerical method and order of accuracy on an unstructured edge-aligned triangular mesh with a resolution of 2.5 elements per shortest dominant wavelength.

### 4.3.2. Results and Discussion

The overall RMS error distribution is shown in Fig. 4.19 and its level is very small as expected. A clear error pattern with error concentrations at the material interfaces is much harder to recognize than in the test cases of Section 4.2.2. However, a trace of higher errors along the lower interface still can be identified. Our interpretation is that due to the complicated wave field, interface waves, multiple reflections, and transmissions the errors might locally sum up close to the interfaces. Therefore, the seismogram with the largest misfit is obtained by receiver r911 and one with a very small misfit by r545. The locations of these stations are denoted in the overview Fig. 4.18(a) and the seismograms together with their time-frequency envelope (TFEM) and phase (TFPM) misfits (Kristeková *et al.*, 2006, 2009) are shown in Figs 4.20 and 4.21, respectively, using Kristeková's signal analysis code from [www.nuquake.eu/Computer\\_Codes/index.html](http://www.nuquake.eu/Computer_Codes/index.html).

Obviously, the envelope misfits of both components at r911 are relatively large compared to the much smaller phase misfits. Furthermore, the misfits dominate in the frequency

Table 4.3.: Table of envelope misfit (EM), phase-misfit (PM) and corresponding goodness-of-fit values of envelope (EG) and phase (PG) for selected receivers r545 and r911.

	horizontal				vertical			
	EM [%]	EG	PM [%]	PG	EM [%]	EG	PM [%]	PG
r545	12.4	8.8	5.3	9.5	11.4	8.9	4.3	9.6
r911	32.5	7.2	11.4	8.9	24.9	7.8	12.0	8.8

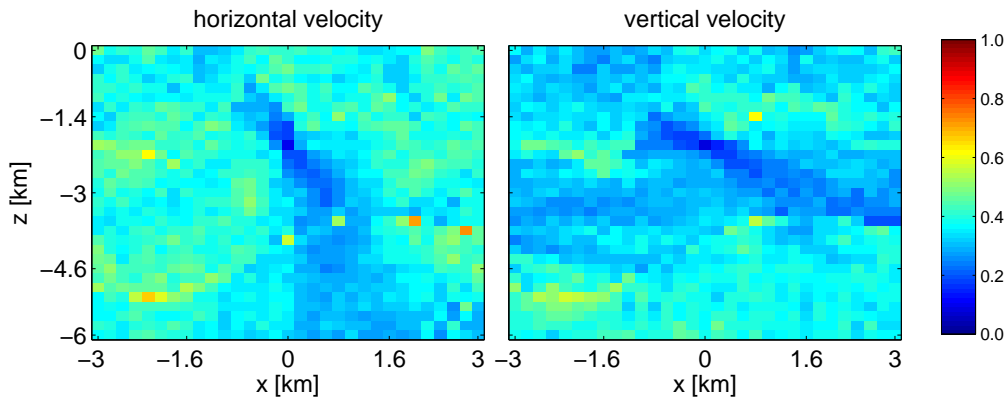


Figure 4.19.: Error maps of the RMS error  $E_i$  for the multiple layer test case.

range from  $f = 8$  Hz to  $2.5f = 20$  Hz as expected due to the dominant and maximum frequency content of the Ricker wavelet. However, most features of the wave forms can be found in both seismograms and the goodness-of-fit values (Kristeková *et al.*, 2009) are still equal or better than 7.2, which in the verbal classification is a 'good' result (Table 4.3). We point out that Anderson (2004), introducing this classification, used the empirical earthquake-engineering characteristics of earthquake ground motion and adjusted his scale to the fact that differences between synthetics and real records are in most cases large. Therefore, for comparisons of numerical solutions the chosen scale of the time-frequency goodness-of-fit might be too robust, as the comparison of numerical solutions typically has differences much less than those between synthetics and real records. Nevertheless, the seismograms at receiver r545 shown in Fig. 4.21 are in our opinion in a perfect agreement as underscored by the goodness-of-fit values equal or better than 8.8.

Note that this test case includes two non-planar interfaces and that the 10 s simulation time allows for the arrival of waves that crossed these interfaces several times. Furthermore, waves can travel through the model in the horizontal direction due to the periodic boundaries and could be strongly affected by the material interfaces. Nevertheless, our rules of Section 4.2.3 still hold. The structured mesh with 5 elements per shortest dominant wavelength seems to represent an arbitrarily shaped interface of material contrast 0.5 with satisfying accuracy.

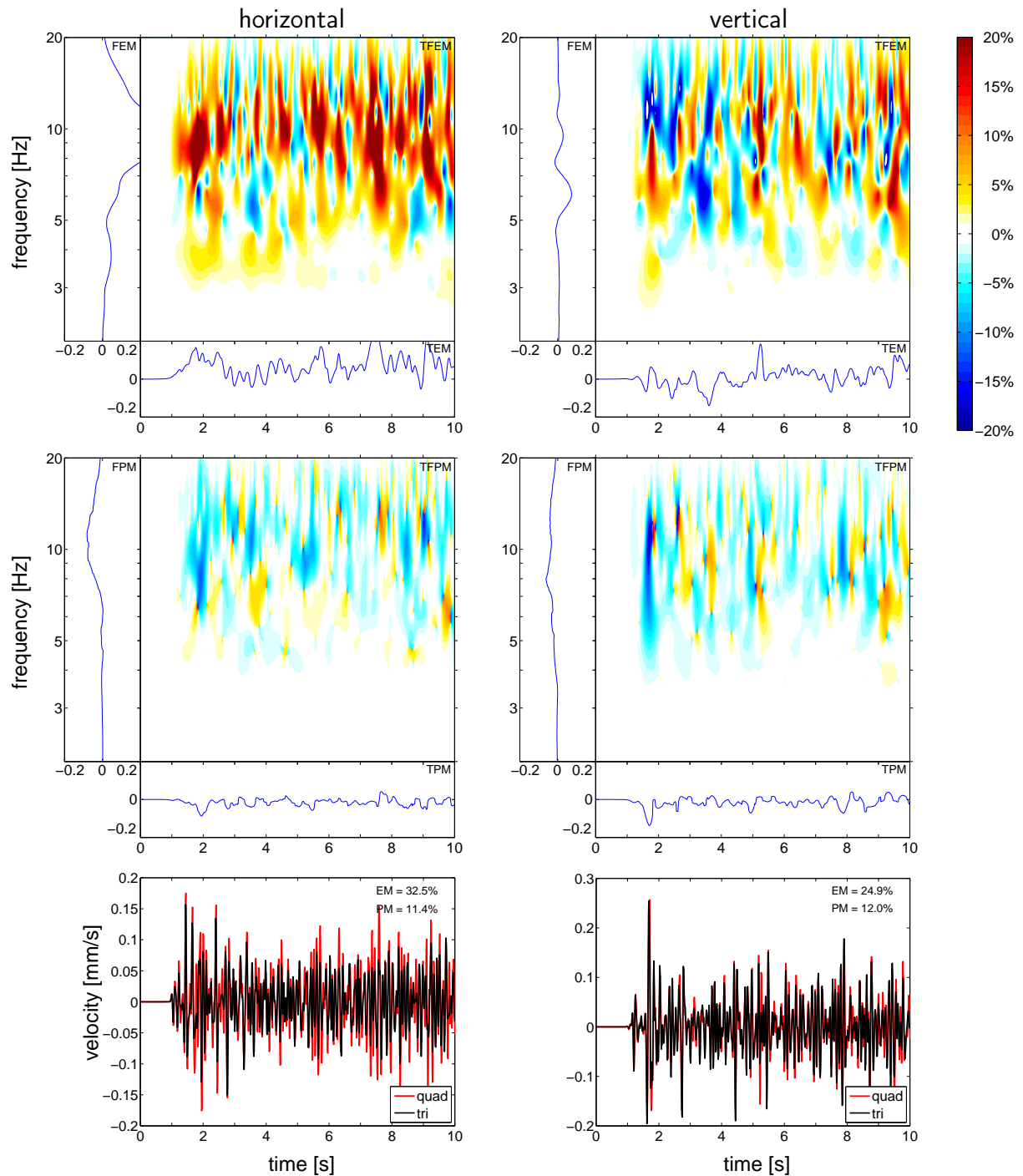


Figure 4.20.: Time-Frequency misfits of the horizontal and vertical velocity components of the worst receiver r911. We also show the seismograms comparison between the reference solution obtained on the triangular mesh (black) and the solution obtained on the quadrilateral mesh (red) together with their single-valued EM and PM of Table 4.3.

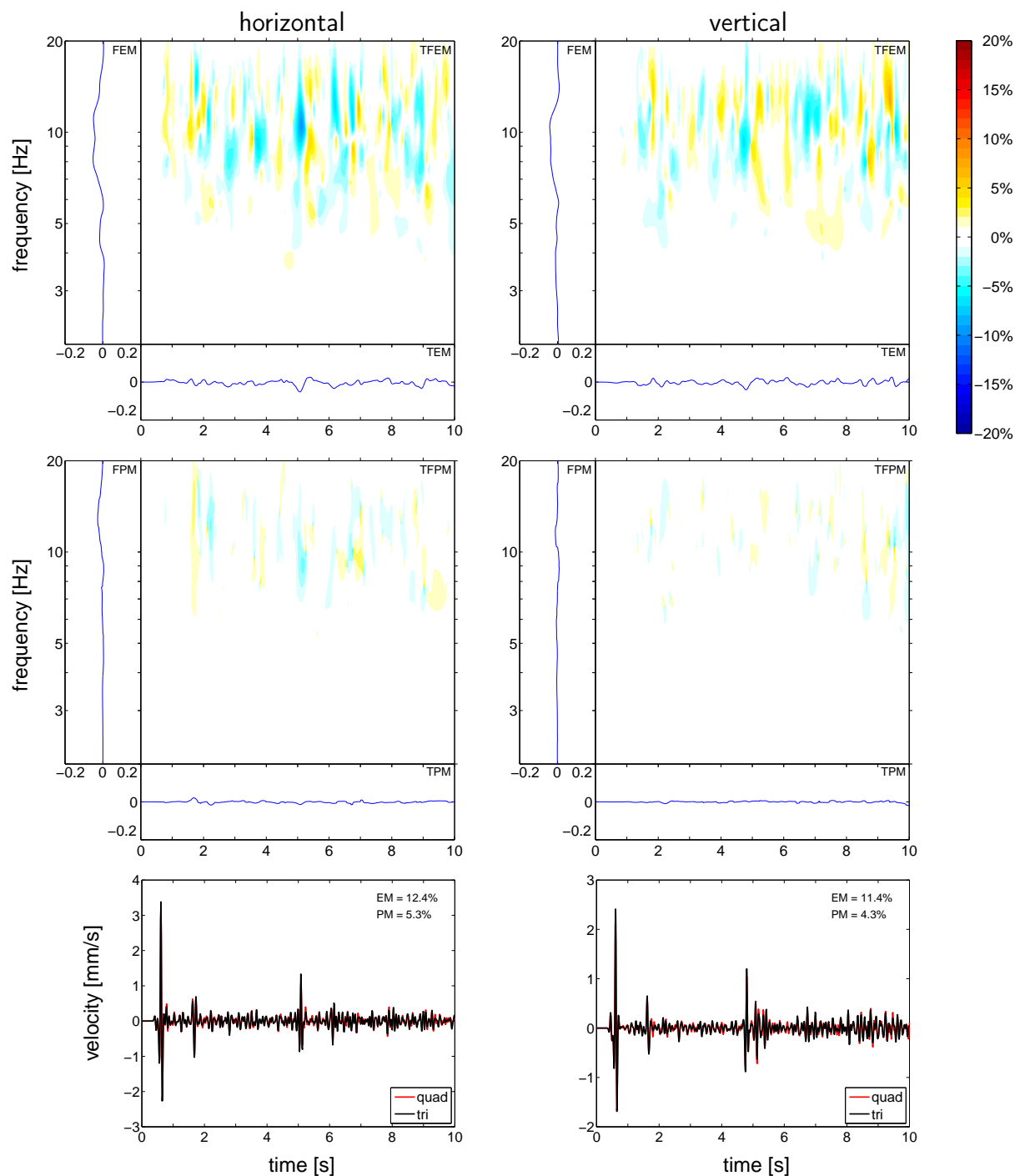


Figure 4.21.: Time-Frequency misfits of the horizontal and vertical velocity components of the receiver r545. We also show the seismograms comparison between the reference solution obtained on the triangular mesh (black) and the solution obtained on the quadrilateral mesh (red) together with their single-valued EM and PM of Table 4.3.

## 4.4. Sedimentary Basin

The accuracy and reliability of synthetic seismograms is of fundamental importance for the investigation of realistic modeling scenarios. Therefore, we use our previous study on the sensitivity of numerical seismograms on geometrically complex material interfaces and apply our resulting discretization rules on a realistic example of a sedimentary basin derived from the EuroseisTest Verification and Validation Project (Chaljub *et al.*, 2009). The aim is to test if the numerical effects of staircase approximations of curved boundaries are acceptable under the consideration of our proposed rules, as this would justify simple and fast regular mesh generation in contrast to a more involved mesh alignment procedure to well-defined material interfaces. Our simplified EuroseisTest model contains a strong discontinuity that separates the bedrock of constant seismic wave velocities from the basin with depth-dependent wave speeds producing moderate material contrasts from 0.32 at the deepest part of the basin to extreme contrasts of 0.1 close to the surface as shown in Fig. 4.22. In this Section, we check, if our rules hold also in a real world case, where a sedimentary basin with extremely low wave velocities is embedded in a high-velocity bedrock.

### 4.4.1. Test Case Description

The model setup is a simplified 2D version of the 'EuroseisTest Verification and Validation Project' model (Chaljub *et al.*, 2009) describing the geological setting of the Mygdonian sedimentary basin near the city of Thessaloniki in northern Greece as shown in Fig. 4.22(a). The vertical direction of the S-wave velocity structure is stretched by a factor of 3 for better visualization of the thin basin. The complete extension of the physical domain has 28.32 km width and 15 km depth. So only the part of the computational domain around the basin is shown. The free surface elevation is at  $z = 63$  m and the deepest point of the basin is at  $z = -319.6$  m. Within the basin the wave speeds depend on depth  $d$  from the surface and are constant for the bedrock as given in Table 4.4.

Thus, high S-wave velocity contrasts of 0.1 exist at the top left and right borders of the basin. With increasing depth the S-wave ratio continuously changes to 0.32 in  $d = -382.6$  m depth. In the following we select two positions, one with high and one with low material contrast, which will be discussed on the basis of recorded seismograms. Again, we use a  $21 \times 21$  receiver array to cover the basin and the adjacent bedrock but focus on two sets of receivers to illustrate representative results. These receiver stations are marked by six black triangles in Fig. 4.22(a). The two highlighted receiver sets cross the material discontinuity, which means that the lowest receiver is based in the bedrock (r218, r103), the middle close to the interface but already in the basin (r219, r104), and the topmost clearly inside the basin (r220, r105). As a source we choose again the force pair with a 5 Hz Ricker pulse of Section 4.3.1 located at  $(x, z) = (-4.5075 \cdot 10^6, -1000)$  m. The total simulation time is 10 s.

Like in the previous experiments material properties are assigned elementwise, but to achieve a better representation of the velocity gradient in the basin we first assign the material properties to the vertices of an element and average them in a second step. A

Table 4.4.: Material properties used for the sedimentary basin application.

	$\rho$ [kg/m <sup>3</sup> ]	$v_P$ [m/s]	$v_S$ [m/s]
basin	2100.0	$1000.0 + 100.0\sqrt{d}$	$200.0 + 32.0\sqrt{d}$
bedrock	2600.0	4500.0	2600.0

reference solution is produced with a fine triangular mesh respecting the material discontinuities by element edges and using a DG scheme of accuracy order 5.

Fig. 4.22(b) and (c) show a zoomed view of the left part of the basin with an overlay of the triangular and quadrilateral meshes, respectively. The triangles of the reference model have a mean edge size of 10 m in the basin and for the bedrock we allow a smooth increase to 100 m, enough to resolve the propagating waves properly. The mesh spacing for the regular mesh is 10 m in a box including the basin and 100 m around this box using the non-conforming mesh approach introduced by Hermann *et al.* (2011). An edge size of 100 m in the bedrock corresponds to 3.7 elements per shortest dominant wavelength, while the higher resolution of 10 m in the basin area leads to depth-dependent sampling of 2.8-11.7 elements per shortest dominant wavelength. Since large parts of the basin-bedrock interface lie in larger depth with material contrast of 0.32 an interface approximation using 10 elements per shortest dominant wavelength should be sufficient, as suggested by the graph in Fig. 4.17. We admit that this value represents a lower limit regarding our rules, however, we remark that even the regular mesh aligns well to the predominantly flat and smoothly varying basin-bedrock interface. At smaller depth the stronger material contrasts cause an undersampling of the interface geometry with 2.8 elements per shortest dominant wavelength, which is clearly less than what is required by our rules of Section 4.2.3. However, these cases appear only in very small areas near the borders of the basin at the surface. As computational efficiency is also an issue in real applications we deliberately avoid the very fine mesh spacing close to the surface to prohibit heavy oversampling of the interface in the deeper parts of the model and to keep the computational cost low. In the following we will show that even in such extreme cases where compromises have to be found we still obtain satisfactory results.

#### 4.4.2. Results and Discussion

As expected from Section 4.2.2 both discretization approaches produce similar seismograms except for small differences, since we are using less elements per wavelength than required by Section 4.2.3 in areas of extremely high material contrasts. Thus, we focus on two representative areas.

One of the best matching seismograms are recorded at receivers r218-r220 although they are located directly at the basin-bedrock interface and are shown in Fig. 4.23. While the arrival times fit almost perfectly, differences in amplitude can be observed in r219 and r220. A quantitative determination of the single-valued EM and PM criteria of Kristeková *et al.* (2009) shows a decrease of the misfit with increasing depth (Table 4.5). This means that seismograms in the bedrock are less affected by the geometry approximation than the ones in the basin. As numerous reflections are typical for low velocity basins embedded in

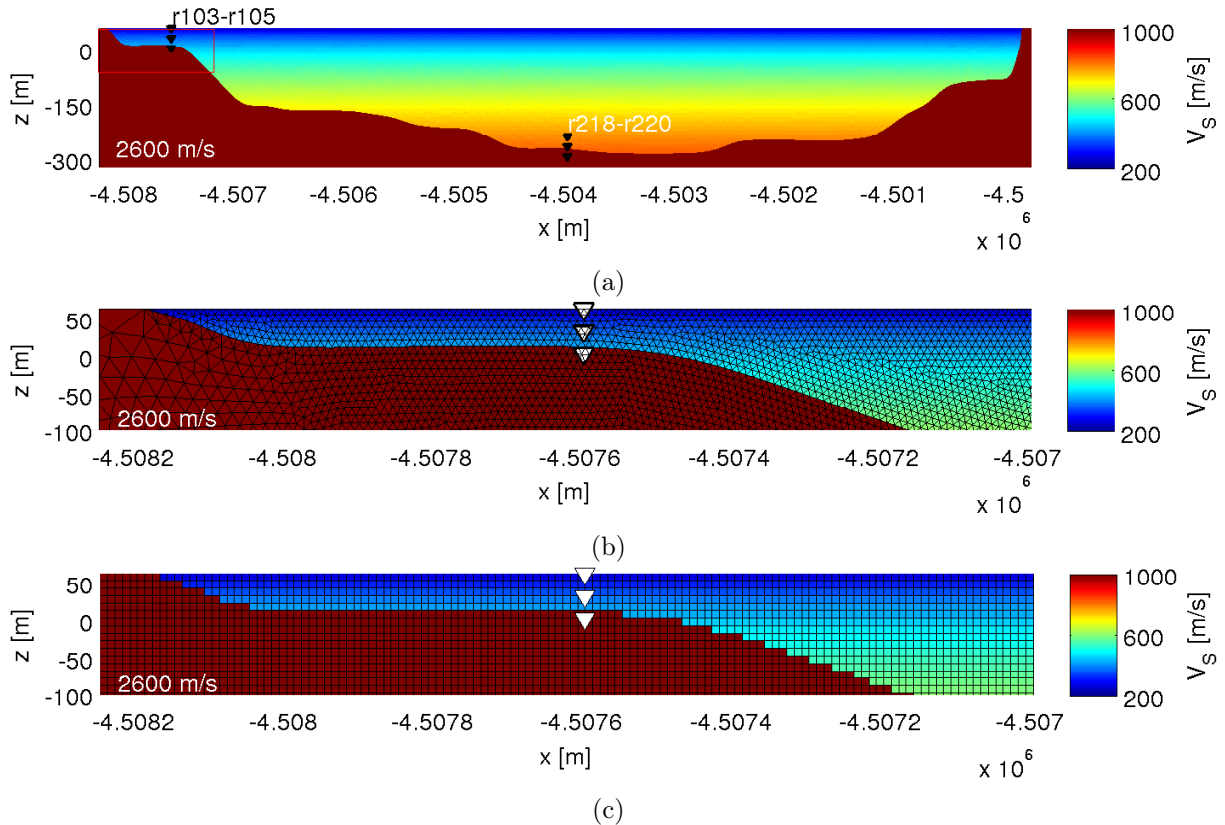


Figure 4.22.: (a) S-wave velocity structure of the basin model stretched in vertical direction by a factor of 3. (b) Zoomed section of the left border of the basin with an overlay of the triangular mesh which respects the interface of the bedrock. White triangles mark the positions of the three geophone positions r103-r105. (c) Same area as (b) but with an overlay of the quadrilateral mesh with staircase approximation of the interface.

Table 4.5.: Table of envelope misfit (EM), phase-misfit (PM) and corresponding goodness-of-fit values of envelope (EG) and phase (PG) for selected receivers.

	horizontal				vertical			
	EM [%]	EG	PM [%]	PG	EM [%]	EG	PM [%]	PG
r220	14.3	8.7	5.5	9.5	18.0	8.4	6.2	9.4
r219	20.4	8.2	8.1	9.2	10.8	9.0	3.2	9.7
r218	5.4	9.5	2.2	9.8	9.1	9.1	3.9	9.6
r105	23.7	7.9	29.0	7.1	12.6	8.8	15.1	8.5
r104	20.3	8.1	15.7	8.4	12.5	8.8	15.8	8.4
r103	3.7	9.6	3.7	9.6	6.0	9.4	4.2	9.6

high-velocity bedrock, it is expected that amplitude and phase errors are accumulating. However, the resulting goodness-of-fit values of around 9 confirm the excellent agreement. A time-frequency misfit analysis for the best matching receiver r218 is given in Fig. 4.25. Occurring errors are smaller than 10% and provide acceptable numerical seismograms obtained by the chosen staircase approximation. Furthermore, all receivers located in the bedrock and most of the stations in the basin show similar well matching seismograms.

In contrast, receivers r103-r105 located in a very shallow region of the basin and close to the basin-bedrock interface show the largest differences of all receivers. In this area the basin has a depth of only 50 m. Hence, the resulting S-wave speed ratio is 0.16. Due to the high material contrast and the vicinity to the left boundary numerical effects due to insufficient geometry approximation are most prevalent here. The corresponding seismograms are shown in Fig. 4.24. Although still satisfactory a regress to a goodness-of-fit value of 8 or even 7 is observable for receivers r104 and r105 (Table 4.5). r103 is located in the bedrock and as mentioned above is less affected by the geometry approximation effects, which results in a significantly smaller misfit. Actually, seismograms of r103 are among the best matching seismograms of all, while the largest misfits appear only 30 m or 60 m above at receivers r104 and r105. Most obvious are the strong phase misfits at receivers r104 and r105 starting after 3 s as shown in the time-frequency analysis for receiver r105 in Fig. 4.26. Here, strong envelope misfits are also observed directly after the first arrival on the horizontal component and after 3 s on the vertical component. These critical misfit levels can be explained by the lower number of elements per wavelength for the interface approximation in this area than suggested in Section 4.2.3.

However, with respect to the different discretization approaches and the compromise between computational effort and approximation accuracy of the material interface, the agreement between the seismograms is still remarkably good. Furthermore, we mention that the obtained results still provide goodness-of-fit values of 'good' or 'excellent', which are reasonable for comparisons of synthetics in benchmarks of seismic wave propagation scenarios.

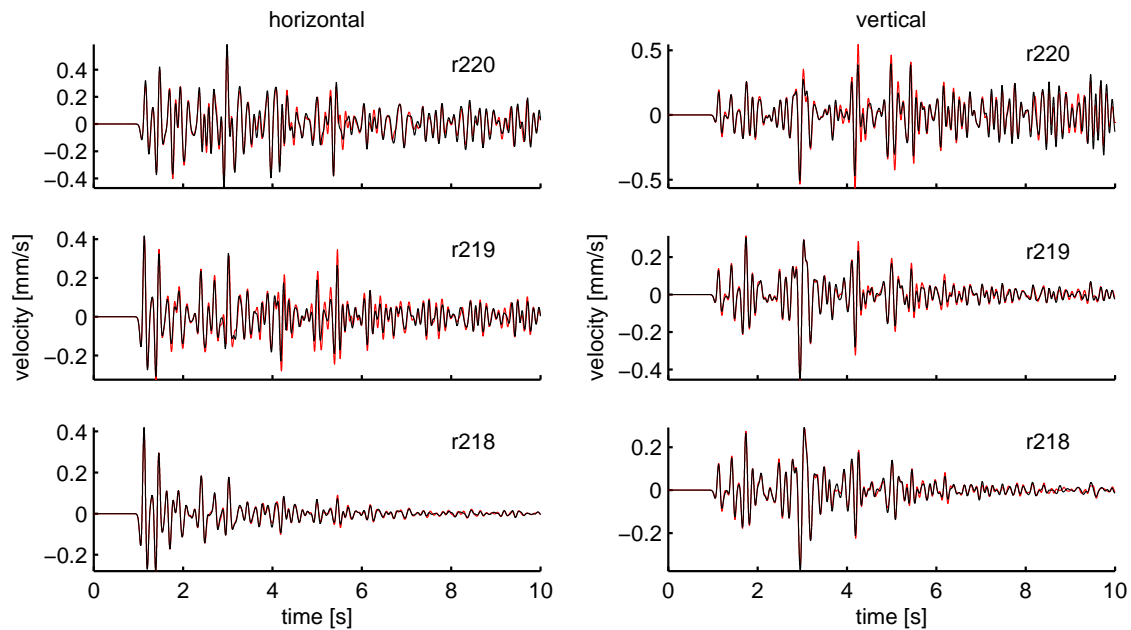


Figure 4.23.: Seismograms of the receiver set r218-r220 located in the middle of the basin. The seismogram in the lowermost plot (r218) is recorded in the bedrock, the other two are 30 m and 60 m above already in the basin. The black line denotes the reference solution, the red line the seismogram obtained using the quadrilateral mesh.

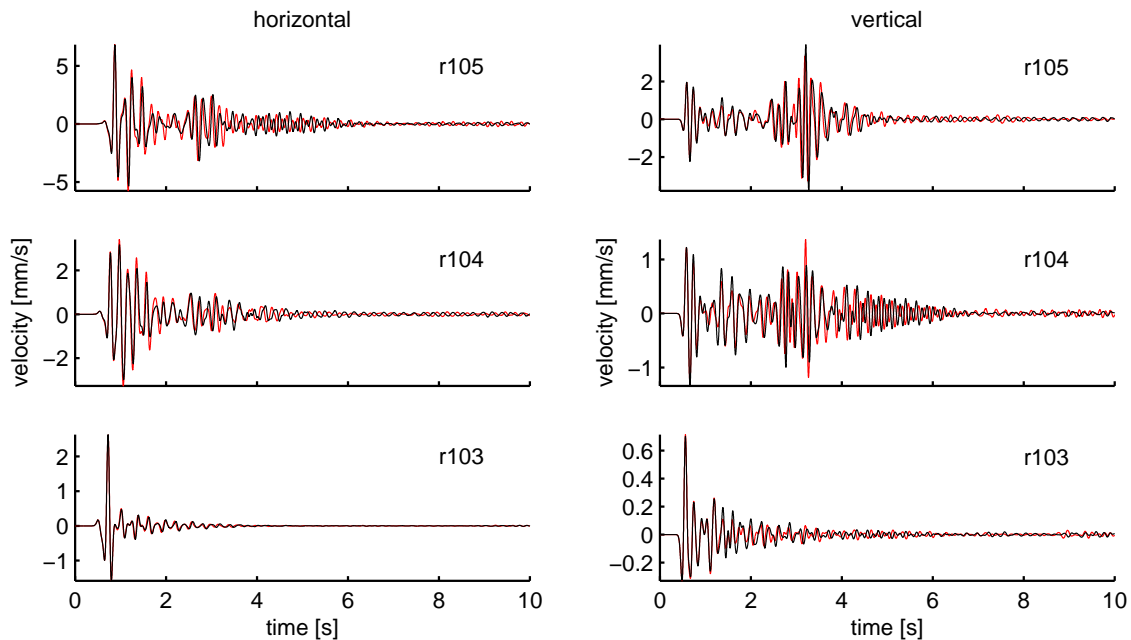


Figure 4.24.: Seismograms of the receiver set r103-r105 located in the middle of the basin. The seismogram in the lowermost plot (r103) is recorded in the bedrock, the other two are 30 m and 60 m above already in the basin. The black line denotes the reference solution, the red line the seismogram obtained using the quadrilateral mesh.

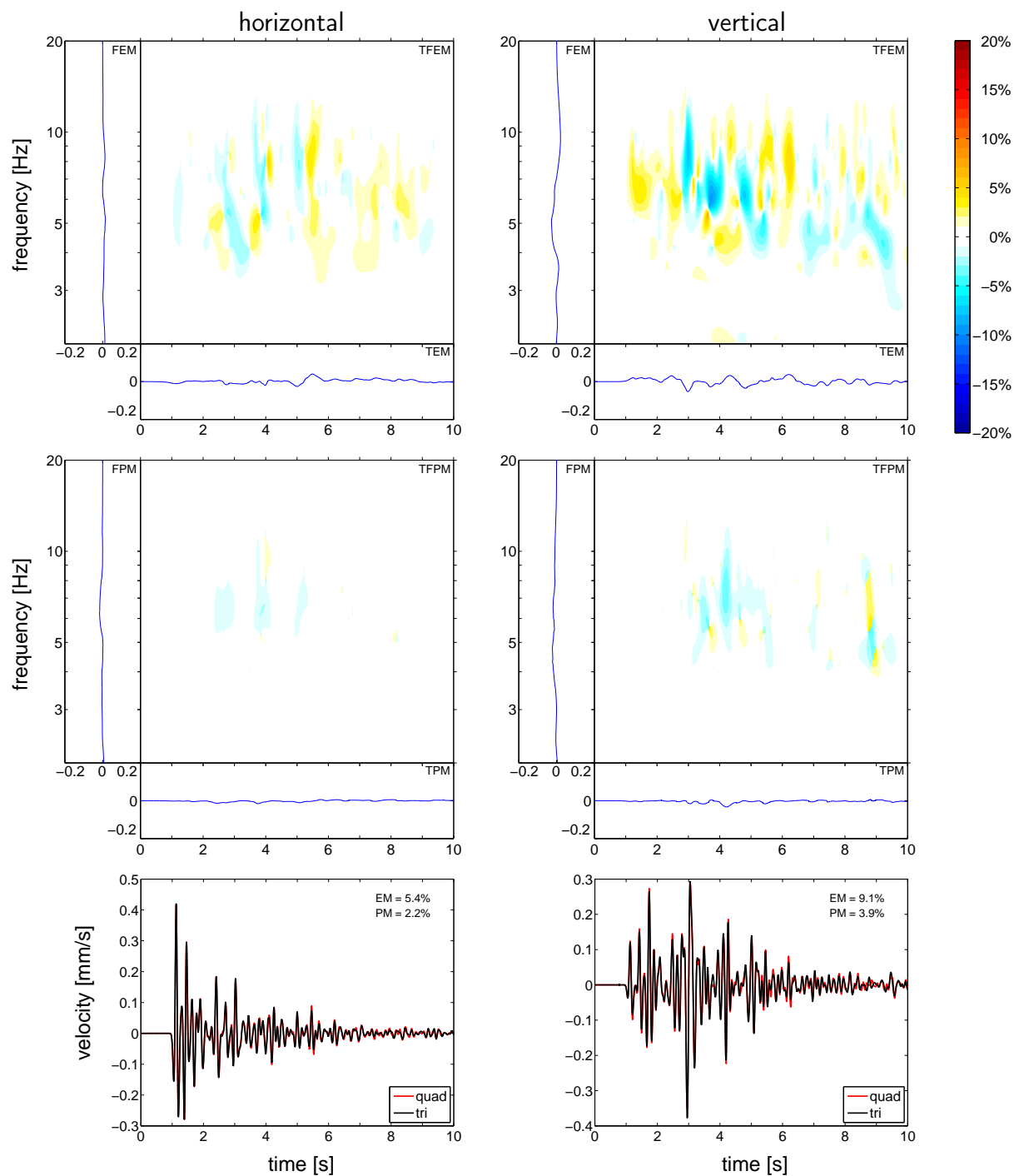


Figure 4.25.: Time-Frequency misfits of the horizontal and vertical velocity components of receiver r218. We also show the seismograms comparison between the reference solution obtained on the triangular mesh (black) and the solution obtained on the quadrilateral mesh (red) together with their single-valued EM and PM of Table 4.5.

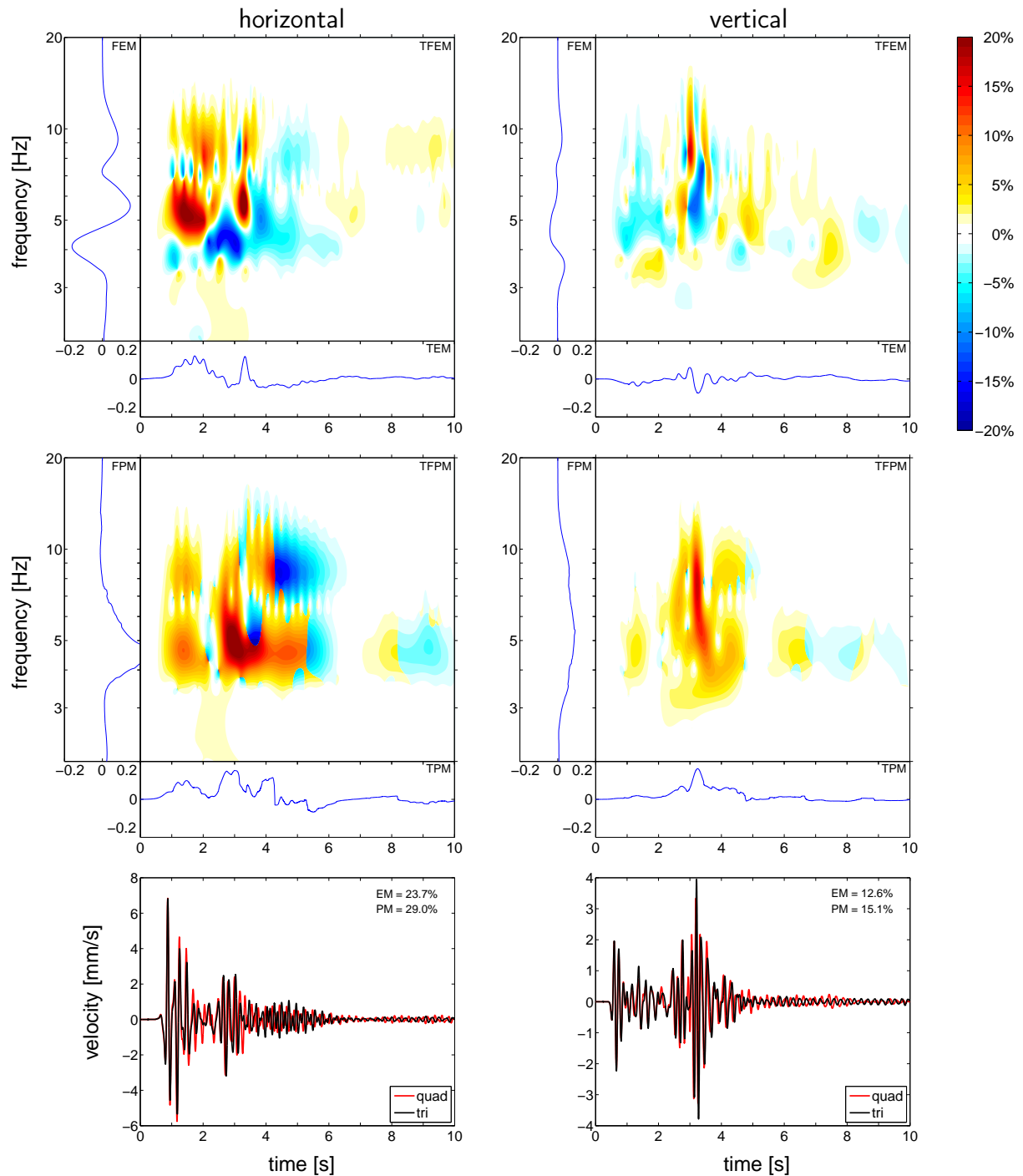


Figure 4.26.: Time-Frequency misfits of the horizontal and vertical velocity components of receiver r105. We also show the seismograms comparison between the reference solution obtained on the triangular mesh (black) and the solution obtained on the quadrilateral mesh (red) together with their single-valued EM and PM of Table 4.5.

## 4.5. Conclusions

In this work, we investigated the effect of staircase approximations of material discontinuities along curved interfaces using a Discontinuous Galerkin (DG) Finite Element method trying to clarify under which conditions such geometry approximations, typically used by regular grid schemes like FD, provide acceptable results. We produced reference solutions using a high-order accurate DG scheme on triangular meshes which can be aligned to the geometry of curved interfaces. We then solved the wave equations on regular square-shaped meshes leading to jagged material contacts. We studied the misfits of seismograms depending on the signal frequency, the mesh spacing, and the material contrast. In fact, the misfits increase with a decreasing number of elements per wavelength and with increasing material contrast. The systematic parameter study of Section 4.2 enabled us to define rules that should be adhered to ensure high quality synthetic data, if regular meshing is applied. A general finding was that up to a material contrast, in the sense of a S-wave speed ratio, of 0.5 a discretization of 5 elements per shortest dominant wavelength generates acceptable seismograms in spite of complex material interfaces. Furthermore, high-order accurate numerical methods can reduce this resolution on structured grids for weaker material contrasts. However, in the case of stronger material contrasts than 0.5 the number of elements per wavelength has to be increased significantly to avoid numerical artifacts due to the staircase approximation. Special cases of a free-surface boundary or an acoustic-elastic coupling should be treated by mesh alignment to the interface as we were not able to produce acceptable seismograms within the range of tested frequencies and mesh spacings with the staircase approximation of such boundaries.

In Section 4.3, we considered a more complicated test case to verify our discretization rules containing a three layer problem separated by two undulating interfaces with material contrasts of 0.5 each and using a minimum number of elements for geometry approximation. In summary, all seismograms show the expected minor misfits compared to the reference solution.

Finally, we applied our results to a realistic scenario of a basin structure. The main issue was to find a compromise between a correct resolution of the material interface and computational efficiency. At the shallow basin boundaries where extremely high material contrasts occur we used less elements per wavelength than suggested by our rules to keep the computational cost low and still obtain good matching seismograms. As expected, the largest but surprisingly moderate misfits can be found in these areas. However, these critical areas are very localized and therefore do not seem to influence the overall error or the accuracy in other areas dramatically. Nevertheless, the surprising result is that even for such untypically high material contrasts over a basin-bedrock interface close to the surface we still obtained a satisfying accuracy of the synthetic seismograms although a structured mesh is applied, which does not respect the material interface.

We conclude that taking into account our approximation rules defined in this study ensures reliable modeling results when using structured discretizations including non-planar material interfaces. Furthermore, adhering these rules can help to minimize the mesh generation effort and computational cost. Conclusions for high-order methods, like SEM and DG, applied on structured meshes can also be drawn. If the material properties allow for large elements these coarse meshes can violate the interface geometry to a certain

degree and do not have to be aligned exactly with them in order to produce acceptable results. On the other hand, we remark that fine discretizations often required by low-order methods often account for the geometry with sufficient accuracy automatically.

## Chapter 5.

# Three-Dimensional Dynamic Rupture Simulation with a High-order Discontinuous Galerkin Method on Unstructured Tetrahedral Meshes

Accurate and efficient numerical methods to simulate dynamic earthquake rupture and wave propagation in complex media and complex fault geometries are needed to address fundamental questions in earthquake dynamics, to integrate seismic and geodetic data into emerging approaches for dynamic source inversion and to generate realistic physics-based earthquake scenarios for hazard assessment. Modeling of spontaneous earthquake rupture and seismic wave propagation by a high-order discontinuous Galerkin (DG) method combined with an Arbitrarily high-order DERivatives (ADER) time integration method was introduced in 2D by de la Puente *et al.* (2009). The ADER-DG method enables high accuracy in space and time and discretization by unstructured meshes. Here we extend this method to three-dimensional dynamic rupture problems. The high geometrical flexibility provided by the usage of tetrahedral elements and the lack of spurious mesh reflections in ADER-DG allows the refinement of the mesh close to the fault, to model the rupture dynamics adequately while concentrating computational resources only where needed. Moreover, ADER-DG does not generate spurious high-frequency perturbations on the fault and hence does not require artificial Kelvin-Voigt damping. We verify our three-dimensional implementation by comparing results of the SCEC TPV3 test problem with two well established numerical methods, finite differences and spectral boundary integral. Furthermore, a convergence study is presented to demonstrate the systematic consistency of the method. To illustrate the capabilities of the high-order accurate ADER-DG scheme on unstructured meshes we simulate an earthquake scenario, inspired by the 1992 Landers earthquake, that includes curved faults, fault branches and surface topography.

---

This chapter presents the work of Christian Pelties, Josep de la Puente, Jean-Paul Ampuero, and Martin Käser published in *Journal of Geophysical Research, Solid Earth* (2012) in a slightly modified form.

## 5.1. Introduction

Strong ground motion simulations of earthquakes require, in order to describe natural phenomena, the proper description and modeling of several features, e.g. seismic source representation, geometry of fault systems, material properties of the bedrock and sediment, topography. A highly accurate solution of the resulting wave field is also essential. The seismic source can be described through a prescribed evolution of slip along the fault or by prescribing physical criteria for earthquake rupture and letting the fault slip be a spontaneous consequence of the state of the fault. The two approaches are called kinematic and dynamic fault representation, respectively. The advantage of dynamic source modeling is that one can investigate how the fault interacts with the surrounding conditions such as confining stress, free-surface or transient wavefields. Furthermore, the influence on the rupture process of the fault geometry and potential heterogeneities are taken into account. As a drawback, dynamic rupture modeling is much more challenging computationally and suffers from large uncertainties on the underlying physics.

Many numerical algorithms have been tested in the past to model dynamic earthquake rupture, such as finite differences (FD) (e.g. Andrews, 1973; Day, 1982; Madariaga *et al.*, 1998; Andrews, 1999; Day *et al.*, 2005; Dalguer and Day, 2007; Moczo *et al.*, 2007a), boundary integral (BI) (e.g. Das, 1980; Andrews, 1985; Cochard and Madariaga, 1994; Geubelle and Rice, 1995; Lapusta *et al.*, 2000; Tada and Madariaga, 2001), finite volume (FV) (e.g. Benjema *et al.*, 2007, 2009), finite element (FE) (e.g. Oglesby *et al.*, 1998, 2000; Aagaard *et al.*, 2001; Galis *et al.*, 2008) or spectral element (SE) (e.g. Ampuero, 2002; Vilotte *et al.*, 2006; Kaneko *et al.*, 2008; Galvez *et al.*, 2011) methods. All these methods provide certain advantages, but have also disadvantages. For instance, schemes implemented on structured and regular grids are in general efficient to solve very large problems but have difficulties in modeling non-planar faults and strong material contrasts, like in sedimentary basins with extremely low wave velocities, which require grid adaptivity. The BI method is one of the most accurate methods but is impractical in heterogeneous media and non-linear materials. FV and FE methods can be implemented on unstructured meshes, which gives flexibility to describe realistic fault and crustal model geometries. However, they are usually formulated as low-order accurate operators that are very dispersive, which affects the small-scale resolution in the near-field and in turn the rupture front evolution. In contrast, SE methods are high-order accurate for seismic wave propagation, but are limited to hexahedral elements, which penalizes geometrical flexibility: it remains challenging to generate hexahedral meshes for complex three dimensional branched fault systems with smooth element refinement or coarsening that adapts to material properties. Furthermore, all approaches suffer from spurious high-frequency oscillations, most notably in the slip-rate time series. Several approaches have been proposed in order to reduce these oscillations, e.g. spatial low-pass filtering (Ampuero, 2002), absorption by a frequency-selective Perfectly Matched Layer surrounding the fault (Festa and Vilotte, 2005, 2006), adding an ad-hoc Kelvin-Voigt damping term to the solution (Day *et al.*, 2005) or adaptive smoothing algorithms (Galis *et al.*, 2010). None of these solutions is completely satisfactory and high-frequency oscillations remain an unsolved nuisance in the numerical modeling of dynamic rupture.

A new approach to overcome these issues was first presented by de la Puente *et al.* (2009). They incorporated the earthquake source physics into a discontinuous Galerkin (DG) scheme linked to an arbitrary high-order derivatives (ADER) time integration (Titarev and Toro, 2002; Käser and Iske, 2005; Dumbser and Käser, 2006). The DG method combines ideas from FE methods, where a polynomial basis approximates the physical variables of the elastic wave equations inside each element, and FV methods, introducing the desired concept of numerical fluxes. In addition to providing a high-order accurate approximation of the physical variables, the flux concept favors data locality: the temporal update of the solution inside one element depends only on its direct neighbors. Therefore, the method is well suited for massively parallel high-performance facilities. This formulation enables the use of fully unstructured meshes, i.e. triangles (2D) or tetrahedrons (3D), to better represent the geometrical constraints of a given geological setting and in particular the fault. The fault is honored by the mesh and can be sampled with small elements in order to capture small-scale rupture phenomena. Fast mesh coarsening with increasing distance from the fault reduces the computational cost without introducing significant spurious grid reflections. Between any two elements the approximated variables of the elastic wave equation are discontinuous in a DG discretization. In our case, fluxes are defined by the exact solution of the elastic wave equations at a discontinuity (Godunov state) to exchange information between elements. Such kind of problem is known as the Riemann problem (Toro, 1999; LeVeque, 2002). At a fault, de la Puente *et al.* (2009) showed how the exact solution of the Godunov state has to be modified to take the frictional boundary conditions into account. An important result of their study was that the ADER-DG solution is very smooth and free of spurious high-frequency oscillations. Therefore, it does not require artificial Kelvin-Voigt damping or filtering. The good numerical dispersion properties of the ADER-DG method (Dumbser *et al.*, 2006; Käser *et al.*, 2008; Hu *et al.*, 1999; Sherwin, 2000), the possibility of using unstructured meshes (Pelties *et al.*, 2010), and the natural representation of variables' discontinuities with Godunov fluxes (de la Puente *et al.*, 2009) might be key features for accurate and efficient dynamic rupture simulations in very complex scenarios.

The main goal of this paper is the extension of the ADER-DG rupture modeling scheme to three-dimensional problems on tetrahedral meshes. We present the Riemann problem for the three-dimensional case and show how its solution is used to compute high-order accurate numerical fluxes. We further use these fluxes together with a DG discretization of the elastodynamic system to build up a highly accurate fault modeling and wave propagation algorithm. The accuracy and convergence properties of the method are shown in convergence tests. Further verification is obtained by comparing the results of our novel 3D DG dynamic rupture scheme with other well established numerical solutions in a standard community test problem of fault rupture. Finally, a large earthquake simulation including complex fault systems, inspired from the 1992 Landers earthquake, shows the potential of the method in dealing with complicated geometrical constraints both in the rupture process and in the wave propagation itself.

## 5.2. Dynamics of Fault Rupture

In the classical three-dimensional dynamic rupture models considered here a fault is represented by a 2D plane of arbitrary shape (or a set of planes in a fault system with branches) across which fault coplanar displacements can be discontinuous. The kinematics of the sliding process are described by the spatio-temporal distribution of the slip vector  $\Delta \mathbf{d} = \mathbf{d}^+ - \mathbf{d}^-$ , or the slip rate vector  $\Delta \mathbf{v} = \dot{\Delta \mathbf{d}}$ , where  $\mathbf{d}^\pm$  are the displacements on each side of the fault, in the directions tangential to the fault plane (see Fig. 5.1a). Earthquakes may involve small-scale fault opening, especially at shallow depth but, for simplicity, here we consider only examples in which both sides of the fault remain in contact. On any point of the fault surface,  $\sigma_n > 0$  represents the compressive normal stress and  $\boldsymbol{\tau}$  the shear traction vector resolved on the + side of the fault. The dynamics of the sliding process are governed by friction relations between traction and slip (Andrews, 1976a,b; Day *et al.*, 2005). The shear traction is bounded by the fault strength,  $\tau_s$ , which is proportional to the normal stress via the friction coefficient  $\mu_f$ :

$$\tau_s = \mu_f \sigma_n. \quad (5.1)$$

Active slip requires the shear traction to reach and remain at the fault strength level, with a direction anti-parallel to the slip rate. These conditions are encapsulated in the following equations for Coulomb friction:

$$\begin{aligned} |\boldsymbol{\tau}| &\leq \tau_s, \\ (|\boldsymbol{\tau}| - \tau_s) |\Delta \mathbf{v}| &= 0, \\ \Delta \mathbf{v} |\boldsymbol{\tau}| + |\Delta \mathbf{v}| \boldsymbol{\tau} &= 0. \end{aligned} \quad (5.2)$$

The evolution of the friction coefficient with ongoing slip is described by the following linear slip weakening friction law:

$$\mu_f = \begin{cases} \mu_s - \frac{\mu_s - \mu_d}{D_c} \delta & \text{if } \delta < D_c, \\ \mu_d & \text{if } \delta \geq D_c. \end{cases} \quad (5.3)$$

where  $\delta(t) = \int_0^t |\Delta \mathbf{v}| dt'$  is the slip path length. With increasing  $\delta$  the friction coefficient  $\mu_f$  drops linearly from the static value  $\mu_s$  to the dynamic value  $\mu_d$  over the critical slip distance  $D_c$ , as shown in Fig. 5.1b. In combination with equations (5.2) the linear slip weakening friction law is capable of modeling initial rupture, arrest of sliding and reactivation of slip. Since it is very simple and easy to implement, it is well suited to verifying numerical methods with dynamic rupture boundary condition. More advanced, realistic friction laws, incorporate rate-and-state effects (Dieterich, 1979; Ruina, 1983) and thermal phenomena such as flash heating and pore pressure evolution (Lachenbruch, 1980; Mase and Smith, 1985, 1987; Rice, 1999). We do not expect any fundamental issue in the implementation of other friction laws in the ADER-DG method and leave that for future work.

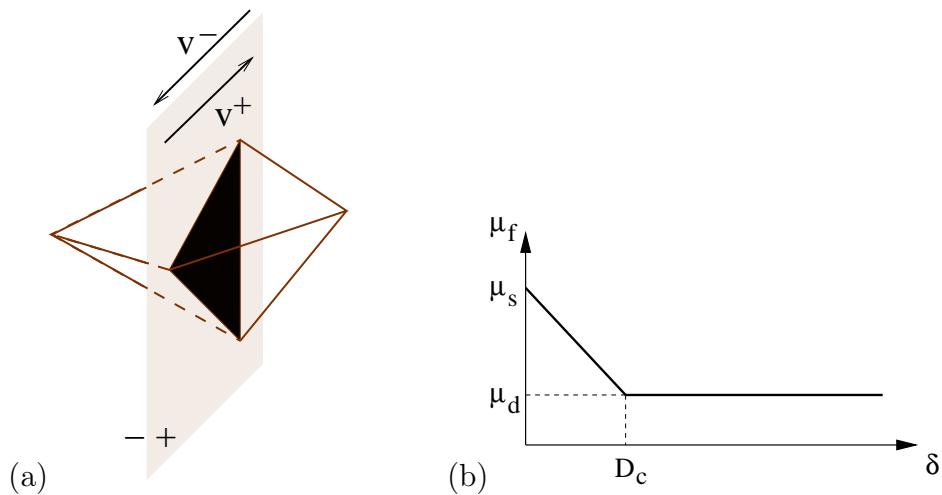


Figure 5.1.: In (a) is depicted a fault segment discretized as the contact surface of two tetrahedral elements. The different fault sides are indicated by plus and minus. In (b) we plot the friction coefficient  $\mu_f$  vs. the slip  $\delta$  for the linear slip weakening friction law.

### 5.3. Fault Dynamics within the Discontinuous Galerkin Framework

In contrast to other numerical dynamic rupture implementations, like the traction-at-split-node (TSN) approach (Andrews, 1973, 1999; Day, 1982), de la Puente *et al.* (2009) followed a new idea employing the concept of fluxes. A detailed description of the adopted DG scheme can be found in Dumbser and Käser (2006). The mathematical and technical analysis of dynamic rupture boundary conditions in a high-order DG formulation was presented by de la Puente *et al.* (2009) in 2D. Therefore, in this section we will explain only the basic ideas and show the extension to three-dimensional spontaneous rupture problems.

### 5.3.1. Discretization of the Linear Elastic Wave Equation

The three-dimensional elastodynamic equations for an isotropic medium are written in velocity-stress form as the linear hyperbolic system

$$\begin{aligned}
\frac{\partial}{\partial t}\sigma_{xx} - (\lambda + 2\mu)\frac{\partial}{\partial x}u - \lambda\frac{\partial}{\partial y}v - \lambda\frac{\partial}{\partial z}w &= 0, \\
\frac{\partial}{\partial t}\sigma_{yy} - \lambda\frac{\partial}{\partial x}u - (\lambda + 2\mu)\frac{\partial}{\partial y}v - \lambda\frac{\partial}{\partial z}w &= 0, \\
\frac{\partial}{\partial t}\sigma_{zz} - \lambda\frac{\partial}{\partial x}u - \lambda\frac{\partial}{\partial y}v - (\lambda + 2\mu)\frac{\partial}{\partial z}w &= 0, \\
\frac{\partial}{\partial t}\sigma_{xy} - \mu\left(\frac{\partial}{\partial x}v + \frac{\partial}{\partial y}u\right) &= 0, \\
\frac{\partial}{\partial t}\sigma_{yz} - \mu\left(\frac{\partial}{\partial z}v + \frac{\partial}{\partial y}w\right) &= 0, \\
\frac{\partial}{\partial t}\sigma_{xz} - \mu\left(\frac{\partial}{\partial z}u + \frac{\partial}{\partial x}w\right) &= 0, \\
\rho\frac{\partial}{\partial t}u - \frac{\partial}{\partial x}\sigma_{xx} - \frac{\partial}{\partial y}\sigma_{xy} - \frac{\partial}{\partial z}\sigma_{xz} &= 0, \\
\rho\frac{\partial}{\partial t}v - \frac{\partial}{\partial x}\sigma_{xy} - \frac{\partial}{\partial y}\sigma_{yy} - \frac{\partial}{\partial z}\sigma_{yz} &= 0, \\
\rho\frac{\partial}{\partial t}w - \frac{\partial}{\partial x}\sigma_{xz} - \frac{\partial}{\partial y}\sigma_{yz} - \frac{\partial}{\partial z}\sigma_{zz} &= 0,
\end{aligned} \tag{5.4}$$

where  $\lambda$  is the first Lamé constant,  $\mu$  is the shear modulus,  $\rho$  is the density,  $\sigma_{ij}$  are the components of the stress tensor and  $u$ ,  $v$  and  $w$  are the components of the particle velocity in the  $x$ ,  $y$ , and  $z$  directions, respectively. Grouping stresses and velocities into a vector  $\mathbf{Q} = (\sigma_{xx}, \sigma_{yy}, \sigma_{zz}, \sigma_{xy}, \sigma_{yz}, \sigma_{xz}, u, v, w)^T$ , we write the system of equations (5.4) in a more compact form:

$$\frac{\partial Q_p}{\partial t} + A_{pq}\frac{\partial Q_q}{\partial x} + B_{pq}\frac{\partial Q_q}{\partial y} + C_{pq}\frac{\partial Q_q}{\partial z} = 0, \tag{5.5}$$

where the space-dependent Jacobian matrices  $A$ ,  $B$  and  $C$  include the material properties. Classical tensor notation and Einstein's summation convention are assumed.

The computational domain  $\Omega$  is divided into conforming tetrahedral elements  $T^{(m)}$  identified by an index  $m$ . The physical variables  $\mathbf{Q}$  are approximated within each tetrahedral element  $T^{(m)}$  by high-order polynomials

$$Q_p^m(\boldsymbol{\xi}, t) = \hat{Q}_{pl}^m(t)\Phi_l(\boldsymbol{\xi}), \tag{5.6}$$

where  $\Phi_l$  are orthogonal basis functions and  $\boldsymbol{\xi} = (\xi, \eta, \zeta)$  are the local coordinates in a canonical reference element  $T_E$ , where all the computations are done. Note, that we are using a modal basis formulation. The physical variables are expressed by a linear combination of these basis functions with time-dependent coefficients  $\hat{Q}_{pl}^m(t)$ . The index  $p$  is associated with the unknowns in the vector  $\mathbf{Q}$ . The index  $l$  indicates the  $l$ -th basis function and ranges from 0 to  $L - 1$ , where  $L = (N + 1)(N + 2)(N + 3)/6$  is the number of required basis functions for a polynomial degree  $N$ . The numerical approximation order is  $\mathcal{O} = N + 1$ .

The elastic wave equation is solved in the weak form. We multiply equation (5.5) by a test function  $\Phi_k$  and integrate over an element  $T^{(m)}$  and over a time increment of size  $\Delta t$ :

$$\begin{aligned} & \int_t^{t+\Delta t} \int_{T^{(m)}} \Phi_k \frac{\partial Q_p}{\partial t} dV dt \\ & + \int_t^{t+\Delta t} \int_{T^{(m)}} \Phi_k \left( A_{pq} \frac{\partial Q_q}{\partial x} + B_{pq} \frac{\partial Q_q}{\partial y} + C_{pq} \frac{\partial Q_q}{\partial z} \right) dV dt = 0. \end{aligned} \quad (5.7)$$

Integration by parts of equation (5.7) yields

$$\begin{aligned} & \int_t^{t+\Delta t} \int_{T^{(m)}} \Phi_k \frac{\partial Q_p}{\partial t} dV dt + \sum_{j=1}^4 \mathcal{F}_{pk}^j \\ & - \int_t^{t+\Delta t} \int_{T^{(m)}} \left( \frac{\partial \Phi_k}{\partial x} A_{pq} + \frac{\partial \Phi_k}{\partial y} B_{pq} + \frac{\partial \Phi_k}{\partial z} C_{pq} \right) Q_q dV dt = 0. \end{aligned} \quad (5.8)$$

Equation (5.8) provides the values of  $Q_p$  at time  $t + \Delta t$ , following the procedures explained by Käser and Dumbser (2006) and Dumbser and Käser (2006). In those papers the integration of the first and third terms in equation (5.8) are fully elaborated. A thorough analysis of the used high-order accurate ADER time integration can be found in (Dumbser *et al.*, 2006). The second term is the sum of numerical fluxes  $\mathcal{F}_{pk}^j$  across the four faces of a tetrahedral element ( $j = 1, 2, 3, 4$ ) accounting for the discontinuity of  $\mathbf{Q}$ . This term achieves the exchange of information between elements. The incorporation of dynamic rupture boundary conditions is based on a modification of these fluxes. Thus, we will have a closer look at them in the next section.

### 5.3.2. Flux computation

For simplicity, we consider a single tetrahedral face with its normal aligned with the  $x$  axis. The flux term in (5.8) can then be written as

$$\mathcal{F}_{pk} = A_{pr} \int_t^{t+\Delta t} \int_S \Phi_k \tilde{Q}_r dS dt, \quad (5.9)$$

where  $\tilde{\mathbf{Q}}$  stands for a suitable approximation of the unknowns on the fault and the integral covers the face  $S$  and a time interval of size  $\Delta t$ . In order to solve the integrals numerically, we evaluate  $\mathbf{Q}$  at a set of space-time Gaussian integration points on the tetrahedral face at space locations  $\boldsymbol{\xi}_i = (\xi_i, \eta_i, \zeta_i)$ , with  $i = 1, \dots, (N+2)^2$ , and along the time axis at time levels  $\tau_l \in [t, t + \Delta t]$ , with  $l = 1, \dots, N+1$ . We define  $\mathbf{Q}_{il} = \mathbf{Q}(\boldsymbol{\xi}_i, \tau_l)$  and  $Q_{p,il} = Q_p(\boldsymbol{\xi}_i, \tau_l)$ . We solve the flux locally at each space-time integration point while ensuring causality by updating the time levels in a sequential way. At special boundaries, such as the free-surface or faults, the values of  $\tilde{\mathbf{Q}}$  in (5.9) might be imposed in order to satisfy the physical boundary conditions. In the particular case of dynamic faults, we impose values derived from the Coulomb friction model (5.2).

At a given time  $\tau \in [t, t + \Delta t]$ , a suitable temporal expansion of the variables is obtained via a Taylor expansion of order  $\mathcal{O} = N + 1$  with respect to time  $t$ :

$$Q_p(\boldsymbol{\xi}, \tau) \approx \sum_{k=0}^N \frac{(\tau - t)^k}{k!} \frac{\partial^k Q_q(\boldsymbol{\xi}, t)}{\partial t^k}. \quad (5.10)$$

The high-order time derivatives in (5.10) are substituted by spatial derivatives using the expression (5.5) in an iterative way

$$\frac{\partial^k Q_p(\boldsymbol{\xi}, t)}{\partial t^k} = (-1)^k \left( A_{pq} \frac{\partial}{\partial x} + B_{pq} \frac{\partial}{\partial y} + C_{pq} \frac{\partial}{\partial z} \right)^k Q_q(\boldsymbol{\xi}, t). \quad (5.11)$$

This yields

$$Q_p(\boldsymbol{\xi}, \tau) \approx \sum_{k=0}^N \frac{(\tau - t)^k}{k!} (-1)^k \left( A_{pq} \frac{\partial}{\partial x} + B_{pq} \frac{\partial}{\partial y} + C_{pq} \frac{\partial}{\partial z} \right)^k Q_q(\boldsymbol{\xi}, t). \quad (5.12)$$

The expansion (5.12) provides a high-order prediction of the evolution of the degrees of freedom. We compute it at each time substep  $\tau_l$ , separately for the states  $\mathbf{Q}^+(\boldsymbol{\xi}, t)$  and  $\mathbf{Q}^-(\boldsymbol{\xi}, t)$  of the two elements on the + and the - side of the face across which the flux is evaluated (see Fig. 5.1a). This yields predicted states  $\mathbf{Q}_{il}^+$  and  $\mathbf{Q}_{il}^-$ .

As mentioned above, between any two elements the variables of the elastic wave equations are in general discontinuous. A partial differential equation problem with discontinuous initial conditions is called a Riemann problem. The solution of the Riemann problem at an element interface is the Godunov state and can be written in terms of explicit values as (Toro, 1999; LeVeque, 2002; de la Puente *et al.*, 2009)

$$\begin{aligned} 2\sigma_{xx,il}^G &= (\sigma_{xx,il}^+ + \sigma_{xx,il}^-) + \rho c_p (u_{il}^- - u_{il}^+), \\ 2\sigma_{xy,il}^G &= (\sigma_{xy,il}^+ + \sigma_{xy,il}^-) + \frac{\mu}{c_s} (v_{il}^- - v_{il}^+), \\ 2\sigma_{xz,il}^G &= (\sigma_{xz,il}^+ + \sigma_{xz,il}^-) + \frac{\mu}{c_s} (w_{il}^- - w_{il}^+), \\ 2u_{il}^G &= (u_{il}^+ + u_{il}^-) + \frac{1}{\rho c_p} (\sigma_{xx,il}^- - \sigma_{xx,il}^+), \\ 2v_{il}^G &= (v_{il}^+ + v_{il}^-) + \frac{c_s}{\mu} (\sigma_{xy,il}^- - \sigma_{xy,il}^+), \\ 2w_{il}^G &= (w_{il}^+ + w_{il}^-) + \frac{c_s}{\mu} (\sigma_{xz,il}^- - \sigma_{xz,il}^+). \end{aligned} \quad (5.13)$$

The stresses  $\sigma_{yy}, \sigma_{zz}, \sigma_{yz}$  are associated to the so-called zero wave speeds and do not contribute to the Godunov state. Equations (5.13) are readily evaluated based on the predicted states  $\mathbf{Q}_{il}^+$  and  $\mathbf{Q}_{il}^-$ .

When the fault is locked, the Godunov state is used in place of  $\tilde{\mathbf{Q}}$  in the flux (5.9). When active slip is expected, we have to impose the shear stresses  $\sigma_{xy,il}$  and  $\sigma_{xz,il}$  on

the fault according to the Coulomb friction model (5.2) to obtain new traction values  $\tilde{\sigma}_{xy,il}$  and  $\tilde{\sigma}_{xz,il}$ , which might be different from  $\sigma_{xy,il}^G$  and  $\sigma_{xz,il}^G$ . Note that fault-normal and fault-parallel components are uncoupled in equations (5.13). Because we ignore the possibility of fault opening, the Godunov state values are assigned to the fault-normal component of stress and velocity,  $\tilde{\sigma}_{xx,il} = \sigma_{xx,il}^G$  and  $\tilde{u}_{il} = u_{il}^G$ . We can now evaluate the fault strength defined in equation (5.1):

$$\tau_s = \mu_{f,il}(\sigma_{xx,il}^G + \sigma_{xx,i}^0), \quad (5.14)$$

where the superscript zero denotes the initial stress values. The value of the friction coefficient is taken from the previous iteration and is updated later if active slip is detected.

To solve for the friction conditions we seek an independent relation between the fault-parallel variables of  $\tilde{\mathbf{Q}}$  derived from the structure of the fluxes. Substituting  $\sigma_{xy,il}^G$  and  $\sigma_{xz,il}^G$  in equations (5.13) with their imposed values  $\tilde{\sigma}_{xy,il}$  and  $\tilde{\sigma}_{xz,il}$ , then multiplying the second and third equations by  $c_s/\mu$  and subtracting or adding the fifth and sixth equations, respectively, leads to

$$\begin{aligned} \tilde{v}_{il}^+ &= v_{il}^+ + \frac{c_s}{\mu} (\tilde{\sigma}_{xy,il} - \sigma_{xy,il}^+) & \text{and} & & \tilde{v}_{il}^- &= v_{il}^- - \frac{c_s}{\mu} (\tilde{\sigma}_{xy,il} - \sigma_{xy,il}^-), \\ \tilde{w}_{il}^+ &= w_{il}^+ + \frac{c_s}{\mu} (\tilde{\sigma}_{xz,il} - \sigma_{xz,il}^+) & \text{and} & & \tilde{w}_{il}^- &= w_{il}^- - \frac{c_s}{\mu} (\tilde{\sigma}_{xz,il} - \sigma_{xz,il}^-). \end{aligned} \quad (5.15)$$

These expressions are crucial for the understanding of fault dynamics using fluxes, as they state that an imposed shear traction instantly and locally generates an imposed velocity parallel to the fault. By subtracting them, the two components of slip rate are obtained:

$$\begin{aligned} \Delta\tilde{v}_{il} &= \frac{2c_s}{\mu} (\tilde{\sigma}_{xy,il} - \sigma_{xy,il}^G), \\ \Delta\tilde{w}_{il} &= \frac{2c_s}{\mu} (\tilde{\sigma}_{xz,il} - \sigma_{xz,il}^G). \end{aligned} \quad (5.16)$$

These expressions capture explicitly the analytical form of the immediate slip velocity response to changes in fault tractions, also known as radiation damping (Cochard and Madariaga, 1994; Geubelle and Rice, 1995). A consequence of the equations in (5.16) is that slip (non zero  $\Delta\tilde{v}_{il}$  or  $\Delta\tilde{w}_{il}$ ) occurs only if  $\tilde{\sigma}_{xy,il} \neq \sigma_{xy,il}^G$  or  $\tilde{\sigma}_{xz,il} \neq \sigma_{xz,il}^G$ . The friction solver amounts to find the shear traction and slip rate (both vectors) that satisfy equations (5.2) and (5.16). The resulting algorithm is described next.

We first test if the Godunov state satisfies the failure criterion

$$|\boldsymbol{\tau}^G| \geq \tau_s, \quad (5.17)$$

where  $|\boldsymbol{\tau}^G| = \sqrt{(\sigma_{xy,il}^G + \sigma_{xy,i}^0)^2 + (\sigma_{xz,il}^G + \sigma_{xz,i}^0)^2}$ . If this inequality is not satisfied the fault is locked and the Godunov state values are assigned to all variables,  $\tilde{\mathbf{Q}}_{il} = \mathbf{Q}_{il}^G$ .

Otherwise, active slip is declared and we compute  $\tilde{\sigma}_{xy,il}$  and  $\tilde{\sigma}_{xz,il}$  as

$$\begin{aligned}\tilde{\sigma}_{xy,il} &= \frac{\sigma_{xy,il}^G + \sigma_{xy,i}^0}{|\boldsymbol{\tau}^G|} \tau_s, \\ \tilde{\sigma}_{xz,il} &= \frac{\sigma_{xz,il}^G + \sigma_{xz,i}^0}{|\boldsymbol{\tau}^G|} \tau_s.\end{aligned}\tag{5.18}$$

Next, the slip path length  $\delta_{il}$  is obtained by integrating (5.16). Therefore, we apply the linear slip weakening friction law (5.3) to update the friction coefficient for the next iteration as

$$\mu_{f,il+1} = \max \left\{ \mu_d, \mu_s - \frac{\mu_s - \mu_d}{D_c} \delta_{il} \right\}.\tag{5.19}$$

Using the shear stresses  $\tilde{\sigma}_{xy,il}$  and  $\tilde{\sigma}_{xz,il}$  and the velocities from (5.15) all values of  $\tilde{\mathbf{Q}}$  at the interface are known and the flux (5.9) can be computed with the discrete expression

$$\mathcal{F}_{pk} = A_{pr} \sum_{i=1}^{(N+2)^2} \sum_{l=1}^{N+1} \omega_i^S \omega_l^T \Phi_k(\boldsymbol{\xi}_i) \tilde{Q}_{r,il}.\tag{5.20}$$

where  $\omega_i^S$  and  $\omega_l^T$  are the weights of the spatial and temporal Gaussian integration, respectively.

## 5.4. Verification

For geophysically relevant dynamic rupture problems no analytical solution exists that could be used as a reference for code verification. Therefore, the Southern California Earthquake Center (SCEC) created the Dynamic Earthquake Rupture Code Verification Exercise, in which different codes and methodologies are compared on a suite of benchmark problems of increasing complexity (Harris *et al.*, 2009). Here, we verify our method with the Test Problem Version 3 (TPV3). Additionally, in section 5.4.2 the convergence of the ADER-DG method is discussed.

### 5.4.1. Code verification on the SCEC TPV3

The TPV3 problem involves rupture on a 30 km long by 15 km deep vertical strike-slip fault embedded in a homogeneous elastic full-space. The fault is governed by linear slip weakening friction and bounded by unbreakable barriers. The initial fault stresses are homogeneous except on a nucleation zone of higher initial shear stress (Fig. 5.2). The friction parameters and background stresses can be found in Table 5.1. The medium has density  $\rho = 2670 \text{ kg/m}^3$ , P-wave velocity  $c_p = 6000 \text{ m/s}$  and S-wave velocity  $c_s = 3464 \text{ m/s}$ . We use a conservatively large computational domain, a cube of edge length 72 km, to avoid spurious reflections from non-perfectly absorbing boundaries.

We compare our  $\mathcal{O}4$  ADER-DG solution with the results of the spectral boundary integral equation (SBIE) method of Geubelle and Rice (1995) and of a second-order staggered-grid finite difference method with traction at split nodes (Day *et al.*, 2005). In particular,

we considered two codes that have been verified during the SCEC exercises, the SBIE implementation of E.M. Dunham (MDSBI: Multidimensional spectral boundary integral, version 3.9.10, 2008, available at <http://pangea.stanford.edu/~edunham/codes/codes.html>) and the finite difference code DFM (Dynamic Fault Model) of Day *et al.* (2005). Both codes were run with a 50 m grid spacing. DFM incorporates artificial Kelvin-Voigt viscosity (Day and Ely, 2002).

We discretize the model by an unstructured mesh of tetrahedra. The edge length on the fault plane is  $h = 200$  m on average. We allow the size of the tetrahedral elements in the bulk to increase gradually to 3000 m edge length, to reduce the computational effort. No artificial reflections possibly caused by the mesh coarsening are observed. To facilitate a fair comparison between the methods we define an equivalent mesh spacing  $\Delta x = h/(N + 1)$ , which accounts for the sub-cell resolution of our high-order DG scheme. Although  $\Delta x$  is not consensually accepted as an exact measure of the spatial resolution it is often used for comparing different discretization techniques. The relatively large element size of our ADER-DG simulation,  $h = 200$  m, corresponds to an equivalent mesh spacing of  $\Delta x = 50$  m, the same as in the DFM and MDSBI computations considered here.

Figs. 5.3a, b, c and d show, for all three schemes, the time series of the shear stress and slip rate at the two fault locations indicated as PI and PA in Fig. 5.2, which probe the in-plane and anti-plane rupture fronts, respectively, at hypocentral distance 7500 m and 6000 m, respectively. The ADER-DG solution (black) is in excellent agreement with the results produced by MDSBI (blue) and DFM (red). The signal amplitudes, the arrival time of the rupture front and stopping phases and the subsequent stress relaxation are mutually consistent. A closer inspection of these results (Figs. 5.3e and f) reveals that the rupture front arrives slightly earlier in DFM than in the other two methods, whereas the rupture times of MDSBI and ADER-DG are more similar. These differences could be due to the Kelvin-Voigt damping in DFM or to different implementations of the non-smooth initial stress conditions.

Spurious high-frequency oscillations are visible in the slip rates produced by MDSBI and DFM, especially around the slip rate peak at the PA station. These are identified clearly in the spectra in Figs. 5.3g and h: the MDSBI slip rates have a significant spectral peak around 25 Hz and DFM has peaks between 10 and 40 Hz, especially at PA. Such spurious peaks are absent from the slip rate spectra of ADER-DG, which are smoother and follow the theoretically expected frequency decay (Ida, 1973). Therefore, no artificial Kelvin-Voigt damping has to be applied in ADER-DG, which would further reduce the time step size and increase the computational cost. Our DG method is based on upwind numerical fluxes, which are intrinsically dissipative. In particular, in our high-order DG approach the amount of numerical dissipation increases very steeply as a function of frequency, beyond an effective high-frequency cutoff that depends on the element size (Hesthaven and Warburton, 2008, p.90, Fig. 4.1). Hence, the very short wavelengths that are poorly resolved by the mesh elements are adaptively damped, without perturbing the longer, physically meaningful wavelengths. The temporal discretization by the ADER scheme also introduces dissipation (Dumbser *et al.*, 2006) with a frequency cut-off that scales with the time step  $\Delta t$ . However, because  $\Delta t$  is global and controlled by the smallest

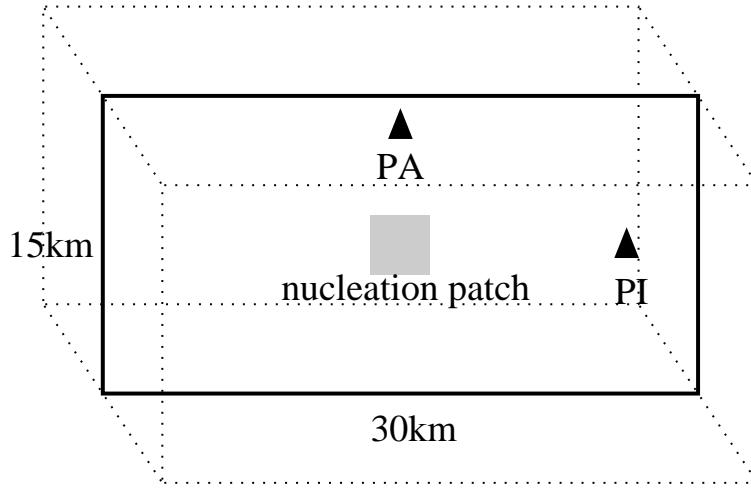


Figure 5.2.: Sketch of the SCEC test case with the nucleation zone (grey shaded). The fault is surrounded by a box with an edge length of 72 km. The black triangles indicate the in-plane receiver (PI) and the anti-plane receiver (PA).

Parameter	Nucleation zone	Outside nucleation zone
Initial shear traction (MPa)	81.6	70.0
Initial normal stress (MPa)	120.0	120.0
Static friction coefficient	0.677	0.677
Dynamic friction coefficient	0.525	0.525
Critical slip distance (m)	0.4	0.4

Table 5.1.: Parameters describing the fault for the SCEC test case.

or most deformed elements, the effect of this dissipation usually appears at much higher frequencies.

The absence of spurious oscillations in ADER-DG enables the observation of interesting details of the solution. For instance, the ADER-DG solution reveals a slope discontinuity of the slip velocity shortly after the peak (at 3.15 s in Fig. 5.3e and at 3.07 s in Fig. 5.3f). This coincides with the time when the slip reaches  $D_c$  and is due to the slope discontinuity in the slip weakening friction law. In the other methods this feature is masked by the spurious oscillations.

### 5.4.2. Convergence test

In section 5.4.1 the good agreement between our ADER-DG method and other numerical methods has been shown. However, since there is no analytical solution available, one cannot determine which numerical method solves the proposed test better. A commonly used technique in computational science to verify the performance of a code is a convergence test. Thereby, we measure the error of the method by the root mean square (RMS) difference of rupture time, peak slip rate and final slip between the finest grid solution

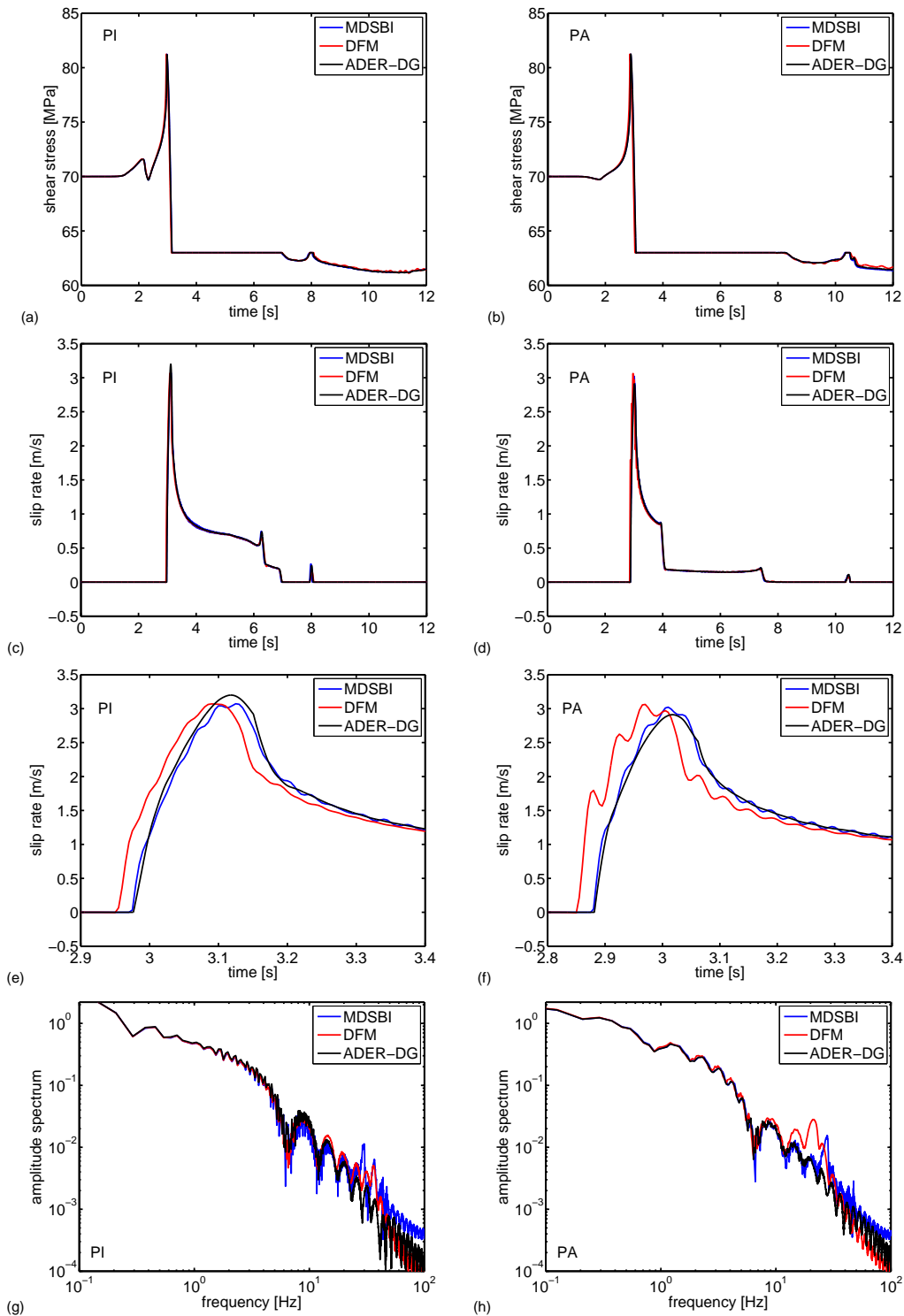


Figure 5.3.: Comparison of solutions for the SCEC TPV3 problem obtained by different methods with comparable grid spacing: the boundary integral method (MDSBI, in blue) with a grid interval of  $h = 50$  m, the FD staggered-grid split node method (DFM, in red) with grid interval  $h = 50$  m, and our ADER-DG scheme (black) with an equivalent mesh spacing of  $\Delta x = 50$  m at the fault. Shown are the shear stresses (a and b) and the slip rates (c and d) at two fault locations indicated as PI (left panels) and PA (right panels) in Fig. 5.2. The panels (e) and (f) provide a focused view of the slip rate peaks. In the bottom row (g),(h) the spectra of the slip are shown. All results are in good agreement. The ADER-DG solution does not produce spurious high-frequency oscillations.

and the solutions for coarser grids. The particular RMS metrics we use in this chapter are taken from Day *et al.* (2005).

We solved the SCEC TPV3 with five different mesh spacings,  $h = 1061, 707, 530, 424$  and  $354$  m, defined as the longest triangular edge length on the fault plane, and four different orders of accuracy ranging from  $\mathcal{O}2$  to  $\mathcal{O}5$ . The resolution of dynamic rupture problems can be quantified by  $N_c$ , the number of elements per median process zone length (here,  $440$  m (Day *et al.*, 2005)). Our meshes correspond to  $N_c = 0.41, 0.62, 0.83, 1.04$  and  $1.24$ , respectively. Some of the coarsest meshes at low orders lead to unphysical results and are ignored ( $h = 707$  and  $1061$  m for  $\mathcal{O}2$  and  $h = 1061$  m for  $\mathcal{O}3$ ). To facilitate comparisons between simulations of different resolution, we designed meshes that are uniform on the fault plane by first generating a regular surface mesh of quadrilateral elements of edge length  $h/\sqrt{2}$ , then dividing each quadrilateral into two triangles. In contrast, the tetrahedral mesh in the bulk is highly unstructured. We used mesh coarsening by increasing the element edge length by 10% per element with increasing distance from the fault, up to a maximum edge length of  $10h$ . The regular meshing of the fault plane does not affect the generality of our results: the accuracy of the simulation presented in Section 5.4.1, executed on a fully unstructured mesh (irregular even on the fault plane), is consistent with the results presented hereafter. Our reference solution was obtained with  $h = 354$  m and  $\mathcal{O}6$ . We sampled the solution with 400 randomly distributed receivers along the fault plane. The rupture time is defined as the first time sample at which the slip rate exceeds 1 mm/s. The 15 receivers located in the nucleation zone are excluded for the rupture time measurement since their rupture time is exactly the first time step.

The results are summarized in Table 5.2 and visualized in Fig. 5.4. The RMS difference in rupture time, final slip and peak slip rate decrease with increasing mesh refinement and increasing order. This implies that a low-order approximation can achieve the accuracy of high-order approximations only when using a much smaller element size. Except for  $\mathcal{O}2$ , the RMS rupture time difference is low (Fig. 5.4a) and all chosen resolutions capture the rupture front evolution reasonably well with respect to the reference solution. The difference between the finest test solution and the reference solution is indeed very small, 0.04% (Table 5.2). The time step size  $\Delta t$ , shown by dashed lines in Fig. 5.4a, is much smaller than the RMS rupture time differences, hence temporal sampling does not bias our measurement of rupture times. The RMS difference of the final slip is also low, around 1% at best (Fig. 5.4b). The RMS difference of peak slip rate is larger (Fig. 5.4c), as usually found for this very sensitive error metrics based on extreme values of a spiky signal. Overall, the error levels are similar to those obtained by methods such as DFM (Day *et al.*, 2005). The ADER-DG solutions achieve numerical convergence with respect to the applied order and element size reduction.

The convergence of the errors as a function of  $h$  is well described by power laws. The small scattering of the error data around their power law regressions (Fig. 5.4) is expected when using structured mesh refinement strategies, like “red-refinement” (split a triangle into four geometrically similar triangles), but is remarkable given our fully unstructured meshes. The smooth convergence to the reference solution confirms the robustness and reliability of the method. The exponent of the power laws, or convergence rate, is given in Table 5.3. The  $\mathcal{O}2$  simulations achieve the highest convergence rates but they also

have the largest errors, as mentioned above. Between  $\mathcal{O}3$  and  $\mathcal{O}5$  the convergence rate saturates. This implies that spectral convergence is not achieved in this problem. In general, the convergence rate of a numerical solution improves when increasing the order of the method only if the exact solution is sufficiently smooth (Godunov, 1959; Krivodonova, 2007; Hesthaven and Warburton, 2008, p.87). Dynamic rupture problems contain non-smooth features. Linear slip weakening friction guarantees continuity of slip velocity and shear stress but slip acceleration remains singular at the leading and trailing edges of the process zone Ida (1973). Moreover, the initial stress conditions and the stopping barriers are not smooth in the TPV3 problem. However, in smoother rupture problems involving rate-and-state friction and smooth initiation conditions improvements of convergence rate with increasing order have not been observed (Rojas *et al.*, 2009), only reduced rupture time errors below the time sampling precision (Kaneko *et al.*, 2008). In Table 5.3 the convergence rates of DFM and of a boundary integral method (from Day *et al.* (2005)) are included for comparison. Whereas the convergence rates of the rupture time agree for the different methods, DFM and BI converge slightly faster than ADER-DG with  $\mathcal{O} > 2$  for the other error metrics, final slip and peak slip rate.

Fig. 5.4d shows the convergence of the rupture time misfit as a function of CPU time, the actual duration of the simulation multiplied by the number of processors involved. The number of processors ranges from 256 to 8192 since the problem size varies so much that the smallest simulation will not run efficiently on the maximum number of processors and the largest problem cannot be solved with fewer processors. Although the scalability of our DG code is in general good, it is still not perfect over this range of number of processors, which affects our measurements of CPU time. From Fig. 5.4d higher order methods are not more efficient for solving the test problem at a given accuracy. For a given  $h$ , high-order methods are more computationally demanding as they store and update more unknowns per element, and this cost is not significantly offset by their improved accuracy. However, the smoothness of the slip rate time series (Section 5.4.1) and the quality of the wave propagation away from the fault are not quantified by the error metrics considered here. Both aspects are an important part of the overall quality and accuracy of the solution. It has been demonstrated that a high-order approximation in a DG scheme is much more efficient for wave propagation problems than a low-order approximation, i.e. it requires lower computational cost to achieve a given error level (Käser *et al.*, 2008). The flexibility of the ADER-DG method allows the resolution to be optimized ( $h$ - and  $p$ -adaptivity) independently for the fault and for the surrounding media based on different criteria, the cohesive zone size and the maximum target frequency, respectively. A high-order approximation is advantageous in strong ground motion simulations based on dynamic rupture scenarios because it provides an accurate wave field at lower cost.

For illustration purposes, we show time series of the shear stresses and slip rates used for the convergence test in Fig. 5.5. The receiver has been picked randomly and is located at along-strike distance of 8525 m and down-dip distance of 6893 m from the center of the nucleation zone. On the left panels, results of all used orders of accuracy  $\mathcal{O}$  are given for a fixed mesh spacing  $h = 354$  m. Note that  $\mathcal{O}6$  is our reference solution. On the right, the order is fixed to  $\mathcal{O}4$  but the mesh spacing varies. Obviously, the  $\mathcal{O}2$  simulation has the largest delay compared to the reference solution, explaining the large errors of the low order runs. Also visible is a significant delay in the simulation with

$h = 1061$  and  $\mathcal{O}4$  (Fig. 5.5 right panels). The differences of all other simulations are only noticeable in the detail views of the rupture front (Fig. 5.5(c), (d), (g) and (h)). No spurious oscillations occur, independent of the mesh spacing and the order of accuracy. Furthermore, no artifacts of the high-order formulation (e.g. over- or undershoots) appear at the discontinuities.

$h$ (m)	$\mathcal{O}$	RMS rupture time (%)	RMS final slip (%)	RMS peak slip rate (%)	CPU time (s)
1061	4	2.79	2.88	14.52	2288640
	5	0.95	2.35	12.58	7280640
707	3	3.05	2.38	13.48	2764800
	4	0.74	1.85	11.39	8386560
	5	0.31	1.42	8.36	26081280
530	2	37.32	54.31	37.98	1474560
	3	1.44	1.61	10.84	4945920
	4	0.43	1.31	8.00	14991360
	5	0.19	1.22	6.87	49827840
424	2	15.34	39.62	25.84	2580480
	3	0.69	1.35	9.18	8847360
	4	0.20	1.20	6.76	29675520
	5	0.08	1.03	6.20	99901440
354	2	9.99	29.74	21.38	3993600
	3	0.44	1.20	7.65	14499840
	4	0.12	0.98	5.95	45772800
	5	0.04	1.03	5.84	163553280

Table 5.2.: Convergence results for the 3D TPV3 SCEC test case.

Method	Rupture time	Final slip	Peak slip rate
ADER-DG $\mathcal{O}2$	3.28	1.48	1.43
ADER-DG $\mathcal{O}3$	2.84	0.99	0.80
ADER-DG $\mathcal{O}4$	2.83	0.97	0.85
ADER-DG $\mathcal{O}5$	2.83	0.75	0.70
DFM <sup>a</sup>	2.96	1.58	1.18
BI <sup>a</sup>	2.74	1.53	1.19

Table 5.3.: Error convergence exponents for ADER-DG schemes of different order. <sup>a</sup>The convergence rates of DFM and BI are from Day *et al.* (2005).

## 5.5. The Landers 1992 Earthquake

To demonstrate the potential of the introduced ADER-DG method on unstructured meshes for simulations of rupture dynamics in complex fault geometries we consider the June 28th 1992  $M_W$ 7.3 Landers, California, earthquake as an example. Our purpose here is not to re-examine the dynamics of this event in detail, as in many previous studies (e.g., Olsen *et al.*, 1997; Aochi and Fukuyama, 2002; Aochi *et al.*, 2003; Fliss *et al.*, 2005), but rather to illustrate the potential of our method for future studies. We hence follow the simplified setup introduced by de la Puente *et al.* (2009) and extend it to three dimensions, including topography.

The Landers earthquake occurred on a 60 km long complex fault system along the western edge of the Eastern California Shear Zone. Its surface rupture involved at least parts of four major right-lateral strike-slip fault segments, breaking successively from south to north the Johnson Valley, Homestead Valley, Emerson and Camp Rock faults (Hauksson *et al.*, 1993). These sub-parallel main segments are curved, overlapping and connected by shorter faults (e.g. the Kickapoo, or Landers fault, connecting the Johnson Valley and Homestead Valley faults). A fault geometry comprising six non-planar fault segments (Fig. 5.6) was adopted from (Aochi and Fukuyama, 2002). Studies based on guided waves (Li *et al.*, 1994) and analysis of the aftershock distribution (Hauksson *et al.*, 1993) show that the surface geometry continues to a depth of at least 10 km. Source inversion results indicate a vertical dip of the fault planes (Wald and Heaton, 1994; Cohee and Beroz, 1994; Cotton and Campillo, 1995). We hence model the three-dimensional fault system geometry by extending the surface fault traces vertically into depth. The fault plane starts below the surface at sea level and extends to 15 km below sea level. Although we do not allow for surface rupture in this tentative test scenario, surface rupture was successfully verified with the current ADER-DG implementation with the SCEC TPV5. This data is freely available from the SCEC website (<http://scecddata.usc.edu/cvws/>).

The model domain is a polygon of lateral extension of 180 km times 220 km and depth of 50 km. Fig. 5.6 shows a map of the model area and its topography. The fault system is enclosed in the south by the San Bernardino mountains, with a maximum elevation of 3505 m, and in the north by smaller dissected mountain ranges.

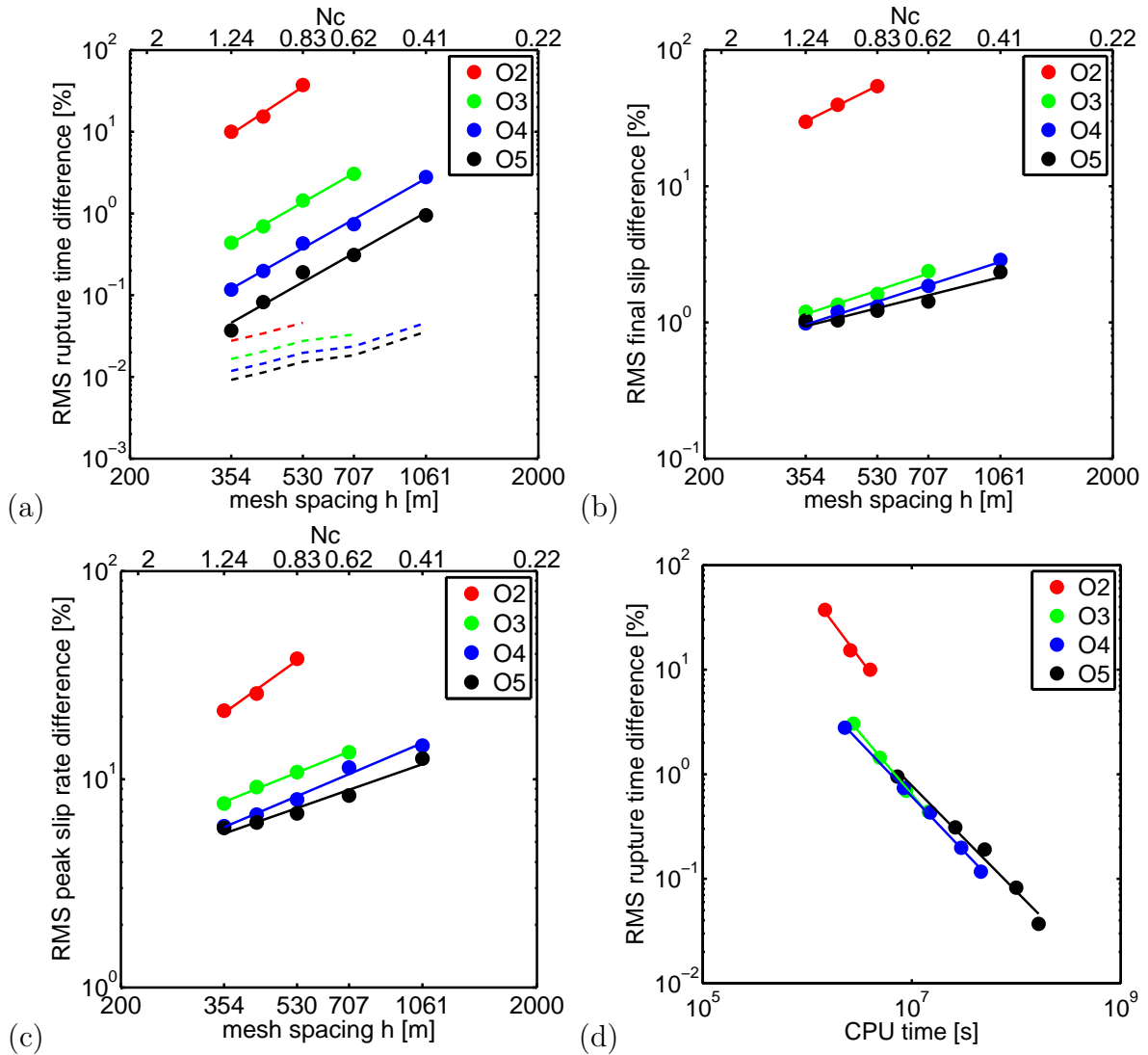


Figure 5.4.: Convergence results for the 3D TPV3 SCEC test case.  $N_c$  is the number of elements per median process zone length. Dots are the simulation results colored by their order of accuracy. The solid lines represent the regression and the dashed lines denote the levels determined by the timestep  $\Delta t$ . Misfits are shown for the rupture time (a), final slip (b), and peak slip rate (c). Panel (d) shows the convergence of the rupture time misfit as a function of its CPU time.

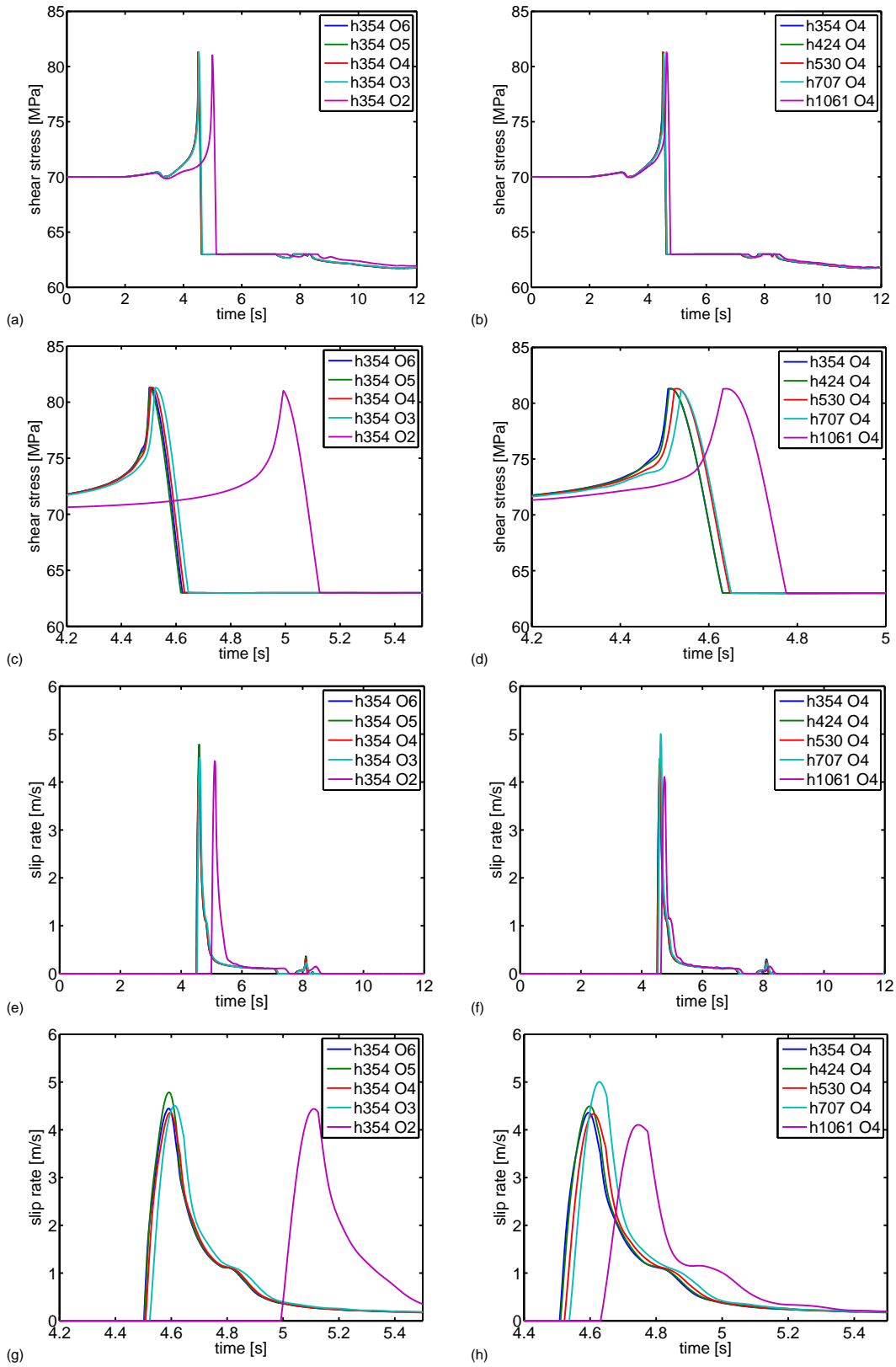


Figure 5.5.: Representative solutions of the SCEC TPV3 problem with ADER-DG of varying grid spacing and order. Shown are time series of shear stress (a and b) and slip rate (e and f) at fault location at a distance of 8525 m along-strike and 6893 m down-dip from the center of the nucleation zone. Panels (c), (d), (g) and (h) show details near the rupture front. The left panels show the results of all used orders of accuracy  $\mathcal{O}$  for a fixed mesh spacing  $h = 354$  m, including the reference solution  $\mathcal{O}6$ . On the right panels, the order is fixed to  $\mathcal{O}4$  but the mesh spacing varies.

Since our purpose is to focus on the rupture process on a geometrically complex fault system, we assume a homogeneous medium ( $v_p = 6200$  m/s,  $v_s = 3520$  m/s and  $\rho = 2700$  kg/m<sup>3</sup>) and a homogeneous initial stress field with horizontal principal stresses  $\sigma_1 = 300$  MPa and  $\sigma_2 = 100$  MPa. The assumed direction of the largest principal stress, N22°E, is representative of the northern part of the rupture in the model of Aochi and Fukuyama (2002) and is indicated by a red double arrow in Figs. 5.6 and 5.8. Although the stress field is homogeneous, the varying fault strike generates a heterogeneous stress state along the fault. The nucleation is initiated by a lower principal stress value of  $\sigma_2 = 70$  MPa in a square patch of edge length 3 km around the hypocenter, located on the southern portion of the Johnson Valley fault. Table 5.4 contains the frictional parameters of the fault. We compute the spontaneous rupture for a total duration of 10 s.

Fig. 5.7 shows the fault discretized by triangles of size  $h = 500$  m (edge length). The horizontal plane below the fault shows the mesh coarsening up to  $h = 2500$  m in the closer neighborhood of the fault. The surface mesh above the fault has  $h = 500$  m to ensure an accurate representation of the topography. This high-resolution area is surrounded by a much coarser mesh consisting mainly of  $h = 5$  km elements, but we allow for  $h = 10$  km at the outer borders of the domain. The fast mesh coarsening does not affect the rupture propagation, it only damps the high-frequency content of the wave field in areas of larger mesh spacing (de la Puente *et al.*, 2009). This allows to concentrate the computational effort on the rupture area, where it is needed. The domain boundaries are located far enough away from the fault to avoid the effect of possible artificial reflections.

The resulting mesh contains 587,585 elements. Using an  $\mathcal{O}5$  approximation this model size is relatively inexpensive and can be computed on a small scale cluster of approximately 100 nodes, which can be currently found in many research institutions. We used the BlueGene/P machine *Shaheen* of the King Abdullah University of Science and Technology, Saudi Arabia. Our 10 s long simulation ran for 20 hours on 512 processors. This relatively large number of processors was conditioned by the low frequency of the BlueGene/P CPUs (850 MHz) and, for standard CPUs, it can be reduced by a factor of 4 to 6. The entire discretization process including topography and fault geometry definition, mesh generation, and boundary specifications took less than two days due to the flexibility and robustness of tetrahedral mesh generation. Hence the manual effort and related cost in terms of expert working hours are kept at a minimum.

Fig. 5.8 shows the amplitude of the particle velocity generated by the earthquake at four different times on a horizontal cross-section of the nucleation area at a depth of 5 km below sea level. Initially, the rupture propagates bilaterally on the Johnson Valley fault (Fig. 5.8a). At time 1.5 s the northern rupture front approaches the first branching point (Fig. 5.8b). It then continues into the Kickapoo fault, without breaking the northern portion of the Johnson Valley fault (Fig. 5.8c). The rupture breaks the complete Kickapoo segment and continues on the Homestead Valley fault where it stops approximately at time 6 s (Fig. 5.8d). This rupture branching to the extensional side is consistent with the 2D study of de la Puente *et al.* (2009) and with theoretical considerations Poliakov *et al.* (2002). While some interesting features of the Landers earthquake rupture, like the backward branching to the southern segment of the Homestead Valley fault (Poliakov *et al.*, 2002; Fliss *et al.*, 2005), are not reproduced by our simulation, it achieves our main intention to conceptually illustrate the capabilities of the 3D ADER-DG method.

Parameter	Nucleation zone	Outside nucleation zone
Principal stress $\sigma_1$ (MPa)	300.0	300.0
Principal stress $\sigma_2$ (MPa)	70.0	100.0
Static friction coefficient	0.6	0.6
Dynamic friction coefficient	0.4	0.4
Critical slip distance (m)	0.8	0.8

Table 5.4.: Frictional parameters for the test case of the Landers fault system.

Fig. 5.9 shows the surface wave field developing with time from 2.5 s to 4.5 s. There is a clear directivity effect: most of the energy is traveling northwards, like the rupture front. From visual inspection, the topography seems to increase the complexity of the wave field. However, we expect stronger site effects when incorporating a more realistic geological model with low velocity layers in the valley and stiffer material in the mountains.

## 5.6. Conclusions

We successfully incorporated 3D earthquake rupture dynamics in the ADER-DG scheme by modifying the Riemann problem according to the Coulomb friction model. Although we considered here linear slip weakening friction, the method allows for the implementation of more advanced friction laws, e.g. rate-and-state friction. Accuracy was verified by comparing results of the SCEC TPV3 benchmark problem for spontaneous rupture to well established methods. The ADER-DG solution is notably free of spurious high-frequency oscillations, most likely owing to the high-order frequency dependence of the intrinsic dissipation of the DG method. Hence, no further artificial viscous damping mechanism has to be applied which could potentially affect the rupture process. The robustness and systematic correctness of the ADER-DG method was proved by a convergence test, which showed that mesh refinement or increasing the order leads to smaller errors.

An example of dynamic rupture simulation on a complex fault system, inspired by the surface rupture geometry of the Landers earthquake, demonstrates the great benefits of the proposed method based on unstructured tetrahedral meshes that can be aligned into merging faults under shallow angles. Areas of interest, here the topography and the fault, can be modeled adequately by small elements while mesh coarsening can be applied elsewhere to reduce the computational cost. This is of interest in particular for dynamic rupture studies which require a fine sampling of the fault in order to capture the cohesive zone for a correct simulation of the rupture process while adapting the resolution to the dispersion requirements of wave propagation at lower frequencies far from the fault. We do not observe any artificial reflection due to mesh coarsening in ADER-DG. In methods based on structured grids the mesh refinement is instead applied uniformly in the entire computational domain, propagating frequencies much higher than required for strong ground motion investigations, or through grid-doubling techniques, which could generate artificial reflections.

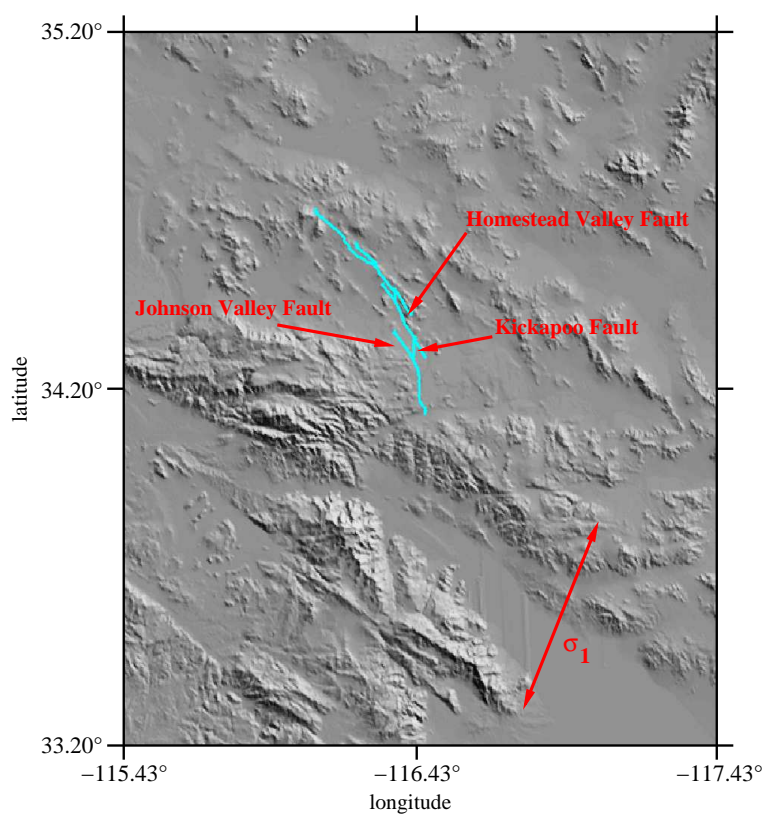


Figure 5.6.: Map view of the 1992 Landers earthquake fault system with topography. The red double arrow indicates the assumed principal stress direction of N22°E. The lateral center of the model domain is the location of the epicenter at 34.20°N and 116.43°W.

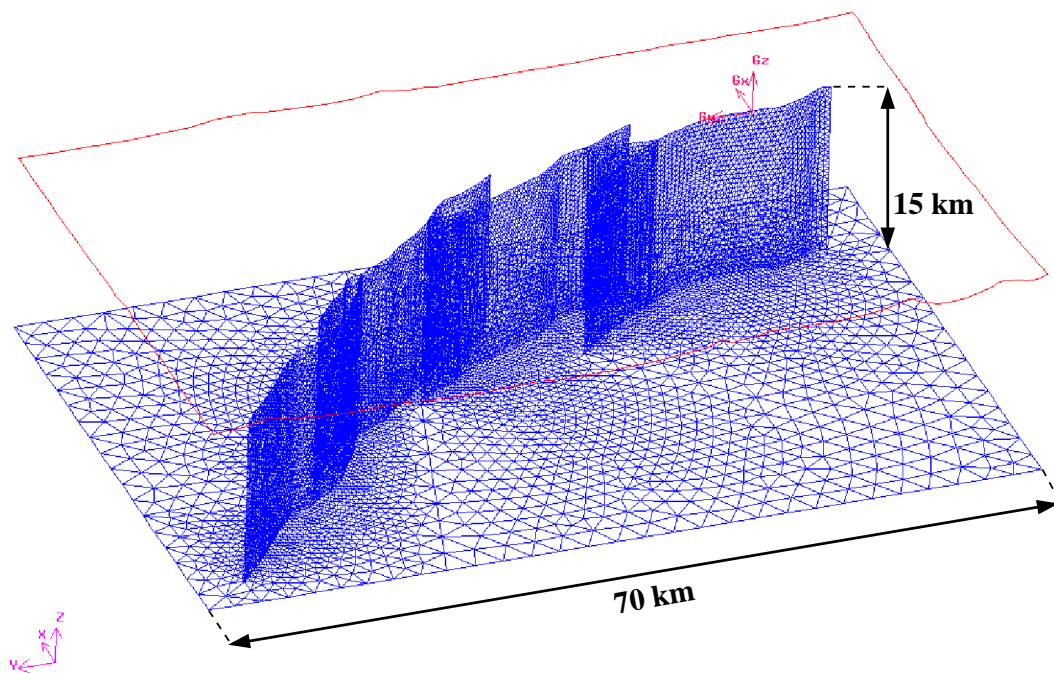


Figure 5.7.: Discretization of the Landers fault system with triangles of 500 m edge length. In the area indicated by a red line the topography is described by a fine mesh of 500 m edge length. The box below is filled by 2500 m elements with only moderate mesh coarsening away from the fault.

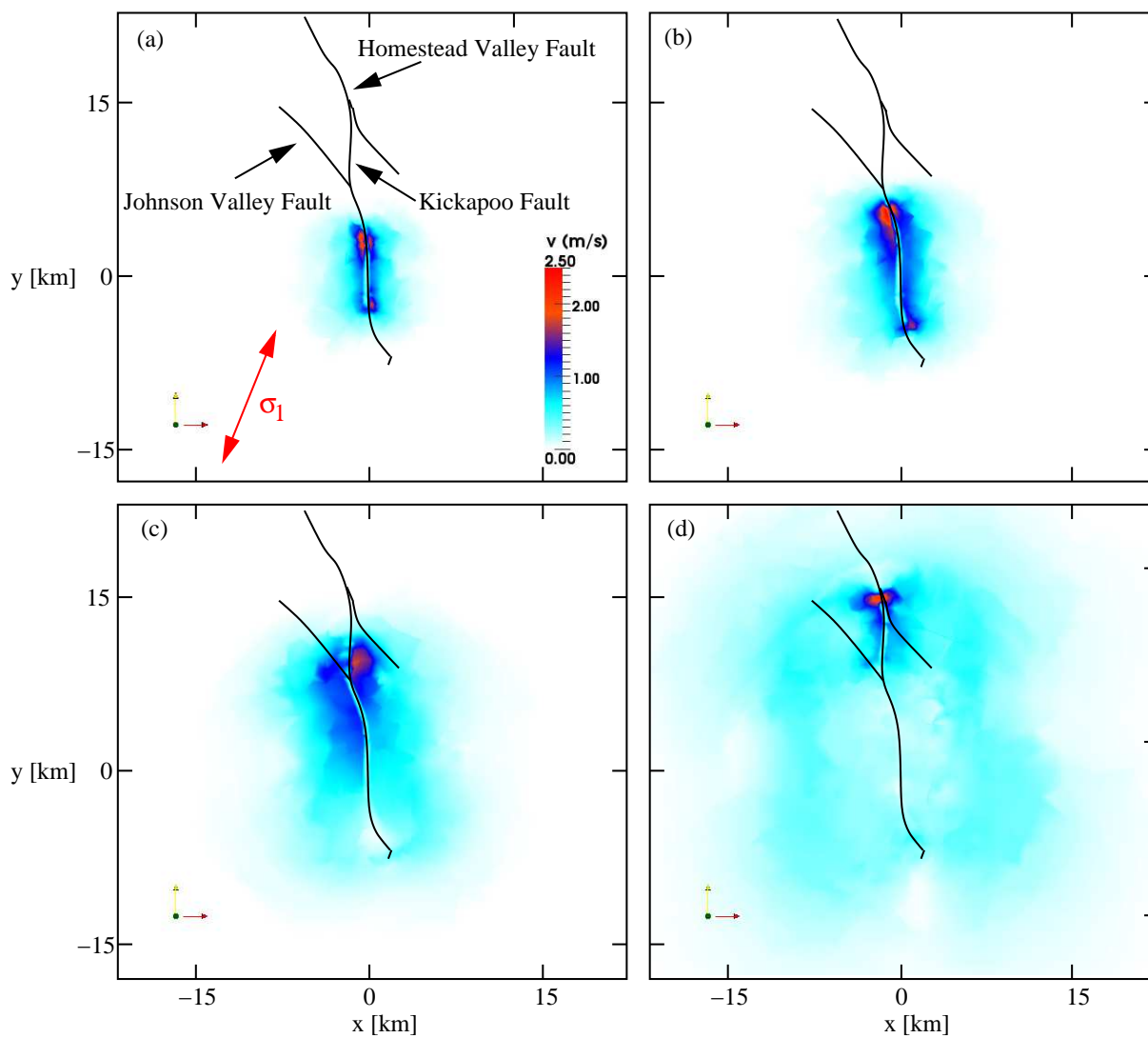


Figure 5.8.: Snapshots of absolute particle velocity at (a) 1, (b) 1.5, (c) 2.5, (d) 4.5 s after rupture initiation on a horizontal cut of the nucleation area at a depth of 5 km below sea level. The red double arrow indicates the assumed principal stress direction.

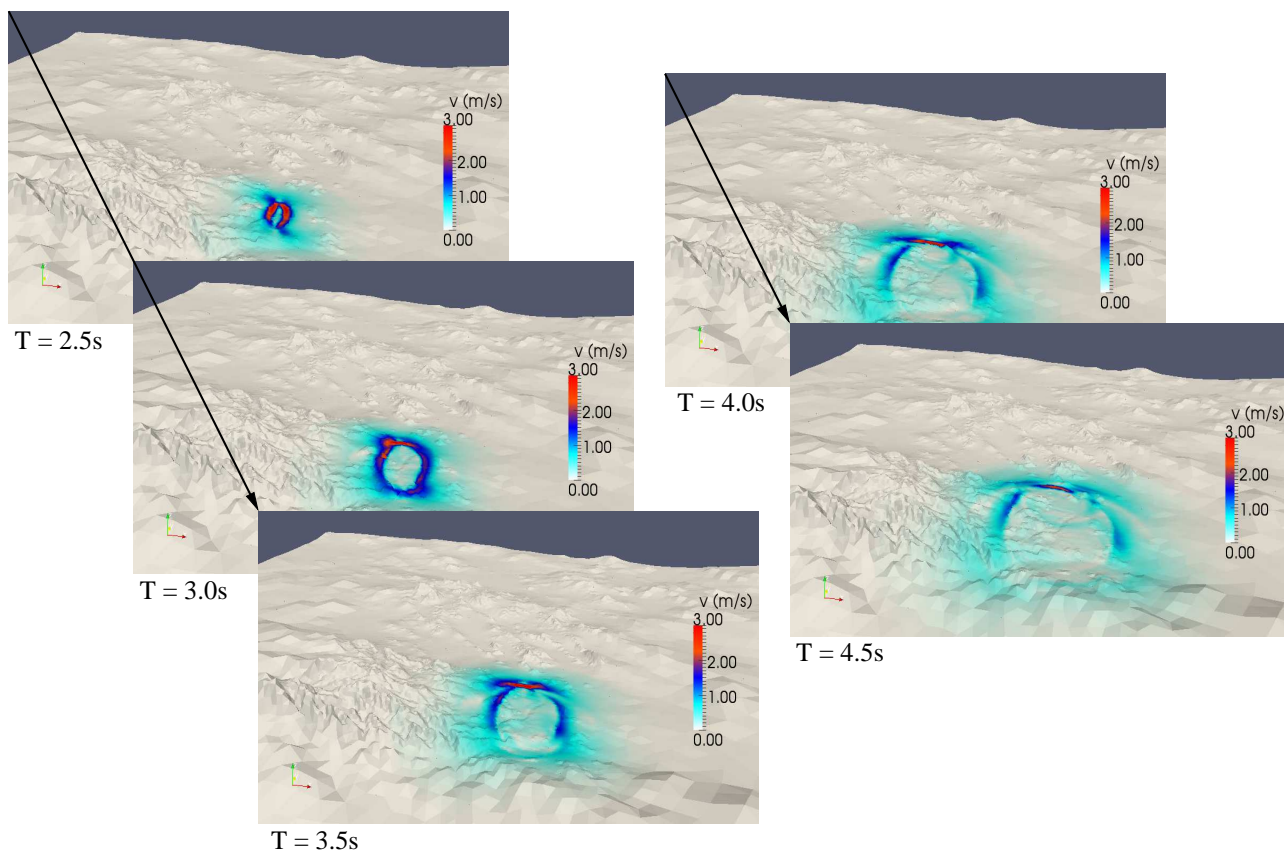


Figure 5.9.: Development of the ground velocity field with time. The topography is scaled by a factor of 3.  $v$  represents the absolute particle velocity in  $\text{m/s}$ . The viewing direction is roughly from southeast to northwest. The directivity effect can be clearly observed.

---

We conclude that the combination of meshing flexibility and high-order accuracy of the ADER-DG method will make it a very useful tool to study earthquake dynamics on complex fault systems. Future steps in the development include the incorporation of bimaterial fault interfaces, more realistic friction laws and non linear bulk rheologies.



# Chapter 6.

## Conclusion

In this work we applied, analyzed and further developed the software SeisSol based on the ADER-DG method. SeisSol is a numerical forward solver for linear hyperbolic partial differential equations. The scheme enables the use of fully unstructured tetrahedral meshes while keeping high-order accuracy. It is designed to model seismic waves in complex and heterogeneous media. We introduced the mathematical formulation in Chapter 2 including a complete discretization of the elastic wave equations.

The advantages of the framework are demonstrated in Chapter 3 with an emphasis on industry applications. In the first application of a sonic logging experiment, the challenge was that small scale features (borehole well, tool) had to be respected by the mesh, although the surrounding material properties would allow for large element sizes. Without *hp*-adaptivity and local time stepping the problem would have not been computational feasible. In the second example of a complicated salt dome model, the enhanced meshing flexibility due to the use of tetrahedra pays off. After the geometry is defined, the elements can be easily adjusted and aligned to the geological material interfaces. In spite of the method's flexibility required by the complex models, it was shown that the method performs excellent on various HPC-infrastructures.

The importance of aligning elements to material interfaces was discussed in Chapter 4. In general, methods implemented on regular grids are computationally very efficient compared to methods with unstructured grid approaches. However, regular grids can result in artificial staircase approximations of material interfaces. The scope of our study was to analyze how fine the regular grid spacing must be in order to produce comparably accurate seismograms as obtained by the mesh aligned version using an irregular grid. We found a strong dependence on mesh spacing, material contrast and signal frequency. In fact, the misfits increase with a decreasing number of elements per wavelength and with increasing material contrast. A systematic parameter study enabled us to define rules that should be adhered to ensure accurate synthetic data, if regular meshing is applied. For the tested geometry, a discretization of 5 elements per shortest dominant wavelength generates acceptable seismograms up to a material contrast of 0.5 in the sense of the S-wave speed ratio. This resolution could be reduced for weaker material contrasts. However, in the case of stronger material contrasts a significant grid refinement is necessary to avoid numerical artifacts. In particular, for a free-surface boundary or an acoustic-elastic coupling the mesh should be aligned to the interface since we were not able to produce reliable data within the range of tested frequencies and mesh spacings with a staircase approximation of such boundaries. Finally, the proposed rules have been tested in two realistic scenarios.

In both cases an expected minor misfit was obtained. The study supports particularly high-order methods, like SEM and DG, implemented on structured meshes as the rules help to choose mesh resolutions that generate reliable seismograms while minimizing the computational cost. Nevertheless, in consideration of the results we highly recommend the use of aligned meshes for topography and solid-fluid interfaces.

In the introduction we proclaimed the extension of the ADER-DG method to three-dimensional spontaneous rupture problems on complex fault shapes as the main goal of this work. For this purpose, we follow the study of de la Puente *et al.* (2009) and employ numerical fluxes to incorporate the rupture dynamics. This is object in Chapter 5, where the mathematical algorithm is described first. The superior accuracy of the concept was shown by comparison with two well established numerical methods. ADER-DG reproduces the rupture process correctly. Neither problems at discontinuities occur nor spurious high-frequency oscillations are observed. Discontinuities in the solution could have been an issue due to Godunov's theorem that predicts over- and undershoots using high-order formulations. Furthermore, Godunov's theorem states that no high-order convergence can be expected in such cases. Indeed, although integrating the equations with high-order accuracy in space and in time, ADER-DG did not reach better convergence rates while improving the approximation. However, the quality of the obtained seismograms enhances significantly by increasing the order of accuracy following well described power laws that determine the correctness of the new implementation. Moreover, the ADER-DG solution is notably free of non-physical high-frequency oscillations, which have been observed in all other numerical approaches until now. Hence, no artificial viscous damping mechanism has to be applied in the ADER-DG framework which could potentially affect the rupture process. Reason for both addressed issues is most likely the intrinsic dissipation of the upwinding flux damping non-physical high-frequency oscillations caused by the dynamic rupture source that is somehow artificially imposed on the system.

Finally, the benefits for strong ground motion modeling have been demonstrated for an earthquake scenario based on the Landers fault system. In this example, we tested our dynamic rupture implementation on unstructured meshes on a complex fault system that includes curved faults and fault branches. The flexibility of the tetrahedral elements makes it possible to align small elements into merging faults under shallow angles. Areas of interest, here the topography and the fault, have been modeled adequately by small elements while mesh coarsening was applied where the dispersion requirements of the wave propagation allowed for it. This way, the computational cost could be reduced significantly. The ability of local mesh refinement is in particular advantageous for dynamic rupture modeling as the cohesive zone requires a dense spatial sampling for a correct rupture front evolution while the interesting frequencies for ground motion analysis are rather low and can be resolved with much larger elements. Unstructured meshes represent the most elegant way to adapt spatially the resolution while avoiding any numerical artifacts that occur e.g. in grid doubling techniques. Furthermore, to our knowledge it was the first fully dynamic rupture simulation that includes such a complex fault system and topography. To conclude, we are convinced that the ADER-DG method on unstructured meshes including the physical correct representation of the spontaneous rupture process will be the tool of choice for realistic strong ground motion simulation in the future. Therewith, the main goal of this project was accomplished successfully.

However, the method has to be extended further in many ways to incorporate all features of a modern strong ground motion simulator. First of all, the method's correctness must be proved and its accuracy quantified for curved and kinked faults which is not a trivial task as there exists no analytical solution for these kinds of problems. Probably, the verification process will include comparisons to other methods and to solutions obtained by semi-analytical estimations. Although we have strong evidence the intrinsic dissipation of the numerical flux is the reason for the absence of spurious oscillations, the mathematical proof in form of a dispersion analysis is still outstanding. Such a dispersion analysis could also provide helpful insights to improve other numerical methods. Another future task could be the incorporation of more advanced friction laws as rate-and-state and non linear bulk rheologies. Hereby, plasticity and material damage are of particular interest which would lead to a more realistic representation of fault branches where extremely high strain rates can be observed and the purely elastic approach might not be valid anymore. Furthermore, the current earthquake source implementation should be combined with computational time reducing features like local time stepping and mortar element concepts that are already successfully tested and applied for the ADER-DG scheme. This is important as the ADER-DG algorithm is in general computationally expensive compared to other numerical methods. At this point, we note that the efficient installation of high-order DG methods on unstructured meshes on parallel HPC architectures is still ongoing research in computational science and applied mathematics. One crucial problem is an observed high rate of cache misses as the character of the unstructured mesh has direct influence on the memory management whose complexity increases dramatically by that. Furthermore, an optimal way to treat the tremendous number of small sparse matrix-matrix multiplication has not been found yet. Although the topic seems to be challenging, we expect large improvements for the optimization in the near future since a clear trend to unstructured meshes and high-order accurate methods can be identified in many disciplines within the natural sciences leading to a high motivation for further investigations.

Besides the lack of certain features, the framework is already feasible to answer a range of scientific questions in many aspects of earthquake source physics. For instance, extremely sensitive but interesting details of the friction law can be observed in the produced results, e.g. the slope discontinuity in the slip rate time series when the slip reaches  $D_c$  of the linear slip weakening friction law (see Section 5.4.1). A future implementation of rate-and-state friction laws would enable confident research on various physical parameters of the frictional sliding. Furthermore, the influence of bimaterial faults on the rupture evolution and the ground motion can be studied on a new level of accuracy due to the absence of spurious oscillations. First convergence tests under Prakash-Clifton regularization appear promising. Investigations in low-velocity fault zone structures will also benefit from the current methodology. Hereby, the elements can be easily aligned to the geometrical shape of so-called flower structures that typically embed active faults while the method allows for surface rupture at the same time. First studies have shown interesting results such as naturally created pulse-like ruptures. The pulse-like ruptures are here generated by transient waves reflected by the low-velocity fault zone and bulk material contrast. These reflected waves stop the primal crack-like rupture due to a change of the stress conditions on the fault. Moreover, a splitting of the pulse-like rupture front into

two could be observed near the free surface. This all represent interesting possibilities and starting points for further research of dynamic rupture.

# Bibliography

**Aagaard, B., Heaton, T., and Hall, J.** (2001). Dynamic earthquake rupture in the presence of lithostatic normal stresses: Implications for friction models and heat production. *Bull. Seism. Soc. Am.*, **91**, 1765–1796.

Referenced in: 2.1, 5.1

**Aki, K. and Richards, P.** (2002). *Quantitative Seismology*. University Science Books, Sausalito, California.

Referenced in: 2.2

**Ampuero, J.-P.** (2002). *Etude physique et numérique de la nucléation des séismes*. Dissertation, Université Paris 7, Denis Diderot.

Referenced in: 5.1

**Anderson, J. G.** (2004). Quantitative measure of the goodness-of-fit of synthetic seismograms. *13th World Conf. on Earthquake Engineering Conference Proc.*, (paper 243).

Referenced in: 4.3.2

**Andrews, D.** (1973). A numerical study of tectonic stress release by underground explosions. *Bull. Seism. Soc. Am.*, **63**, 1375–1391.

Referenced in: 1, 5.1, 5.3

**Andrews, D.** (1976a). Rupture propagation with finite stress in antiplane strain. *J. Geophys. Res.*, **81**, 3575–3582.

Referenced in: 5.2

**Andrews, D.** (1976b). Rupture velocity of plane-strain shear cracks. *J. Geophys. Res.*, **81**, 5679–5687.

Referenced in: 5.2

**Andrews, D.** (1985). Dynamic plane-strain shear rupture with a slip-weakening friction law calculated by a boundary integral method. *Bull. Seism. Soc. Am.*, **75**, 1–21.

Referenced in: 5.1

**Andrews, D.** (1999). Test of two methods for faulting in finite-difference calculations. *Bull. Seism. Soc. Am.*, **89**, 931–937.

Referenced in: 5.1, 5.3

**Aochi, H. and Fukuyama, E.** (2002). Three-dimensional nonplanar simulation of the 1992 Landers earthquake. *J. Geophys. Res.*, **107**, B22035.

Referenced in: 5.5

- Aochi, H., Madariaga, R., and Fukuyama, E.** (2003). Constraint of fault parameters inferred from nonplanar fault modeling. *Geochem. Geophys. Geosyst.*, **4**(2), 1020.  
Referenced in: 5.5
- Atkins, H. and Shu, C.** (1998). Quadrature-free implementation of the discontinuous Galerkin method for hyperbolic equations. *AIAA Journal*, **36**, 775–782.  
Referenced in: 2.3.4
- Bao, H., Bielak, J., Ghattas, O., Kallivokas, L. F., O’Hallaron, D. R., Shewchuk, J. R., and Xu, J.** (1998). Large-scale simulation of elastic wave propagation in heterogeneous media on parallel computers. *Computer Methods in Applied Mechanics and Engineering*, **152**(1-2), 85 – 102. Containing papers presented at the Symposium on Advances in Computational Mechanics.  
Referenced in: 2.1, 4.1
- Benjema, M., Glinsky-Olivier, N., Cruz-Atienza, V., Virieux, J., and Piperno, S.** (2007). Dynamic non-planar crack rupture by a finite volume method. *Geophys. J. Int.*, **171**, 271–285.  
Referenced in: 2.1, 5.1
- Benjema, M., Glinsky-Olivier, N., Cruz-Atienza, V., and Virieux, J.** (2009). 3-D dynamic rupture simulations by a finite volume method. *Geophys. J. Int.*, **178**, 541–560.  
Referenced in: 2.1, 5.1
- Bizzarri, A., Cocco, M., Andrews, D. J., and Boschi, E.** (2001). Solving the dynamic rupture problem with different numerical approaches and constitutive laws. *Geophys. J. Int.*, **144**, 656–678.  
Referenced in: 1
- Bohlen, T. and Saenger, E.** (2006). Accuracy of heterogeneous staggered-grid finite-difference modeling of rayleigh waves. *Geophysics*, **71**(4), 109–115.  
Referenced in: 2.1, 4.1, 4.2.3
- Brietzke, G. B., Cochard, A., and Igel, H.** (2009). Importance of bimaterial interfaces for earthquake dynamics and strong ground motion. *Geophysical Journal International*, **178**(2), 921–938.  
Referenced in: 1
- Burridge, R. and Knopoff, L.** (1967). Model and theoretical seismicity. *Bull. Seism. Soc. Am.*, **57**, 341–371.  
Referenced in: 1
- Butcher, J.** (1987). *The Numerical Analysis of Ordinary Differential Equations: Runge-Kutta and General Linear Methods*. John Wiley & Sons, New York.  
Referenced in: 2.3.4

- Carcione, J.** (1994). The wave equation in generalised coordinates. *Geophysics*, **59**, 1911–1919.  
Referenced in: 2.1
- Castro, C. E., Käser, M., and Brietzke, G. B.** (2010). Seismic waves in heterogeneous material: subcell resolution of the discontinuous galerkin method. *Geophys. J. Int.*, **182**, 250–264.  
Referenced in: 2.3, 4.2.1
- Chaljub, E., Komatitsch, D., Vilotte, J.-P., Capdeville, Y., Valette, B., and Festa, G.** (2007). Spectral-Element Analysis in Seismology, In *Advances in Wave Propagation in Heterogeneous Earth*. *Advances in Geophysics*, **48**, 365–419.  
Referenced in: 2.1
- Chaljub, E., Bard, P., Tsuno, S., Kristek, J., Moczo, P., Franek, P., Hollender, F., Manakou, M., Raptakis, D., and Ptilakis, K.** (2009). Assessing the capability of numerical methods to predict earthquake ground motion: the euroseistest verification and validation project. *Eos Trans. AGU*.  
Referenced in: 4.4, 4.4.1
- Chaljub, E., Moczo, P., Tsuno, S., Bard, P.-Y., Kristek, J., Käser, M., Stupazzini, M., and Kristekova, M.** (2010). Quantitative comparison of four numerical predictions of 3D ground motion in the grenoble valley, france. *Bull. Seis. Soc. Am.*, **100**(4), 1427–1455.  
Referenced in: 2, 4.2.1
- Cochard, A. and Madariaga, R.** (1994). Dynamic faulting under rate-dependent friction. *Pure and Applied Geophysics*, **105**, 25891–25907.  
Referenced in: 5.1, 5.3.2
- Cockburn, B., Karniadakis, G., and Shu, C.** (2000). *Discontinuous Galerkin Methods, Lecture Notes in Computational Science and Engineering*. LNC-SE 11, Springer, Berlin, Germany.  
Referenced in: 2.3.1, 3.2, A
- Cohee, B. P. and Beroz, G. C.** (1994). Slip distribution of the 1992 Landers earthquake and its implications for earthquake source mechanics. *Bull. Seis. Soc. Am.*, **84**(3), 692–712.  
Referenced in: 5.5
- Collino, F., Joly, P., and Millot, F.** (1997). Fictitious domain method for unsteady problems. *J. Comput. Phys.*, **138**(2), 907–938.  
Referenced in: 4.1
- Cotton, F. and Campillo, M.** (1995). Frequency domain inversion of strong motions: Application to the 1992 Landers earthquake. *J. Geophys. Res.*, **100**, 3961–3975.  
Referenced in: 5.5

- Courant, R., Friedrichs, K., and Lewy, H.** (1928). Über die partiellen Differenzialgleichungen der mathematischen Physik. *Mathematische Annalen*, **100**, 32–74.  
**Referenced in:** 2.1, 2.3.4
- Dalguer, L. and Day, S.** (2007). Staggered-grid split-node method for spontaneous rupture simulation. *J. Geophys. Res.*, **112**, B02302.  
**Referenced in:** 5.1
- Dalguer, L. A., Irikura, K., Riera, J. D., and Chiu, H. C.** (2001). The Importance of the Dynamic Source Effects on Strong Ground Motion during the 1999 Chi-Chi, Taiwan, Earthquake: Brief Interpretation of the Damage Distribution on Buildings. *Bull. Seism. Soc. Am.*, **91**(5), 1112–1127.  
**Referenced in:** 1
- Das, S.** (1980). A numerical method for determination of source time functions for general three-dimensional rupture propagation. *Geophys. J. Roy. Astr. Soc.*, **62**, 591–604.  
**Referenced in:** 5.1
- Day, S.** (1982). Three-dimensional finite-difference simulation of fault dynamics: rectangular faults with fixed rupture velocity. *Bull. Seism. Soc. Am.*, **72**, 705–727.  
**Referenced in:** 5.1, 5.3
- Day, S. and Ely, G.** (2002). Effect of a shallow weak zone on fault rupture: numerical simulation of scale-model experiments. *Bull. Seism. Soc. Am.*, **92**(8), 3022–3041.  
**Referenced in:** 5.4.1
- Day, S., Dalguer, L., Lapusta, N., and Liu, Y.** (2005). Comparison of finite difference and boundary integral solutions to three-dimensional spontaneous rupture. *J. Geophys. Res.*, **110**, B12307.  
**Referenced in:** 5.1, 5.2, 5.4.1, 5.4.2, 5.3
- de la Puente, J.** (2008). *Seismic Wave Propagation for Complex Rheologies*. VDM Verlag, Dr. Müller, Saarbrücken, Germany.  
**Referenced in:** 2, 2.2, 3.2
- de la Puente, J., Käser, M., Dumbser, M., and Igel, H.** (2007). An arbitrary high order discontinuous Galerkin method for elastic waves on unstructured meshes IV: Anisotropy. *Geophys. J. Int.*, **169**(3), 1210–1228.  
**Referenced in:** 2.2, 3.2
- de la Puente, J., Dumbser, M., Käser, M., and Igel, H.** (2008). Discontinuous Galerkin methods for wave propagation in poroelastic media. *Geophysics*, **73**(5), T77–T97.  
**Referenced in:** 2.2, 3.2
- de la Puente, J., Ampuero, J.-P., and Käser, M.** (2009). Dynamic rupture modeling on unstructured meshes using a discontinuous Galerkin method. *J. Geophys. Res.*, **114**, B10302.  
**Referenced in:** 1, 2.1, 5, 5.1, 5.3, 5.3.2, 5.5, 6

- DeDontney, N., Rice, J. R., and Dmowska, R.** (2011a). Influence of material contrast on fault branching behavior. *Geophys. Res. Lett.*, **38**(14), 1–5.  
**Referenced in:** 1
- DeDontney, N., Templeton-Barrett, E. L., Rice, J. R., and Dmowska, R.** (2011b). Influence of plastic deformation on bimaterial fault rupture directivity. *J. Geophys. Res.*, **116**(B10), 1–12.  
**Referenced in:** 1
- Dieterich, J. H.** (1979). Modeling of Rock Friction 1. Experimental Results and Constitutive Equations. *J. Geophys. Res.*, **84**(B5), 2161–2168.  
**Referenced in:** 5.2
- Dumbser, M.** (2005). *Arbitrary High Order Schemes for the Solution of Hyperbolic Conservation Laws in Complex Domains*. Dissertation, Universität Stuttgart, Institut für Aerodynamik und Gasdynamik.  
**Referenced in:** 2.3.4
- Dumbser, M. and Käser, M.** (2006). An arbitrary high order discontinuous Galerkin method for elastic waves on unstructured meshes II: The three-dimensional case. *Geophys. J. Int.*, **167**(1), 319–336.  
**Referenced in:** 2, 2.3.4, 3.2, 4.2.1, 5.1, 5.3, 5.3.1, B
- Dumbser, M. and Munz, C.** (2005a). ADER discontinuous Galerkin schemes for aeroacoustics. *Comptes Rendus Mécanique*, **333**, 683–687.  
**Referenced in:** 2.1, 2.3.4
- Dumbser, M. and Munz, C.** (2005b). Arbitrary high order discontinuous Galerkin schemes. In S. Cordier, T. Goudon, M. Gutnic, and E. Sonnendrucker, *Numerical Methods for Hyperbolic and Kinetic Problems*, IRMA series in mathematics and theoretical physics, 295–333. EMS Publishing House.  
**Referenced in:** 2.1, 2.3.4
- Dumbser, M., Schwartzkopff, T., and Munz, C.-D.** (2006). Arbitrary High Order Finite Volume Schemes for Linear Wave Propagation. In E. Krause, Y. Shokin, M. Resch, and N. S. (editors), *Computational Science and High Performance Computing II*, Notes on Numerical Fluid Mechanics and Multidisciplinary Design (NNFM), 129–144. Springer Verlag Berlin / Heidelberg.  
**Referenced in:** 5.1, 5.3.1, 5.4.1
- Dumbser, M., Käser, M., and Toro, E.** (2007). An arbitrary high order discontinuous Galerkin method for elastic waves on unstructured meshes V: Local time stepping and p-adaptivity. *Geophys. J. Int.*, **171**(2), 695–717.  
**Referenced in:** 2, 2.1, 2.3.4, 4.1
- Dunham, E. M., Belanger, D., Cong, L., and Kozdon, J. E.** (2011). Earthquake Ruptures with Strongly Rate-Weakening Friction and Off-Fault Plasticity, Part 2: Non-planar Faults. *Bull. Seism. Soc. Am.*, **101**(5), 2308–2322.  
**Referenced in:** 1

- Ely, G. P., Day, S. M., and Minster, J.-B.** (2008). A support-operator method for viscoelastic wave modelling in 3-d heterogeneous media. *Geophysical Journal International*, **172**(1), 331–344.  
**Referenced in:** 2.1
- Engquist, B. and Majda, A.** (1979). Radiation boundary conditions for acoustic and elastic wave calculations. *Comm. Pure App. Math.*, **32**, 313–357.  
**Referenced in:** 2.5.2
- Etienne, V., Virieux, J., and Operto, S.** (2009). A massively parallel time-domain discontinuous galerkin method for 3D elastic wave modeling. *SEG Meeting Houston*.  
**Referenced in:** 1, 4.1
- Fehler, M.** (2009). Seam phase I, progress report: Numerical simulation verification. *The Leading Edge*, **28**(3), 270–271.  
**Referenced in:** 3.1
- Festa, G. and Vilotte, J.-P.** (2005). The Newmark scheme as velocity-stress time-staggering: an efficient PML implementation for spectral element simulations of elastodynamics. *Geophysical Journal International*, **161**(3), 789–812.  
**Referenced in:** 5.1
- Festa, G. and Vilotte, J.-P.** (2006). Influence of the rupture initiation on the intersonic transition: Crack-like versus pulse-like modes. *Geophysical Research Letters*, **33**(15), 1–5.  
**Referenced in:** 5.1
- Fliss, S., Bhat, H., Dmowska, R., and Rice, J.** (2005). Fault branching and rupture directivity. *J. Geophys. Res.*, **110**, B06312.  
**Referenced in:** 5.5
- Galis, M., Moczo, P., and Kristek, J.** (2008). A 3-D hybrid finite-difference-finite-element viscoelastic modelling of seismic wave motion. *Geophys. J. Int.*, **175**, 153–184.  
**Referenced in:** 2.1, 5.1
- Galis, M., Moczo, P., Kristek, J., and Kristekova, M.** (2010). An adaptive smoothing algorithm in the TSN modeling of rupture propagation with the linear slip-weakening friction law. *Geophys. J. Int.*, **180**, 418–432.  
**Referenced in:** 5.1
- Gallovic, F., Käser, M., Burjanek, J., and Papaioannou, C.** (2010). Three-dimensional modeling of near-fault ground motions with nonplanar rupture models and topography: Case of the 2004 parkfield earthquake. *J. Geophys. Res.*, **115**, B03308.  
**Referenced in:** 2
- Galvez, P., Ampuero, J.-P., Dalguer, L., and Nissen-Meyer, T.** (2011). Dynamic rupture modelling of the 2011 M9 Tohoku earthquake with unstructured 3D spectral element method. *U51B-0043*, Fall Meet. Suppl., Abstract S24.  
**Referenced in:** 5.1

- Gao, H. and Zhang, J.** (2006). Parallel 3-D simulation of seismic wave propagation in heterogeneous anisotropic media: a grid method approach. *Geophys. J. Int.*, **165**, 875–888.  
Referenced in: 4.1
- Geubelle, P. and Rice, J.** (1995). A spectral method for three-dimensional elastodynamic fracture problems. *J. Mech. Phys. Solids*, **43**, 1791–1824.  
Referenced in: 5.1, 5.3.2, 5.4.1
- Givoli, D. and Keller, J. B.** (1990). Non-reflecting boundary conditions for elastic waves. *Wave Motion*, **12**(3), 261 – 279.  
Referenced in: 2.5.2
- Givoli, D., Hagstrom, T., and Patlashenko, I.** (2006). Finite element formulation with high-order absorbing boundary conditions for time-dependent waves. *Computer Methods in Applied Mechanics and Engineering*, **195**(29-32), 3666 – 3690.  
Referenced in: 2.5.2
- Godinho, L., Mendes, P. A., Tadeu, A., Cadena-Isaza, A., Smerzini, C., Sanchez-Sesma, F. J., Madec, R., and Komatitsch, D.** (2009). Numerical simulation of ground rotations along 2D topographical profiles under the incidence of elastic plane waves. *Bull. Seism. Soc. Am.*, **99**(2B), 1147–1161.  
Referenced in: 4.2.1
- Godunov, S.** (1959). A finite difference method for the computation of discontinuous solutions of the equations of fluid dynamics. *Mat. Sb.*, **47**, 271–306.  
Referenced in: 5.4.2
- Graves, R.** (1996). Simulating seismic wave propagation in 3D elastic media using staggered-grid finite differences. *Bull. Seis. Soc. Am.*, **86**(4), 1091–1106.  
Referenced in: 4.1
- Gustafsson, B. and Wahlund, P.** (2004). Time compact difference methods for wave propagation in discontinuous media. *SIAM J. Sci. Comput.*, **26**(1), 272–293.  
Referenced in: 2.1, 4.1
- Harris, R., Barall, M., Archuleta, R., Aagaard, B., Ampuero, J.-P., Bhat, H., Cruz-Atienza, V., Dalguer, L., Dawson, P., Day, S., Duan, B., Dunham, E., Ely, G., Kaneko, Y., Kase, Y., Lapusta, N., Liu, Y., Ma, S., Oglesby, D., Olsen, K., Pitarka, A., Song, S., and Templeton, E.** (2009). The SCEC/USGS Dynamic Earthquake Rupture Code Verification Exercise. *Seismological Research Letters*, **80**(1), 119–126.  
Referenced in: 5.4
- Hauksson, E., Jones, L. M., Hutton, K., and Eberhart-Phillips, D.** (1993). The 1992 Landers Earthquake Sequence: Seismological Observations. *J. Geophys. Res.*, **98**, 19835–19858.  
Referenced in: 5.5

- Hermann, V.** (2010). *ADER-DG - Analysis, further Development and Applications*. Dissertation, Ludwig-Maximilians-Universität München, Department für Geo- und Umweltwissenschaften.  
**Referenced in:** 2
- Hermann, V., Käser, M., and Castro, C. E.** (2011). Non-conforming hybrid meshes for efficient 2D wave propagation using the Discontinuous Galerkin method. *Geophys. J. Int.*, **184**(2), 746–758.  
**Referenced in:** 2.6, 4.3.1, 4.4.1
- Hesthaven, J. and Warburton, T.** (2008). *Nodal Discontinuous Galerkin Methods: Algorithms, Analysis, and Applications*. Springer, New York.  
**Referenced in:** 1, 2.1, 2.3.2, 3.2, 5.4.1, 5.4.2
- Hu, F., Hussaini, M., and Rasetarinera, P.** (1999). An analysis of the discontinuous Galerkin method for wave propagation problems. *jcp*, **151**, 921–946.  
**Referenced in:** 5.1
- Huang, Y. and Ampuero, J.-P.** (2011). Pulse-like ruptures induced by low-velocity fault zones. *J. Geophys. Res.*, **in press**.  
**Referenced in:** 1
- Ichimura, T., Hori, M., and Bielak, J.** (2009). A hybrid multiresolution meshing technique for finite element three-dimensional earthquake ground motion modelling in basins including topography. *Geophys. J. Int.*, **177**, 1221–1232.  
**Referenced in:** 4.1
- Ida, Y.** (1973). The maximum acceleration of seismic ground motion. *Bull. Seism. Soc. Am.*, **63**, 959–968.  
**Referenced in:** 5.4.1, 5.4.2
- Kaneko, Y., Lapusta, N., and Ampuero, J.-P.** (2008). Spectral element modeling of spontaneous earthquake rupture on rate and state faults: Effect of velocity-strengthening friction at shallow depths. *J. Geophys. Res.*, **113**, B09317.  
**Referenced in:** 5.1, 5.4.2
- Karypis, G. and Kumar, V.** (1998). Multilevel k-way partitioning scheme for irregular graphs. *J. Parallel Distrib. Comput.*, **48**, 96–129.  
**Referenced in:** 2.6
- Käser, M. and Dumbser, M.** (2006). An arbitrary high order discontinuous Galerkin method for elastic waves on unstructured meshes I: The two-dimensional isotropic case with external source terms. *Geophys. J. Int.*, **166**(2), 855–877.  
**Referenced in:** 1, 2, 2.3.4, 2.3.4, 2.4, 3.2, 5.3.1
- Käser, M. and Dumbser, M.** (2008). A highly accurate discontinuous galerkin method for complex interfaces between solids and moving fluids. *Geophysics*, **73**(3), T23–T35.  
**Referenced in:** 3.4.1

- Käser, M. and Gallovič, F.** (2008). Effects of complicated 3d rupture geometries on earthquake ground motion and their implications: A numerical study. *Geophys. J. Int.*, **72**(1), 276–292.  
Referenced in: 2
- Käser, M. and Iske, A.** (2005). ADER schemes on adaptive triangular meshes for scalar conservation laws. *J. Comp. Phys.*, **205**, 486–508.  
Referenced in: 5.1
- Käser, M., Mai, P., and Dumbser, M.** (2007). On the accurate treatment of finite source rupture models using ADER-DG on tetrahedral meshes. *Bull. Seism. Soc. Am.*, **97**(5), 1570–1586.  
Referenced in: 2, 2.4
- Käser, M., Hermann, V., and de la Puente, J.** (2008). Quantitative Accuracy Analysis of the Discontinuous Galerkin Method for Seismic Wave Propagation. *Geophys. J. Int.*, **173**(3), 990–999.  
Referenced in: 2, 3.4.2, 4.2.1, 5.1, 5.4.2
- Käser, M., Pelties, C., Castro, C., Djikpessa, H., and Prange, M.** (2010). Wave Field Modeling in Exploration Seismology Using the Discontinuous Galerkin Finite Element Method on HPC-infrastructure. *The Leading Edge*, **29**, 76–85.  
Referenced in: 2
- Kawase, H.** (1988). Time-domain response of a semi-circular canyon for incident SV, P, and Rayleigh waves calculated by the discrete wavenumber boundary element method. *Bull. Seism. Soc. Am.*, **78**(4), 1415–1437.  
Referenced in: 4.2.1
- Komatitsch, D. and Vilotte, J.** (1998). The spectral-element method: an efficient tool to simulate the seismic response of 2D and 3D geological structures. *Bull. Seism. Soc. Am.*, **88**, 368–392.  
Referenced in: 2.1
- Komatitsch, D., Barnes, C., and Tromp, J.** (2002). Spectral-element simulations of global seismic wave propagation - I. validation. *Geophys. J. Int.*, **149**, 390–412.  
Referenced in: 2.1
- Kozdon, J. E., Dunham, E. M., and Nordström, J.** (revised: 05 June 2012). Simulation of dynamic earthquake ruptures in complex geometries using high-order finite difference methods. *J. Sci. Comp.*  
Referenced in: 2.1
- Kristek, J., Moczo, P., and Galis, M.** (2010). Stable discontinuous staggered grid in the finite-difference modeling of seismic motion. *Geophys. J. Int.*, **183**(3), 1401–1407.  
Referenced in: 2.1

- Kristeková, M., Kristek, J., Moczo, P., and Day, S.** (2006). Misfit criteria for quantitative comparison of seismograms. *Bull. Seism. Soc. Am.*, **96**(5), 1836–1850.  
**Referenced in:** 4.2.2, 4.3.2
- Kristeková, M., Kristek, J., and Moczo, P.** (2009). Time-frequency misfit and goodness-of-fit criteria for quantitative comparison of time signals. *Geophys. J. Int.*, **178**, 813–825.  
**Referenced in:** 4.2.2, 4.3.2, 4.4.2
- Krivodonova, L.** (2007). Limiters for high-order discontinuous galerkin methods. *Journal of Computational Physics*, **226**, 879–896.  
**Referenced in:** 5.4.2
- Lachenbruch, A. H.** (1980). Frictional heating, fluid pressure and the resistance to fault motion. *J. Geophys. Res.*, **85**, 6097–6112.  
**Referenced in:** 5.2
- Lapusta, N., Rice, J., Ben-Zion, Y., and Zheng, G.** (2000). Elastodynamic analysis for slow tectonic loading with spontaneous rupture episodes on faults with rate- and state-dependent friction. *J. Geophys. Res.*, **105**, 23765–23789.  
**Referenced in:** 5.1
- Levander, A.** (1988). Fourth-order finite difference P-SV seismograms. *Geophysics*, **53**, 1425–1436.  
**Referenced in:** 2.1
- LeVeque, R.** (2002). *Finite Volume Methods for Hyperbolic Problems*. Cambridge University Press, Cambridge.  
**Referenced in:** 2.2, 5.1, 5.3.2
- Li, Y.-G., Aki, K., Adams, D., Hasemi, A., and Lee, W. H. K.** (1994). Seismic guided waves trapped in the fault zone of the Landers, California, earthquake of 1992. *J. Geophys. Res.*, **99**, 11705–11722.  
**Referenced in:** 5.5
- Lisitsa, V., Reshetova, G., and Tcheverda, V.** (2011). Finite-difference algorithm with local time-space grid refinement for simulation of waves. *Computational Geosciences*.  
**Referenced in:** 2.1
- Madariaga, R.** (1976). Dynamics of an expanding circular fault. *Bull. Seism. Soc. Am.*, **65**, 163–182.  
**Referenced in:** 2.1
- Madariaga, R., Olsen, K., and Archuleta, R.** (1998). Modeling dynamic rupture in a 3D earthquake fault model. *Bull. Seism. Soc. Am.*, **88**, 1182–1197.  
**Referenced in:** 5.1

- Mase, C. and Smith, L.** (1985). Pore-fluid pressures and frictional heating on a fault surface. *Pure and Applied Geophysics*, **122**, 583–607.  
**Referenced in:** 5.2
- Mase, C. and Smith, L.** (1987). Effects of frictional heating on the thermal, hydrologic, and mechanical response of a fault. *J. Geophys. Res.*, **92**, 6249–6272.  
**Referenced in:** 5.2
- Mercerat, E., Vilotte, J.-P., and Sánchez-Sesma, F.** (2006). Triangular spectral element simulation of two-dimensional elastic wave propagation using unstructured triangular grids. *Geophys. J. Int.*, **166**, 679–698.  
**Referenced in:** 4.1
- Moczo, P., Kristek, J., Vavrycuk, V., Archuleta, R., and Halada, L.** (2002). 3D heterogeneous staggered-grid finite-difference modeling of seismic motion with volume harmonic and arithmetic averaging of elastic moduli and densities. *Bull. Seism. Soc. Am.*, **92**(8), 3042–3066.  
**Referenced in:** 2.1, 4.1
- Moczo, P., Kristek, J., Galis, M., Pazak, P., and Balazovjeh, M.** (2007a). The finite-difference and finite-element modeling of seismic wave propagation and earthquake motion. *Acta physica slovacica*, **57**(2), 177–406.  
**Referenced in:** 2.1, 4.1, 5.1
- Moczo, P., Robertsson, J., and Eisner, L.** (2007b). The finite-difference time domain method for modeling of seismic wave propagation. *Advances in Wave Propagation in Heterogeneous Earth*, **48**, 421–516.  
**Referenced in:** 2.1, 4.1
- Moczo, P., Kristek, J., Galis, M., and Pazak, P.** (2010). On accuracy of the finite-difference and finite-element schemes with respect to p-wave to s-wave speed ratio. *Geophys. J. Int.*, **182**, 493–510.  
**Referenced in:** 4.2.3
- Oglesby, D., Archuleta, R., and Nielsen, S.** (1998). The three-dimensional dynamics of dipping faults. *Bull. Seism. Soc. Am.*, **90**, 616–628.  
**Referenced in:** 2.1, 5.1
- Oglesby, D., Archuleta, R., and Nielsen, S.** (2000). Earthquakes on dipping faults: the effects of broken symmetry. *Science*, **280**, 1055–1059.  
**Referenced in:** 5.1
- Ohminato, T. and Chouet, B. A.** (1997). A free-surface boundary condition for including 3D topography in the finite-difference method. *Bull. Seism. Soc. Am.*, **87**(2), 494–515.  
**Referenced in:** 4.2.1

- Olsen, K., Madariaga, R., and Archuleta, R. J.** (1997). Three-dimensional dynamic simulation of the 1992 Landers earthquake. *Science*, **278**(5339), 834–838.  
**Referenced in:** 5.5
- Olsen, K., Day, S., Minster, J., Cui, Y., Chourasia, A., Faerman, M., Moore, R., Maechling, P., and Jordan, T.** (2006). Strong shaking in los angeles expected from southern san andreas earthquake. *Geophys. Res. Lett.*, **33**(7), 575–596.  
**Referenced in:** 4.1
- Pasquetti, R. and Rapetti, F.** (2006). Spectral element methods on unstructured meshes: Comparisons and recent advances. *J. Sci. Comput.*, **27**, 377–387.  
**Referenced in:** 4.1
- Pelties, C., Käser, M., Hermann, V., and Castro, C. E.** (2010). Regular versus irregular meshing for complicated models and their effect on synthetic seismograms. *Geophys. J. Int.*, **183**(2), 1031–1051.  
**Referenced in:** 2, 2.1, 5.1
- Pelties, C., de la Puente, J., Ampuero, J.-P., Brietzke, G. B., and Käser, M.** (2012). Three-Dimensional Dynamic Rupture Simulation with a High-order Discontinuous Galerkin Method on Unstructured Tetrahedral Meshes. *J. Geophys. Res.*, Seite in press.  
**Referenced in:** 1
- Pitarka, A.** (1999). 3D elastic finite-difference modeling of seismic motion using staggered grids with nonuniform spacing. *Bull. Seis. Soc. Am.*, **89**(1), 54–68.  
**Referenced in:** 2.1
- Poliakov, A., Dmowska, R., and Rice, J.** (2002). Dynamic shear rupture interactions with fault bends and off-axis secondary faulting. *J. Geophys. Res.*, **107**(2295), 6–1.  
**Referenced in:** 5.5
- Priolo, E., Carcione, J., and Seriani, G.** (1994). Numerical simulation of interface waves by high-order spectral modeling techniques. *J. Acoust. Soc. Am.*, **95**, 681–693.  
**Referenced in:** 2.1
- Reed, W. and Hill, T.** (1973). Triangular mesh methods for the neutron transport equation. Technical Report LA-UR-73-479, Los Alamos Scientific Laboratory.  
**Referenced in:** 2.1
- Rice, J. R.** (1999). Flash heating at asperity contacts and rate-dependent friction. *Eos Trans. AGU*, **80**(46), Fall Meet. Suppl., F681.  
**Referenced in:** 5.2
- Robertsson, J.** (1996). A numerical free-surface condition for elastic/viscoelastic finite-difference modeling in the presence of topography. *Geophysics*, **96**(4B), S11–S27.  
**Referenced in:** 2.1, 4.1, 4.2.3

- Roden, J. and Gedney, S.** (2000). Convolution PML (CPML): an efficient FDTD implementation of the CFS-PML for arbitrary media. *Microw. Opt. Technol. Lett.*, **27**, 334–339.  
**Referenced in:** 2.5.2
- Rojas, O., Dunham, E. M., Day, S., Dalguer, L., and Castillo, J.** (2009). Finite difference modelling of rupture propagation with strong velocity-weakening friction. *Geophys. J. Int.*, **179**, 1831–1858.  
**Referenced in:** 1, 5.4.2
- Ruina, A. L.** (1983). Slip instability and state variable friction laws. *J. Geophys. Res.*, **88**, 10359–10370.  
**Referenced in:** 5.2
- Schwartzkopff, T., Munz, C., and Toro, E.** (2002). ADER: A high-order approach for linear hyperbolic systems in 2D. *J. Sci. Comput.*, **17**, 231–240.  
**Referenced in:** 2.1, 2.3.4
- Seriani, G.** (1998). 3-D large-scale wave propagation modeling by a spectral-element method on a Cray T3E multiprocessor. *Comput. Methods Appl. Mech. Eng.*, **164**, 235–247.  
**Referenced in:** 2.1
- Seriani, G., Priolo, E., Carcione, J., and Padovani, E.** (1992). High-order spectral element method for elastic wave modeling. *Soc. of Expl. Geophys., 62nd Ann. Internat. Mtg*, 1285–1288.  
**Referenced in:** 2.1
- Sherwin, S.** (2000). Dispersion analysis of the continuous and discontinuous Galerkin formulation. *International Symposium on Discontinuous Galerkin Methods, Newport, RI, USA*, **2**, 425–431.  
**Referenced in:** 5.1
- Smith, T. M., Collis, S. S., Ober, C. C., Overfelt, J. R., and Schwaiger, H. F.** (2010). Elastic Wave Propagation in Variable Media using a Discontinuous Galerkin Method. *SEG Technical Program Expanded Abstracts*, **29**(1), 2982–2987.  
**Referenced in:** 1
- Stein, S. and Wysession, M.** (2003). *An Introduction to Seismology, Earthquakes, and Earth Structure*. Blackwell Publishing, Malden, MA.  
**Referenced in:** 2.2
- Stupazzini, E. C. M., Lee, S. J., Komatitsch, D., Piersanti, A., and Tromp, J.** (2008). *Proceedings of the 16th International Meshing Roundtable*, chapter CUBIT and Seismic Wave Propagation Based Upon the Spectral-Element Method: An Advanced Unstructured Mesher for Complex 3D Geological Media, 579–597. Springer, Berlin.  
**Referenced in:** 4.1

- Symes, W., Terentyev, I., and T.W., V.** (2008). Gridding requirements for accurate finite difference simulation. *SEG Expanded Abstracts*, **27**, 2077–2081.  
**Referenced in:** 2.1, 4.1
- Tada, T. and Madariaga, R.** (2001). Dynamic modelling of the flat 2-D crack by a semi-analytic BIEM scheme. *International Journal for Numerical Methods in Engineering*, **50**(1), 227–251.  
**Referenced in:** 5.1
- Tamura, S. and Ide, S.** (2011). Numerical study of splay faults in subduction zones: The effects of bimaterial interface and free surface. *Journal of Geophysical Research*, **116**(B10), 1–18.  
**Referenced in:** 1
- Titarev, V. and Toro, E.** (2002). ADER: Arbitrary high order Godunov approach. *J. Sci. Comput.*, **17**(1-4), 609–618.  
**Referenced in:** 3.2, 5.1
- Toro, E.** (1999). *Riemann Solvers and Numerical Methods for Fluid Dynamics*. 2nd Edition, Springer, Berlin.  
**Referenced in:** 2.3.2, 3.2, 5.1, 5.3.2
- Toro, E. and Titarev, V.** (2002). Solution of the generalized Riemann problem for advection-reaction equations. *Proc. Roy. Soc. London*, 271–281.  
**Referenced in:** 2.3.4
- Toro, E., Millington, R., and Nejad, L.** (2001). *Towards very high order Godunov schemes*. Kluwer Academic Plenum Publishers, Oxford.  
**Referenced in:** 2.1, 2.3.4
- van Vossen, R., Robertsson, J., and Chapman, C.** (2002). Finite-difference modeling of wave propagation in a fluid-solid configuration. *Geophysics*, **67**(2), 618–624.  
**Referenced in:** 4.1, 4.2.3
- Vilotte, J.-P., Festa, G., and Ampuero, J.-P.** (2006). Dynamic fault rupture propagation using nonsmooth spectral element method. *Eos Trans. AGU*, **87**(52), Fall Meet. Suppl., Abstract S52B–05.  
**Referenced in:** 5.1
- Virieux, J.** (1984). SH-wave propagation in heterogeneous media: Velocity-stress finite-difference method. *Geophysics*, **49**, 1933–1942.  
**Referenced in:** 2.1
- Virieux, J.** (1986). P-SV wave propagation in heterogeneous media: Velocity-stress finite-difference method. *Geophysics*, **51**, 889–901.  
**Referenced in:** 2.1

**Wald, D. and Heaton, T.** (1994). Spatial and temporal distribution of slip for the 1992 Landers, California, earthquake. *Bull. Seis. Soc. Am.*, **84**(3), 668–691.

**Referenced in:** 5.5

**Wilcox, L. C., Stadler, G., Burstedde, C., and Ghattas, O.** (2010). A high-order discontinuous galerkin method for wave propagation through coupled elastic-acoustic media. *J. Comput. Phys.*, **229**, 9373–9396.

**Referenced in:** 1, 4.1

**Zahradnik, J., Moczo, P., and Hron, F.** (1993). Testing four elastic finite-difference schemes for behaviour at discontinuities. *Bull. Seism. Soc. Am.*, **83**, 107–129.

**Referenced in:** 4.1

**Zhang, C. and LeVeque, R.** (1997). The immersed interface method for acoustic wave equations with discontinuous coefficients. *Wave Motion*, **25**, 237–263.

**Referenced in:** 4.1, 4.2.3

**Zhang, C. and Symes, W.** (1998). Fourth order, full-stencil immersed interface method for elastic waves with discontinuous coefficients. *SEG Expanded Abstracts*, **17**, 1929–1932.

**Referenced in:** 4.1, 4.2.3



# Appendix A.

## Orthogonal Basis Functions for Tetrahedral Elements

The presented ADER-DG implementation makes use of the orthogonal hierarchical Dubiner's basis functions (Cockburn *et al.*, 2000). Hierarchical means in this context, that every set of basis functions of degree  $N$  includes all basis functions of all lower degrees as a subset. The basis functions are expressed in terms of the Jacobi polynomials  $P_n^{\alpha,\beta}(x)$ , which are solutions of the Jacobi differential equation

$$(1-x^2)y'' + [\beta - \alpha - (\alpha + \beta + 2)x]y' + n(n + \alpha + \beta + 1)y = 0. \quad (\text{A.1})$$

In the interval  $[-1, 1]$  the polynomials can be written as

$$P_n^{\alpha,\beta}(x) = \frac{(-1)^n}{2^n n!} (1-x)^{-\alpha} (1+x)^{-\beta} \frac{d^n}{dx^n} [(1-x)^{\alpha+n} (1+x)^{\beta+n}]. \quad (\text{A.2})$$

For  $\alpha = \beta = 0$  the Jacobi polynomials  $P_n^{0,0}(x)$  reduce to the Legendre polynomials. We construct the DG basis functions as products of up to the three primal functions

$$\begin{aligned} \Theta_i^a(x) &= P_i^{0,0}(x), \\ \Theta_{ij}^b(x) &= \left(\frac{1-x}{2}\right)^i P_j^{2i+1,0}(x), \\ \Theta_{ijk}^c(x) &= \left(\frac{1-x}{2}\right)^{i+j} P_k^{2i+2j+2,0}(x). \end{aligned} \quad (\text{A.3})$$

For tetrahedrons the reference element  $\mathcal{T}_{ref}$  is defined as

$$\mathcal{T}_{ref} = \{(\xi, \eta, \zeta) \in \mathbb{R}^3 \mid 0 \leq \xi \leq 1 \wedge 0 \leq \eta \leq 1 - \xi \wedge 0 \leq \zeta \leq 1 - \xi - \eta\}. \quad (\text{A.4})$$

The basis functions  $\Phi_k(\xi, \eta, \zeta)$  on this reference element are given by the following product of primal functions:

$$\Phi_{k(p,q,r)}(\xi, \eta, \zeta) = \Theta_p^a(e) \cdot \Theta_{pq}^b(f) \cdot \Theta_{pqr}^c(g), \quad (\text{A.5})$$

with

$$e = \frac{\eta - 1 + \zeta + 2\xi}{1 - \eta - \zeta}, \quad f = \frac{2\eta - 1 + \zeta}{1 - \zeta}, \quad g = 2\zeta - 1. \quad (\text{A.6})$$

The mono-index  $k = k(p, q, r)$  is a function of the index triple  $(p, q, r)$ . For a third order scheme  $\mathcal{O}3$  (polynomial degree  $N = 2$ ) the three-dimensional basis functions are:

$$\begin{aligned}
\Phi_0 &= 1, \\
\Phi_1 &= -1 + 2\xi + \eta + \zeta, \\
\Phi_2 &= -1 + 3\eta + \zeta, \\
\Phi_3 &= -1 + 4\zeta, \\
\Phi_4 &= 1 - 6\xi + 6\xi^2 - 2\eta + 6\xi\eta + \eta^2 - 2\zeta + 6\xi\zeta + 2\eta\zeta + \zeta^2, \\
\Phi_5 &= 1 - 2\xi - 6\eta + 10\xi\eta + 5\eta^2 - 2\zeta + 2\xi\zeta + 6\zeta\eta + \zeta^2, \\
\Phi_6 &= 1 - 8\eta + 10\eta^2 - 2\zeta + 8\eta\zeta + \zeta^2, \\
\Phi_7 &= 1 - 2\xi - \eta - 7\zeta + 12\xi\zeta + 6\eta\zeta + 6\zeta^2, \\
\Phi_8 &= 1 - 3\eta - 7\zeta + 18\eta\zeta + 6\zeta^2, \\
\Phi_9 &= 1 - 10\zeta + 15\zeta^2.
\end{aligned} \tag{A.7}$$

## Appendix B.

# Coordinate Transformation of Tetrahedra

From Dumbser and Käser (2006) we obtain the coordinate transformation of a tetrahedron in the global, Cartesian  $xyz$ -coordinate system into the  $\xi\eta\zeta$ -reference system as shown in Figure 2.1 which is defined by

$$\begin{aligned}
 \xi &= \frac{1}{|\mathbf{J}|} \left[ x_1(y_4z_3 - y_3z_4) + x_3(y_1z_4 - y_4z_1) + x_4(y_3z_1 - y_1z_3) + \right. \\
 &\quad \left. \left( y_1(z_3 - z_4) + y_3(z_4 - z_1) + y_4(z_1 - z_3) \right) x + \right. \\
 &\quad \left. \left( x_1(z_4 - z_3) + x_3(z_1 - z_4) + x_4(z_3 - z_1) \right) y + \right. \\
 &\quad \left. \left( x_1(y_3 - y_4) + x_3(y_4 - y_1) + x_4(y_1 - y_3) \right) z \right] \\
 \eta &= \frac{1}{|\mathbf{J}|} \left[ y_1(x_4z_2 - x_2z_4) + y_2(x_1z_4 - x_4z_1) + y_4(x_2z_1 - x_1z_2) + \right. \\
 &\quad \left. \left( y_1(z_4 - z_2) + y_2(z_1 - z_4) + y_4(z_2 - z_1) \right) x + \right. \\
 &\quad \left. \left( x_1(z_2 - z_4) + x_2(z_4 - z_1) + x_4(z_1 - z_2) \right) y + \right. \\
 &\quad \left. \left( x_1(y_4 - y_2) + x_2(y_1 - y_4) + x_4(y_2 - y_1) \right) z \right] \\
 \zeta &= \frac{1}{|\mathbf{J}|} \left[ z_1(x_3y_2 - x_2y_3) + z_2(x_1y_3 - x_3y_1) + z_3(x_2y_1 - x_1y_2) + \right. \\
 &\quad \left. \left( y_1(z_2 - z_3) + y_2(z_3 - z_1) + y_3(z_1 - z_2) \right) x + \right. \\
 &\quad \left. \left( x_1(z_3 - z_2) + x_2(z_1 - z_3) + x_3(z_2 - z_1) \right) y + \right. \\
 &\quad \left. \left( x_1(y_2 - y_3) + x_2(y_3 - y_1) + x_3(y_1 - y_2) \right) z \right]
 \end{aligned} \tag{B.1}$$

where

$$\begin{aligned}
 |\mathbf{J}| &= x_1 \left( y_2(z_4 - z_3) + y_3(z_2 - z_4) + y_4(z_3 - z_2) \right) + \\
 &\quad x_2 \left( y_1(z_3 - z_4) + y_3(z_4 - z_1) + y_4(z_1 - z_3) \right) + \\
 &\quad x_3 \left( y_1(z_4 - z_2) + y_2(z_1 - z_4) + y_4(z_2 - z_1) \right) + \\
 &\quad x_4 \left( y_1(z_2 - z_3) + y_2(z_3 - z_1) + y_3(z_1 - z_2) \right),
 \end{aligned} \tag{B.2}$$

is the determinant of the Jacobian matrix  $\mathbf{J}$  of the transformation being equal to 6 times the volume of the tetrahedron.

The back-transformation is given through

$$\begin{aligned}x &= x_1 + (x_2 - x_1)\xi + (x_3 - x_1)\eta + (x_4 - x_1)\zeta, \\y &= y_1 + (y_2 - y_1)\xi + (y_3 - y_1)\eta + (y_4 - y_1)\zeta, \\z &= z_1 + (z_2 - z_1)\xi + (z_3 - z_1)\eta + (z_4 - z_1)\zeta.\end{aligned}\tag{B.3}$$

# Acknowledgment

This thesis would not have been possible without the contribution of the following persons I wish to thank:

- Dr. Martin Käser, for offering me this interesting topic, introducing me into numerical seismology and its community, getting me around the world and for meetings on the racing bike. I was always pleased to work in his Emmy-Noether group and to have such an excellent mentor.
- Prof. Dr. Heiner Igel for giving me the opportunity to do a doctor's degree in his seismology group at LMU Munich. His motivating workshops, a combination of science and sport, are unique.
- Prof. Dr. Peter Moczo for his support during my Ph.D. studies and for accepting to evaluate this thesis.
- Prof. Dr. Jean-Paul Ampuero for being a great supporter of my work and having always the proper solution ready. Also for getting me into the SCEC community and enabling a research visit at Caltech.
- Dr. Cristóbal E. Castro, who introduced me into the concept of high-order methods. I never had such a patient mentor and I am glad to have him as a friend.
- Dr. Josep de la Puente for all the fruitful discussions, thorough explanations, motivation and his outstanding seminal work that I was allowed to continue.
- Dr. Luis Angel Dalguer for educating me in dynamic rupture, inviting me to the ETH Zurich and the unforgettable dinner at Prof. Dr. Steven M. Day's place, who I like to thank herewith, too.
- Prof. Dr. Martin Mai for his enthusiasm about my research and his support to access Shaheen.
- Dr. Gilbert Brietzke for his motivation and for always sharing his fair-minded opinion with me.
- My colleagues and room mates for enlightening moments and good collaboration. I am happy to found so many friends within the Geophysics section: Martin van Driel, Dr. Andreas Fichtner, Dr. Celine Hadziioannou, Dr. Verena Hermann, André Horbach, Kasra Hosseini Zad, Simon Kremers, Dr. Dieter Kurrle, Yang Li, Julia Linder, Tobias Megies, Dr. Christoph Moder, Dr. Ilaria Mosca, Maria Fernanda Nader-Nieto, Dr. Nguyen Dinh Pham, Dr. Alan Schiemenz, Dr. Karin Sigloch, Simon Stähler and Stefan Wenk.

- 
- Peter Bergmann, Martin Galis, Frantisek Gallovic, Percey E. Galvez, Yihe Huang, Dr. Irene Molinari and Luca Passone for great collaborations and idea sharing outside the LMU.
  - The administration and IT-service: Marion Bachhäubl, Alex Hornung, Greta Küppers, Dr. Marcus Mohr, Dr. Jens Oeser, Yvonne Schirmer, Gerald Schroll, Ludwig Siebel, Veronika Strachwitz and Veronika Weber.
  - Fabian Schölling and Thomas Stork my friends outside the university who helped me to keep a fair balance and, especially, for always being good and patient listeners for all kind of issues.
  - My family for support and backing me all the way.
  - Cathrin Hesselink, who consults me about all issues about and around my work and for her belief in me.